HIGH-RESOLUTION STUDIES OF INTACT SOLID-LIQUID INTERFACES AND REACTIVE MATERIALS BY CRYOGENIC ELECTRON MICROSCOPY

A Dissertation

Presented to the Faculty of the Graduate School

of Cornell University

In Partial Fulfillment of the Requirements for the Degree of

Doctor of Philosophy

by

Michael Joseph Zachman

August 2018

HIGH-RESOLUTION STUDIES OF INTACT SOLID-LIQUID INTERFACES AND REACTIVE MATERIALS BY CRYOGENIC ELECTRON MICROSCOPY

Michael Joseph Zachman, Ph.D.

Cornell University 2018

Solid-liquid interfaces play a key role in many processes, such as biomineralization, crystal growth, and electrochemical energy generation and storage, but often lack characterization at spatial resolutions relevant to these processes. Additionally, many techniques used currently require the sample to be washed and dried, which can significantly alter the structure and chemistry of the interface. Finally, chemically reactive materials are present at solid-liquid interfaces in many devices, such as batteries, which makes preparation, storage, and characterization of these materials in an unaltered state challenging. In the work presented here, we describe cryogenic electron microscopy techniques that allow us to study the structure and bonding of intact solid-liquid interfaces and reactive materials at high resolution. We introduce a paired cryo-focused ion beam/scanning electron microscopy technique designed to enable the native structure and elemental composition of natural and engineered interfacial layers tens of nanometers thick to be characterized on surfaces in devices. Additionally, we describe a cryo-focused ion beam technique for extracting and preparing solid-liquid interface cross sections for high-resolution scanning transmission electron microscopy with the liquids intact, including a method for precisely localizing features of interest without labels, even those below the sample surface in some cases. Finally, we combine these techniques to study electrode-electrolyte interfaces processes at the nanoscale in lithium metal batteries, which are promising candidates to replace lithium-ion batteries, but which are currently limited by processes that occur at these interfaces. We find that

two types of dendritic lithium structures are present at the lithium anode-electrolyte interface, one which has an extended interphase layer on its surface, and the other which is composed of uniform lithium hydride, which has not been observed before. These lithium hydride dendrites may contribute disproportionately to the significant capacity fade observed in lithium metal batteries, and our findings allowed us to propose potential methods for inhibiting these dendrites, which initial experiments support. The development of the cryogenic techniques described here has thus not only allowed us to reveal never-before-seen features of solid-liquid interfaces at the nanoscale, but has enabled practical pathways toward improving lithium metal battery performance to be proposed.

BIOGRAPHICAL SKETCH

Michael Zachman was born in Kokomo, IN to Joseph and Deborah Zachman, and has two younger siblings, Lindsey and Anthony. He attended public school until fourth grade, after which his mother began home-schooling him. When he was young, Michael had a strong interest in science and engineering, and the ability to emphasize these topics by home-schooling allowed him to retain his curiosity and desire to learn later in life. This, along with constant encouragement from his father to follow his passion, is what he believes led him to a career in science. Michael returned to public school in Altoona, WI for his junior year of high school, and took courses at Ivy Tech Community College and Purdue University for his senior year. In 2006, Michael began at Purdue University, and spent three years in the Management and Building Construction Management programs. During this time, Michael discovered his strong interest in physics while taking a required mechanics course and a subsequent electromagnetism elective. Michael enjoyed these courses immensely, and they completely transformed his view of the world around him. With encouragement from his professor, family, and friends, he switched majors after his Junior year. In 2012, Michael graduated with Highest Distinction from Purdue University with a Bachelor of Science in Physics. During his undergraduate studies he decided he wanted to inspire and educate others with science, as he had been, as well as use physics to research renewable energy. As a result, he chose to pursue a PhD and was admitted to the Applied Physics program at Cornell University in the fall of 2012. During Michael's first year at Cornell he was a teaching assistant for courses on electromagnetism, quantum mechanics, and mathematical physics, and in subsequent years was a member of Lena Kourkoutis' research group, where he developed the cryogenic electron microscopy techniques outlined in this thesis. He anticipates receiving his PhD in August of 2018, and will be transitioning to a postdoctoral position at Oak Ridge National Laboratory.

ACKNOWLEDGEMENTS

First, I would like to thank my advisor Lena for all of her guidance and mentoring. Without much ability to judge the potential of various research projects when I began at Cornell, I put my trust in the impact she anticipated my project would have, and it has paid off. I was very fortunate to be in the right place at the right time. During my time in her group, my skills as a researcher, writer, and presenter have dramatically improved as a direct consequence of her skill in these areas and how closely she works with her students. I would also like to thank Professors Héctor Abruña and Tobias Hanrath for serving on my special committee.

Many thanks also need to go to my collaborators, including Emily Asenath-Smith, Snehashis Choudhury, Barnaby Levin, Seung-Ho Yu, and especially Zhengyuan Tu for our close collaboration over many years and projects, as well as Professors Héctor Abruña, Lynden Archer, Lara Estroff and David Muller.

I also want to thank the labmates that I have interacted with daily for the last few years, including Ismail El Baggari, Berit Goodge, Jade Noble, Ben Savitzky, and Katie Spoth, for making my time here more enjoyable, with an additional thanks to David Baek for our many interesting conversations and collaboration, as well as my more recent labmates Colin Bundschu, Laila Hayani, Taylor Moon, Michelle Smeaton, Duncan Sutherland, and Yue Yu, for bringing new personality and energy to the group.

Finally, I would like to thank my family for their encouragement recently and throughout my life, my wife Christine for being supportive throughout our time here, and my daughter Lyla for being so good and tolerating how busy I often am at home.

TABLE OF CONTENTS

LIST OF FIGURES

LIST OF TABLES

CHAPTER 1

INTRODUCTION

The modern world relies on energy storage to power devices in locations not physically connected to energy sources, or at times after the energy was generated. One form that has become nearly ubiquitous in our society is electrochemical energy storage, in the form of batteries. Today, rechargeable batteries power nearly all portable electronic devices such as cell phones, laptop computers, etc. Additionally, in a little over a decade hybrid electric vehicles (HEVs), plug-in hybrid electric vehicles (PHEVs), and electric vehicles (EVs), all of which use large battery packs to provide some or all of the vehicle's energy, have grown significantly in popularity [1]. With the continued push towards cleaner and more efficient transportation, the proportion of battery-powered vehicles is likely to continue to increase steadily into the future. In parallel with this change of energy storage in transportation is the transition of electricity production from fossil-fuels to renewable energy sources, such as solar energy [2], that is beginning. Many renewable energy sources are inherently intermittent, and therefore require energy storage to match the fluctuating supply to demand, and many types of batteries are being proposed for this purpose as well [3]. Clearly, batteries play an important role in society today and will play an increasingly pivotal role in the future. Many applications, however, require increased energy density compared to current lithium-ion batteries, which have dominated the market since their introduction nearly thirty years ago [4].

The operation and performance of batteries is highly dependent on nanoscale

processes at interfaces between materials within them, commonly solid-liquid interfaces between electrodes and liquid electrolytes [5]. A characterization technique capable of probing the nanoscale structure and chemistry of solid-liquid interfaces is therefore necessary to fully understand and control these processes. Additionally, many of the materials used in batteries are highly chemically reactive and sensitive to air and/or moisture, such as lithium, and techniques to accurately characterize these materials are needed as well. Finally, these processes occur within macroscopic batteries, so techniques that can bridge the size gap between the devices and the nanoscale processes at the interfaces within them are essential.

When paired with focused ion beam (FIB) techniques, electron microscopy allows high-resolution structural, elemental, and bonding information about materials and interfaces within large devices to be obtained. Pairing FIB with scanning electron microscopy (SEM), for example, allows surface and cross-sectional structures and elemental compositions to be imaged and mapped by energy dispersive X-ray (EDX) spectroscopy down to the nanoscale [6]. To obtain atomic-resolution structural and bonding information about the sample, the FIB can be used as a sample preparation tool for extracting electron-transparent cross-sectional lamellas from devices for subsequent transmission electron microscopy (TEM) and aberration-corrected scanning transmission electron microscopy (STEM) paired with electron energy-loss spectroscopy (EELS) [7,8].

All of these techniques are routinely used to study solid materials, but to enable characterization of solid-liquid interfaces by traditional methods, samples must be washed and dried to remove the liquids. While this does provide some information about

the interface, the harsh sample preparation necessary for these traditional electron microscopy techniques can significantly alter the structure and chemistry of the interface by removing liquids and soft or brittle materials, as well as potentially allowing reactive materials to interact with a foreign environment [9].

To address these issues and enable high-resolution characterization of fully intact solid-liquid interfaces and unaltered reactive materials, in the work described here we adapt standard room-temperature microscopy techniques for use with samples at cryogenic temperatures, a principle similarly implemented in biology for studying frozen-hydrated specimens by cryogenic electron microscopy (cryo-EM) [10]. By rapidly cooling the sample to liquid nitrogen temperature, liquids and structures present at solid-liquid interfaces are preserved in a near-native state. In addition to this preservation, the cryogenic sample temperatures also dramatically reduce the rate of chemical reactions that occur, allowing reactive materials to be characterized in an unaltered state.

Before presenting the details of these techniques and the results they have produced thus far, I will first provide a general background on the basic physics behind battery operation, a history of batteries leading up to the lithium batteries studied in this work, a brief discussion of common materials used in lithium batteries, and details on the potential and remaining challenges for the lithium metal batteries that I have focused on in much of my work. After this, I will discuss the theoretical and practical details of EELS relevant to this work, since this is the technique that allows us to obtain the highest resolution elemental and bonding information. A discussion of the challenges associated with performing EELS on typically beam-sensitive battery materials is also included.

1.1 Electrochemical Energy Storage by Batteries

1.1.1 Basic Physics of Battery Operation

A battery consists of two electrode materials with different electrochemical potentials separated by an ionically conducting and electronically insulating electrolyte material. The electrochemical potential of a species *i* with charge z_i in a phase α is [11]:

$$\boldsymbol{\mu_i^\alpha} = \mu_i^\alpha + z_i e \boldsymbol{\phi}^\alpha \tag{1.1}$$

where μ_i^α is the chemical potential of the species (defined as the change in Gibbs free energy of the system with addition of a single particle of species *i*), *e* is the fundamental unit of charge, and $\boldsymbol{\phi}^\alpha$ is the inner potential of phase α. A difference in electrochemical potential between two materials establishes a driving force for movement of particles from the phase with higher electrochemical potential to the phase with lower electrochemical potential. In a battery, the electrode materials with higher and lower electrochemical potential are termed the "anode" and "cathode," respectively. The electrical driving force between the electrodes can be measured as the open-circuit potential of the cell, given by $V_{OC} = (\boldsymbol{\mu}_A - \boldsymbol{\mu}_C)/e$, where $\boldsymbol{\mu}_A$ and $\boldsymbol{\mu}_C$ are the anode and cathode electrochemical potentials, respectively [12], as shown in Figure 1.1.

To maintain charge neutrality while current is flowing through a battery, ions must be exchanged between the electrodes to compensate for the electronic charge movement. Electrochemical reactions therefore occur in the electrodes during charge/discharge. For the battery to produce useful work, however, the ionic and electronic flows must be separated, and the electronic flow channeled through an external circuit. Electrolyte materials are ionically conducting but electronically

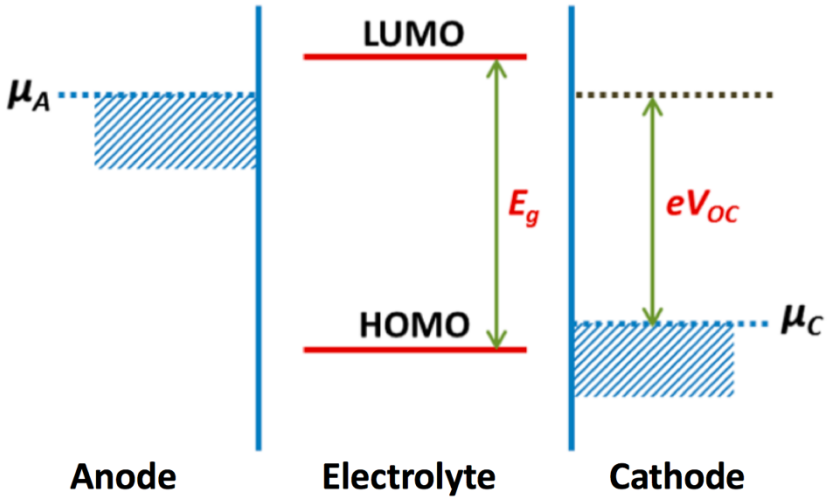

Figure 1.1 Schematic displaying the electrode electrochemical potentials and the cell open circuit potential, as well as the electrolyte highest occupied and lowest unoccupied molecular orbital energies. Reproduced from [12].

insulating, which allows this separation to be established. Electrolytes are therefore placed between the electrodes to form a functional battery. Since the electrolyte is electronically insulating, this also allows energy to be stored long-term, since in principle no current should flow between the electrodes when not connected to an external circuit. If the electrode reactions are reversible, this spontaneous flow of particles can be reversed by application of a sufficiently large voltage that opposes the natural flow, which "recharges" the battery and enables it to be used multiple times.

1.1.2 A Brief History of Rechargeable Lithium Batteries

Though there is some discussion of whether an electrochemical device may have existed around two-thousand years ago, called the "Baghdad Battery" [4], the first undisputed design for an electrochemical device that generated electricity was published by Alessandro Volta in 1800 [13]. An original schematic and an example of one of these

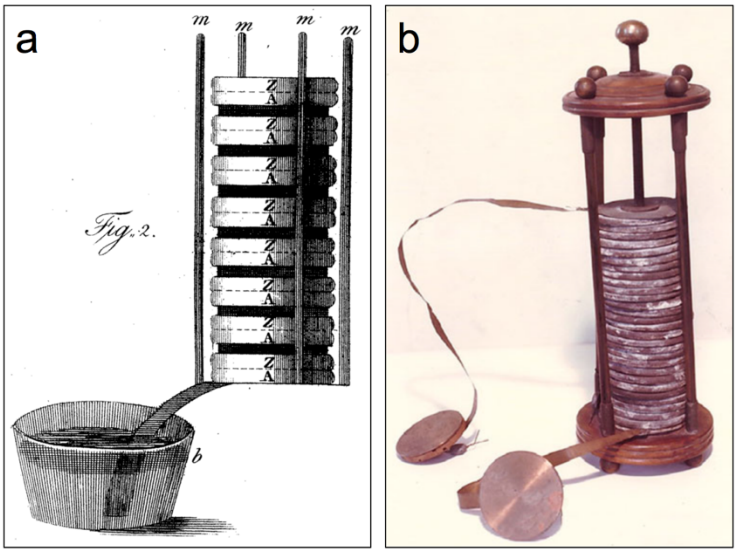

Figure 1.2 The voltaic pile, designed by Alessandro Volta, was the first device for producing electricity electrochemically, and consisted of alternating stacked zinc and silver plates separated by a cloth soaked in a salt solution to enable ionic conductivity. (a) shows a schematic of one type of pile displayed in Volta's original publication, and (b) shows an example of an actual pile. Reproduced from (a) [13], and (b) from [4].

devices, known as a voltaic pile, are shown in Figure 1.2. These original voltaic piles utilized alternating zinc and silver plates to generate a potential difference, and were separated by a cloth soaked in a salt solution to allow ions to flow between the plates. It took nearly sixty years after Volta's original design for the first rechargeable battery to be invented. In 1859, Gaston Planté developed the lead-acid battery, and despite the basic chemistry of this type of cell being known for over 150 years, these batteries are still very common today. For example, lead-acid batteries are still being used to start internal combustion engines (ICEs) in the vast majority of personal vehicles. The next major step forward for rechargeable batteries was the discovery of the Ni-Cd battery chemistry in 1901, which allowed significantly higher energy densities to be achieved, with up to 50 Wh kg^{-1} or more and 200 Wh l^{-1} (compared to 10s of Wh kg^{-1} and up to 100 Wh l^{-1} for lead-acid batteries), as displayed in Figure 1.3 [5]. Since the market for

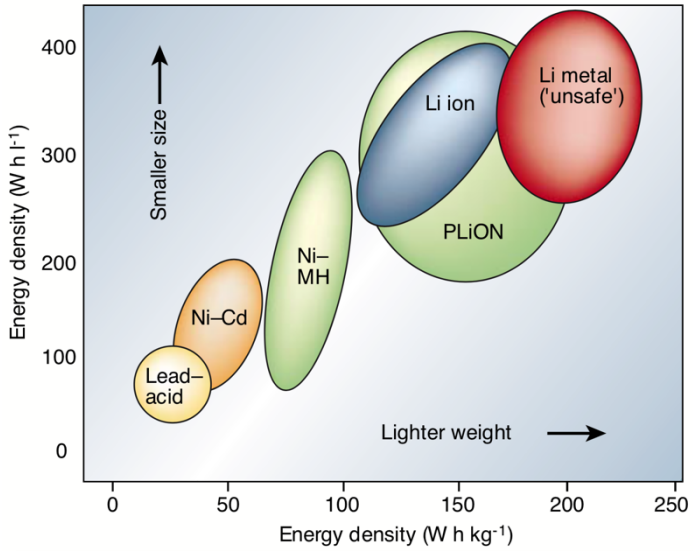

Figure 1.3 Approximate volumetric and specific energy densities of various battery chemistries. Reproduced from [5].

portable electronic devices did not exist at this time, these batteries were sufficient for the applications of the time, and no major advances occurred during many subsequent decades.

As the need for portable power increased, however, researchers sought new battery chemistries that allowed even higher energy densities. One material that began to attract attention was lithium, since it is the lightest metal and has the lowest potential, in theory making a highly energy-dense anode [5]. Though the initial lithium batteries were non-rechargeable, Stan Whittingham demonstrated a rechargeable lithium metal battery (LMB) in 1976 that utilized a reversible TiS_2 cathode material [14]. Unfortunately, the "simple" metal electrodeposition process that occurs during charging of a LMB resulted in issues that limited these batteries, such as formation of lithium growths that protrude from the anode surface, called "dendrites" [5]. These dendrites can grow across the electrolyte and contact the cathode, short-circuiting the battery and resulting in safety

hazards. In addition to the safety concerns, early electrolyte materials continuously broke down on the anode surface, and combined with the fact that dendrites can become disconnected from the anode during cycling, this resulted in a battery capacity that faded rapidly from its initial value. As a result, efforts were focused on finding solutions to these problems through modifications to the anode and electrolyte materials [4].

While many approaches were attempted, the problems with a lithium metal anode were never completely overcome. In 1989, an alternative anode material was demonstrated that still utilized lithium ions shuttled between the electrodes, but which nearly completely eliminated the risk of dendrite formation. These anode materials were composed of carbon and enabled insertion of lithium ions between layers of the material, as opposed to metal deposition on the surface [15]. The addition of non-active mass to the anode did significantly reduce the energy density of this material compared to lithium metal, but the reversibility of the battery was greatly improved, the safety risks were minimized, and the energy density was still a large improvement over Ni-Cd batteries. Consequently, both the research community and commercial interests shifted away from lithium metal to these materials in subsequent years.

While these carbon materials brought lithium ion batteries much closer to commercialization, the anode potential was still sufficient to cause continuous breakdown of the organic electrolytes in use at the time. In 1990, however, Jeff Dahn's group discovered that use of ethylene carbonate (EC) in the electrolyte resulted in the self-limiting formation of a passivation layer on the graphite anode surface, rather than

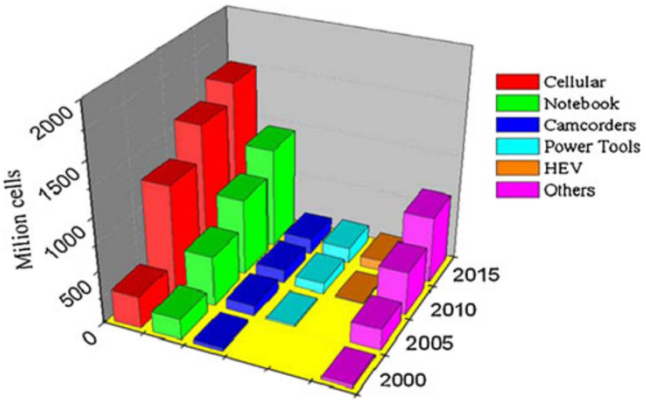

Figure 1.4 Number of Li-ion cells manufactured for different applications in five year intervals from 2000 to 2015. Reproduced from [4].

generation of soluble or gaseous products as with other organic liquids [16]. Reduction of EC on the anode therefore produced a conformal surface layer that blocked further flow of electrons to the electrolyte and limited further decomposition. This enabled reversible cycling of the battery after initial formation of the passivation layer.

Finally, while this work on the anode and electrolyte materials was being performed, progress was also made on improving the energy density of cathode materials. In 1980, John Goodenough's group produced a lithium cobalt oxide ($LiCoO_2$) cathode material [17] that alongside a graphite anode became the basis of the first commercial Li-ion battery, released by Sony in 1991 [18]. These batteries had significantly improved energy densities compared to lead-acid and Ni-Cd batteries, and rapidly became commercially successful, allowing smaller and more powerful portable electronic devices with longer battery lives to be developed. Today, the lithium ion battery dominates the battery market, with billions of cells produced annually, as displayed in Figure 1.4 [4].

While Li-ion technology provided a great improvement in energy density over

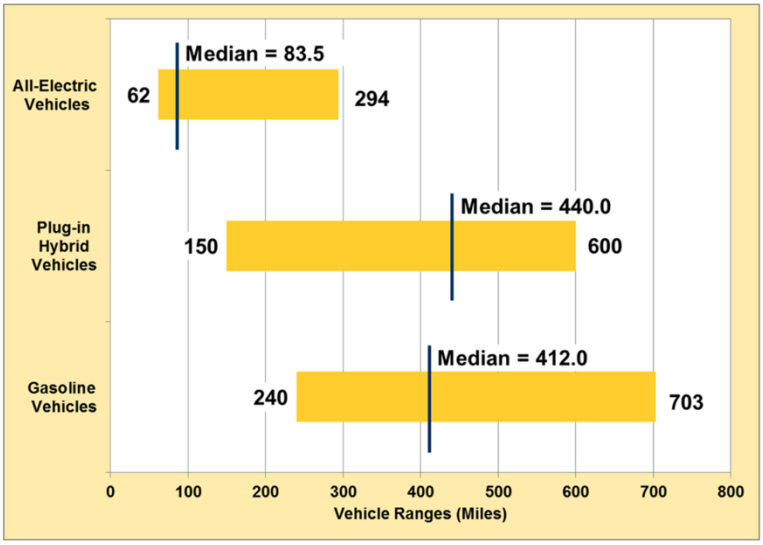

Figure 1.5 EV, PHEV, and gasoline-powered vehicle ranges for model year 2016 vehicles. Reproduced from [19].

previous batteries and essentially enabled the modern portable electronics market, the emerging EV market is putting a strain on their capabilities. In order for the average range of EVs to match that of vehicles powered by ICEs, an energy density increase of around five times is needed while keeping the battery pack size constant, as shown in Figure 1.5 [19]. Li-ion batteries have an inherent limit to their energy density due to the mechanism of lithium storage, and even pushing them to their theoretical limit cannot give the range required to make EVs competitive with ICE powered vehicles while using reasonably sized batteries [20]. An additional challenge is reducing the price of the batteries used in EVs so the total vehicle price becomes comparable to that of an ICE powered vehicle. As a result, new battery materials and chemistries are needed to simultaneously enhance the energy density beyond what can be achieved with Li-ion batteries and reduce the overall cost. In the following section, I will briefly discuss various types of materials currently used in lithium batteries, and those being sought in

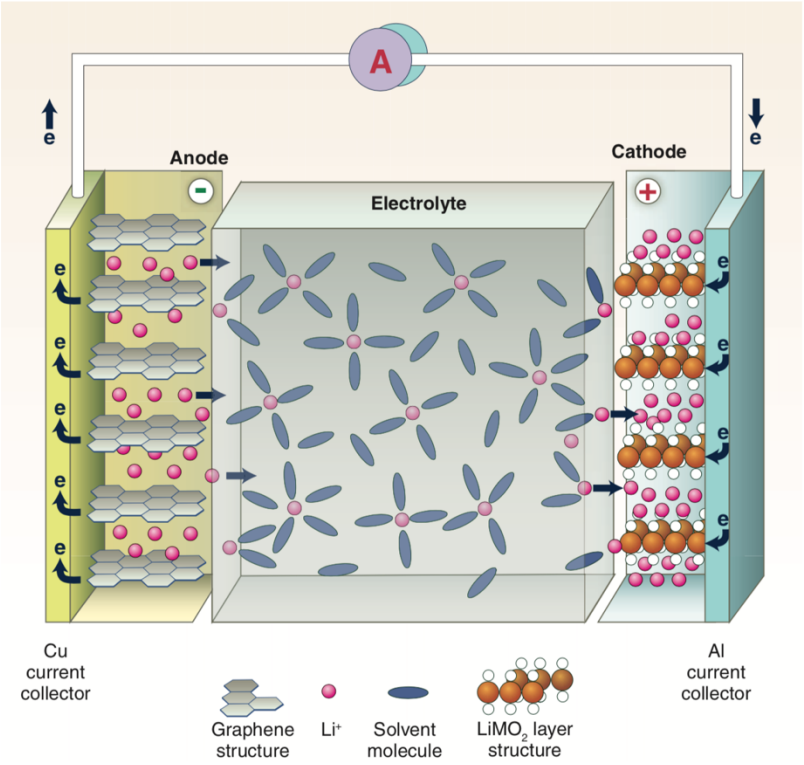

Figure 1.6 Schematic of a typical Li-ion battery with carbon anode and lithium metal oxide intercalation cathode. Reproduced from [3].

order to increase the energy density beyond Li-ion. Subsequently, I will describe in more detail the particular promising system that I primarily studied, including the challenges involved and the approach used here to address these.

1.1.3 Overview of Common Lithium Battery Materials

The chemical reactions that occur in the electrodes of lithium batteries can typically be divided into three categories: intercalation, alloying, and conversion reactions [5,20,21]. Intercalation compounds are the most mature and commonly used, and are the basis of the wide-spread Li-ion battery, shown in Figure 1.6. Intercalation involves ions entering and diffusing through the electrode to come to rest at specific sites within the lattice. In

these electrodes, the ions do not form strong bonds with the surrounding material, and typically exhibit very little volume change during charge/discharge, resulting in a high reversibility. Intercalation compounds typically contain many atoms in the supporting lattice for every ion that can be intercalated, however, which limits the storage capacity of these materials compared to alloying and conversion reaction materials.

Alloying compounds are typically used as anode materials, and often exhibit significantly higher capacities than graphite [5,21]. For example, silicon and tin can react with up to approximately four lithium ions per silicon or tin atom. While this allows high capacity, the high uptake of ions leads to massive volume expansion, up to hundreds of percent. As a result, these materials tend to disintegrate upon cycling, leading to significant capacity fade. To address this, nanostructured electrode materials are being designed that allow the material to accommodate the dramatic expansion and contraction without permanently altering the structure [22].

Materials that react chemically with the mobile ions to form different compounds in the charged/discharged states are referred to as conversion reaction materials, and are generally used for cathodes. For example, one of the most promising conversion cathode materials is sulfur. These cathodes convert sulfur S_8 rings to Li_2S through a multi-step process, and provide the potential to significantly increase energy density compared to current cathode materials [20]. Conversion materials are similar to alloying materials in that they experience significant expansion and contraction during cycling, and have additional challenges to overcome as well, such as dissolution of intermediate polysulfides into the electrolyte in the case of sulfur. Many solutions are being sought to address these issues, such as yolk-shell structures that encapsulate the sulfur and

provide room for expansion, for example [23,24]. Conversion-type cathode materials are often paired with a metal anode since they do not contain the energy storage ions before construction of the battery, as intercalation compounds do. Metal anodes can also offer an order of magnitude larger energy density than graphite anodes, but have a host of challenges associated with them, as mentioned previously and discussed further in the following section.

Several types of electrolyte materials are also used in batteries, and these generally fall into the categories of liquid or solid electrolytes [25]. Some of the most important electrolyte properties are ionic conductivity and chemical/electrochemical stability against the electrode materials. The stability window of the electrolyte is represented by E_g in Figure 1.1, and is defined by the energies between the highest occupied and lowest unoccupied molecular orbitals (HOMO/LUMO) of the electrolyte molecules. If the electrochemical potential of the anode lies above the LUMO or the cathode electrochemical potential lies below the HOMO of the electrolyte, it can react with these materials. As mentioned previously, some materials break down to form a new self-limiting passivation layer on the electrode surface that protects from further breakdown, known as a "solid-electrolyte interphase" (SEI) layer. While liquid electrolytes typically have good ionic conductivity, the stability windows of the most commonly used solvents in lithium batteries, organic liquids, are usually not large enough to prevent reaction. Certain organic solvents, such as EC, form a stable SEI layer in Li-ion batteries though, permitting their use. These materials are still not ideal, however, since they are flammable, among other drawbacks. Additional problems arise when these materials are

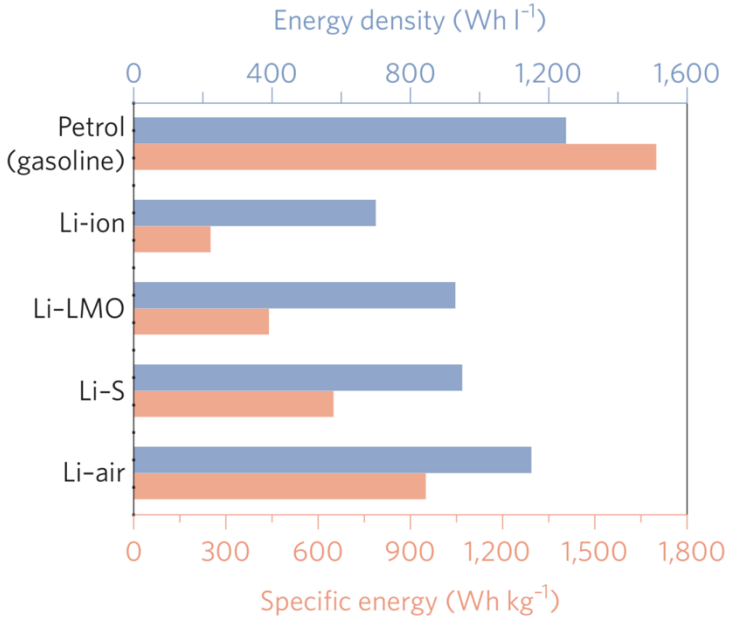

Figure 1.7 Practical energy densities of Li-ion and LMB cells compared to gasoline. Reproduced from [29].

used with metal-anode batteries, which will be discussed further below. Many solid electrolytes, on the other hand, have large stability windows and are not flammable like organic liquids. While ionic conductivities of solid electrolytes are generally lower than liquids, some materials have been identified that have ionic conductivities similar to organic liquids. Major challenges remain for batteries utilizing solid electrolytes though, including loss of electrode-electrolyte contact during cycling and high interfacial resistance. These issues, among others, have limited the performance of ambient-temperature solid-state lithium batteries thus far [26].

1.1.4 Lithium Metal Batteries

One of the anode materials considered most promising for next-generation batteries is lithium metal, the same material used in early LMBs, before focus shifted towards the

graphite for Li-ion batteries. While the challenges associated with these anodes were not overcome in the past, the search for materials with significantly higher energy densities has caused a resurgence of interest in lithium metal, since its theoretical capacity is an order of magnitude larger than graphite (3860 mAh g^{-1} vs. 372 mAh g^{-1} for graphite) [5,27,28]. As mentioned previously, lithium metal anodes also open up the possibility of using cathodes that are not compatible with graphite anodes, which initially contain no lithium. These anodes are thus frequently paired with conversion-type cathode materials, such as sulfur, to form batteries with practical cell energy densities beginning to approach gasoline, as shown in Figure 1.7 [29]. Many of the cathode materials these anodes are paired with are composed of abundant and cheap materials as well, such as sulfur again, which results in lower battery costs [20].

While these anodes have the potential to enable cheaper EVs with ranges competitive with ICE powered vehicles, the same issues that limited LMBs in the 1970's are still present and need to be resolved before these batteries can be commercialized. First, an SEI layer is formed on the surface of the lithium metal, like its counterpart on the graphite anode in a Li-ion battery [30], but the formation mechanisms are not as well understood, and it plays a more important role in the LMB. Rather than forming during the initial cycle like on a graphite anode, the electrochemical potential of lithium metal sits outside the stability window of commonly used organic electrolytes (refer to Figure 1.1) and therefore reduces the electrolyte at any state of charge. Consequently, the electrolyte reacts spontaneously upon contact with the anode surface. The formation of this layer is not homogeneous, and preferential deposition of lithium occurs in regions with increased ionic conductivity [31]. The expansion caused by this localized

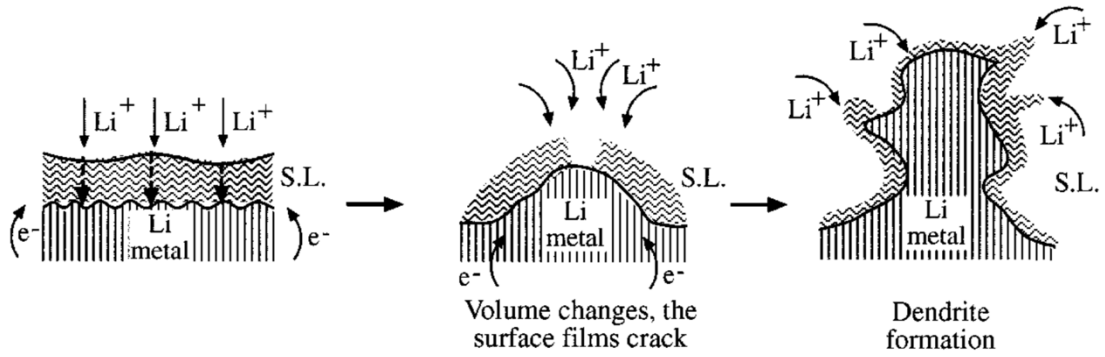

Figure 1.8 Schematic of lithium deposition, SEI layer breaking, and the related nucleation of a dendrite. Reproduced from [32].

deposition can break the SEI layer, exposing the underlying anode surface to the electrolyte and initiating a fresh set of reactions. Reduction of the electrolyte material also consumes lithium, and this repeated breaking and reforming of the SEI contributes to the capacity fade observed in LMBs [27].

In addition to this continuous breaking and reforming of the SEI, the inhomogeneity of the related lithium deposition contributes to another process behind the safety concerns associated with LMBs [32]. Due to a variety of processes, deposition of lithium is not stable, and protrusions from the surface tend to grow, rather than be suppressed [27,33]. This results in uncontrolled localized deposition that forms extended structures. Various types of structures can form and there is some inconsistency in the naming convention, but we will refer to them collectively as "dendrites." The previously discussed SEI processes and the related nucleation of these types of dendrites are represented in Figure 1.8.

Dendrites have two major detrimental effects on LMBs. First, during cycling these structures can become isolated or disconnected from the anode. This results in lost active material, and contributes to the capacity fade of LMBs. Additionally, dendrites can

penetrate the separator between electrodes and cross over to the anode. Upon contact, a short-circuit is produced and the resulting high current locally heats the lithium to very high temperatures. The organic liquids commonly used as electrolyte solvents are flammable, and therefore these dendrite-induced short-circuits can result in fires or explosions. These safety concerns, as well as the rapid capacity fade, are the remaining major barriers to commercialization of LMBs, and therefore must be overcome to provide significantly improved battery energy densities.

Despite the interest these anodes have attracted both in the 1970's and recently, the processes that occur at the electrode-electrolyte interface are not fully understood, due in large part to the difficulty of accurately characterizing solid-liquid interfaces in devices. The two biggest obstacles are the scale of the SEI layer, and the fact that the interface of interest falls between two condensed phases of matter. First, the SEI is generally regarded as on the order of tens of nanometers thick, with spatial variations in materials within the layer on an even smaller scale [34]. As a result, gaining a full understanding of SEI layers requires characterization techniques with at least nanoscale resolution. Additionally, the position of the interfaces between a solid and liquid complicates characterization of the interface, since many probes cannot penetrate these materials [35]. Sample preparation methods typically used to expose the interface can significantly alter its structural and chemical properties [9]. Therefore, in order to accurately characterize the interface, techniques are needed that provide high resolution and access to the interface, as well as circumvent alteration during preparation.

Most techniques used to characterize the SEI thus far have lacked the spatial resolution necessary to reveal its finest features. In fact, many techniques used lack

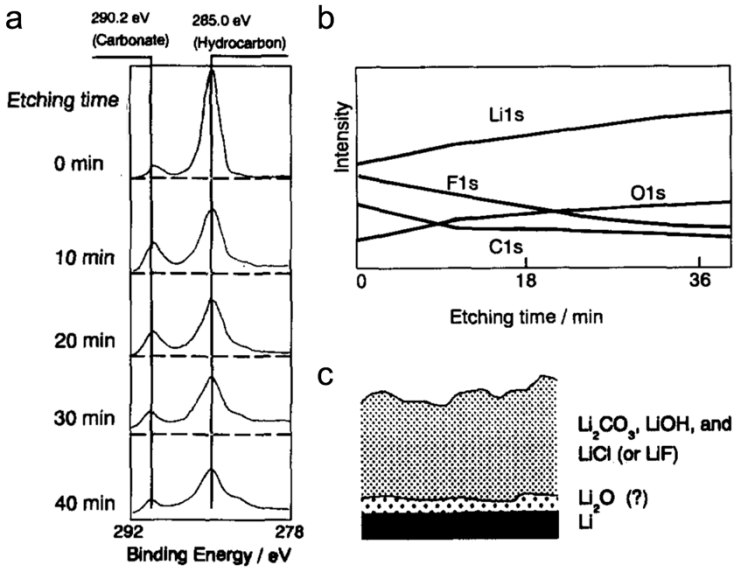

Figure 1.9 Representative data from characterization of an SEI layer by XPS paired with Ar-ion sputtering. (a) C 1*s* spectra of the surface of lithium metal soaked in $LiAsF_6$ + propylene carbonate electrolyte, as a function of sputtering time. (b) The evolution of the spectra from different elements can then be plotted together, and (c) a depth profile of materials can be proposed. Reproduced from [36].

spatial resolution altogether. For example, X-ray photoelectron spectroscopy (XPS) has been commonly used to characterize the chemistry of solid-liquid interfaces for decades [36]. While XPS enables elemental and bonding analysis of samples, it provides no spatial resolution and is surface-sensitive. As such, it is commonly paired with argon-ion sputtering to provide a pseudo depth-profile of the materials present at an interface. This results in data such as that shown in Figure 1.9. The results provided by XPS about SEI layers and reactive battery materials may be questionable though. In addition to the fact that materials sputter at different rates, Ar-ion sputtering has been shown to be capable of altering the chemical composition of materials at the interface [37]. Other techniques have been used over the years to characterize SEI layers with increased spatial resolution, such as time-of-flight secondary ion mass spectrometry (TOF-SIMS) [38], but the majority have not been able to provide spectroscopic data with the spatial

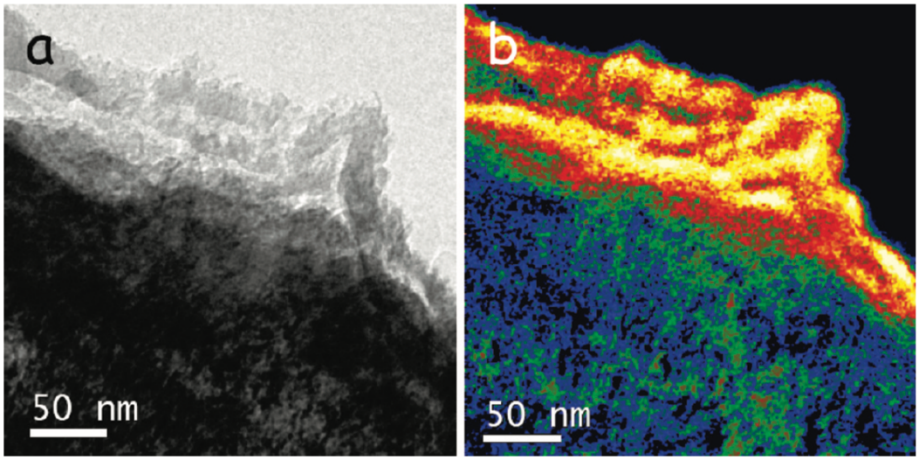

Figure 1.10 (a) Bright-field TEM image and (b) corresponding EELS Li-concentration map demonstrating nanometer-scale resolution of an SEI on a lithiated graphite anode. Reproduced from [39].

resolution needed to gain a full understanding of SEI layers.

One technique that does allow resolution down to the atomic scale and has been applied to battery materials is STEM. When paired with EELS, this technique can provide nanometer scale or better compositional information about battery materials, such as SEI layers, as shown in Figure 1.10 [39]. Unfortunately, although TEM techniques can provide very high resolution, they are limited by the presence of liquids in samples, like many other techniques. Standard sample preparation techniques for TEM and other high-vacuum techniques often involves washing and drying the sample surface to remove the liquid electrolyte. This can alter the structures and chemistry at the surface [9,39], leading to inaccurate results. In fact, it has been shown that simply displacing the liquid from the electrode surface collapses the SEI layer and causes lithium deposits to agglomerate [40], suggesting that alterations due to washing and drying are likely severe.

These washing and drying steps could potentially be circumvented by either

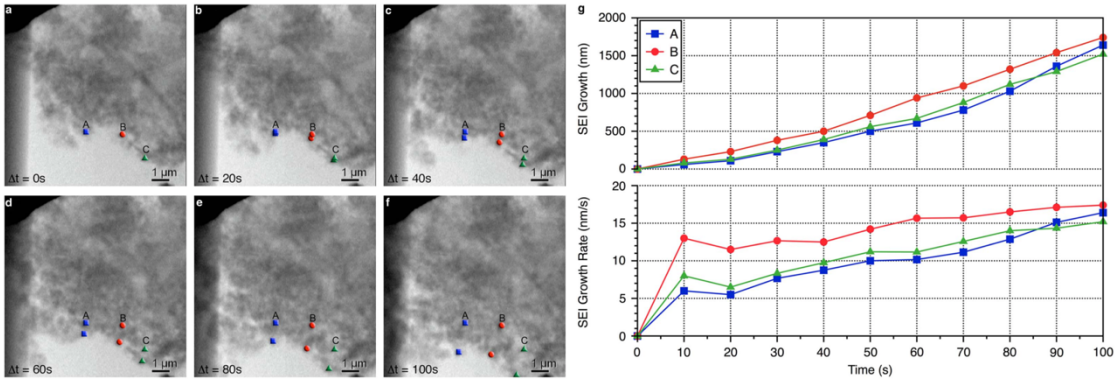

Figure 1.11 Tracking of SEI layer thickness on a graphite electrode by *in situ* TEM. Reproduced from [44].

isolating or immobilizing the liquids while in the instrument. The former is known as *in situ* TEM, and allows liquids to remain present by encapsulating them between two thin silicon nitride windows, preventing contact with the vacuum [40–45]. Using *in situ* techniques, it is possible to study dynamic processes as well, for example growth of the SEI layer on an electrode immersed in electrolyte, such as shown in Figure 1.11 [44]. Despite the ability for *in situ* TEM to examine solid-liquid interfaces with the liquids present, the technique is limited by the small sample size and large cell thickness. Since the sample must fit between the silicon nitride windows, this limits the technique to small samples such as nanoparticles or microelectrodes. Additionally, the cell is more than an order of magnitude thicker than, for example, solid samples prepared for atomic-resolution characterization. This limits both the resolution and spectroscopic capabilities of *in situ* techniques [41,45]. A complementary technique is therefore needed to enable high-resolution characterization of thin intact-solid liquid interface samples taken from large devices.

In this work, I will describe how cryogenic electron microscopy and focused ion beam techniques can be utilized for this purpose, detail the steps necessary to achieve

this, and report initial findings from applying these techniques to LMB systems. I will first describe the physics of inelastic interactions between fast electrons and matter and how it relates to EELS, however, and discuss radiation damage mechanisms that occur in beam-sensitive battery materials. Additionally, I will briefly outline the basic principles of sample freezing, and what cryogenic electron microscopy techniques have been used for previously. Finally, I will conclude by outlining the content of the chapters in this thesis.

1.2 Transmission Electron Microscopy

In a transmission electron microscope, electrons are extracted from a source and accelerated down the instrument column by tens or hundreds of kilovolts. Magnetic lenses manipulate the electron beam to arrive at the sample in a range of different orientations, from a broad and parallel beam in a TEM, to a convergent beam focused to a sub-Ångström spot in a STEM. As the beam electrons pass through the sample, they interact with the nuclei and electrons inside through various physical mechanisms, and these interactions can be measured using appropriate detector configurations. This allows atomic resolution structural, elemental, and bonding information to be obtained from favorable samples.

The first transmission electron microscope was built by Ernst Ruska and Max Knoll in 1931, for which Ruska was awarded the Nobel Prize in Physics in 1986 [46]. Electron microscopes rapidly achieved spatial resolutions far better than optical microscopes, as shown in Figure 1.12 [47]. In 1936, however, Otto Scherzer showed that a fundamental resolution limit exists for rotationally symmetric magnetic lenses such as those used in

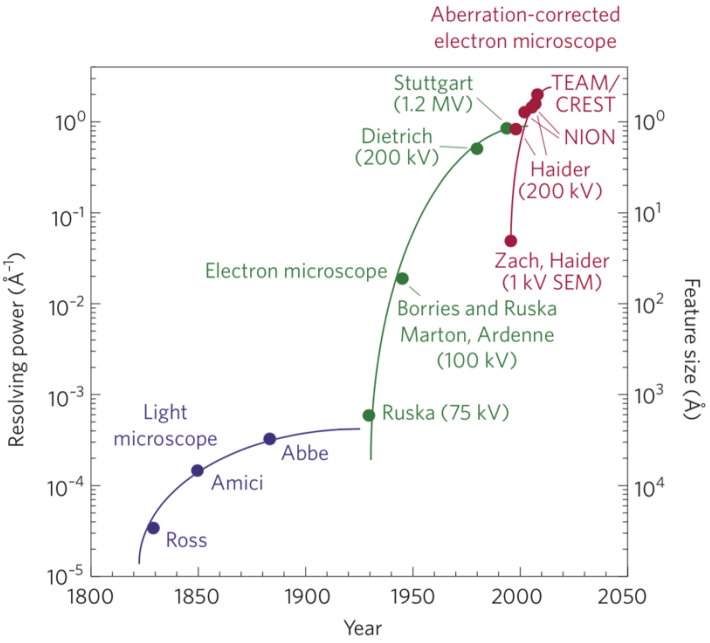

Figure 1.12 Maximum microscope resolution achieved over the past two centuries. Reproduced from [47].

electron microscopes, due to the unavoidable spherical aberration that they generate [48]. In 1947, however, he outlined methods for circumventing this limit by violating various assumptions used for his previous work, including the use of non-rotationally symmetric lenses [49]. As a result, aberration correction using various combinations of non-rotationally symmetric lenses has been sought over the years [50,51]. The addition of extra lenses with multiple poles significantly increases the number of variables involved in properly aligning the instrument, however, and manual alignment proved infeasible. As a result, aberration correction was not successfully implemented until the 1990's, when computing power had advanced enough to assist the alignment procedure [51–55]. The achievable resolution using aberration-corrected instruments has continued to improve, and today commercial aberration-corrected STEMs are capable of routinely achieving sub-Å resolution, as shown in Figure 1.13. In addition to allowing

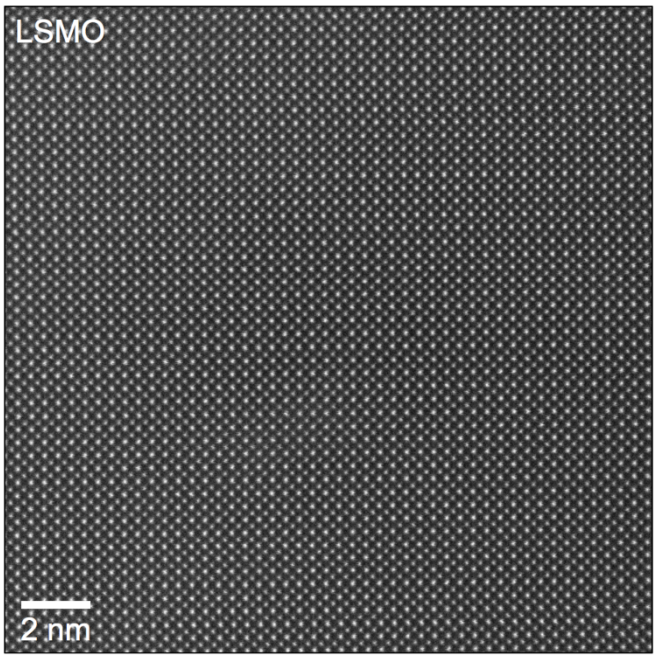

Figure 1.13 An annular dark-field STEM image of the perovskite oxide LSMO taken on Cornell's FEI Titan Themis at 300 kV with a resolution of 0.67 Å.

sub-Å resolution, aberration correction permits the use of larger objective apertures which block less of the beam and provide higher beam currents. This increased beam current allows EELS mapping to be achieved [8], which was pivotal for obtaining full two-dimensional maps of elemental concentrations and bonding environments at intact solid-liquid interfaces in this work.

In the following sections we will discuss the physical mechanisms that give rise to energy losses in two different regions of the electron energy-loss spectrum, and how we can most effectively use these regions to characterize battery materials.

1.2.1 Electron Energy-Loss Spectroscopy

Fast electrons that pass through a material can undergo a variety of inelastic processes that result in a change of the electron's kinetic energy. Electron energy-loss

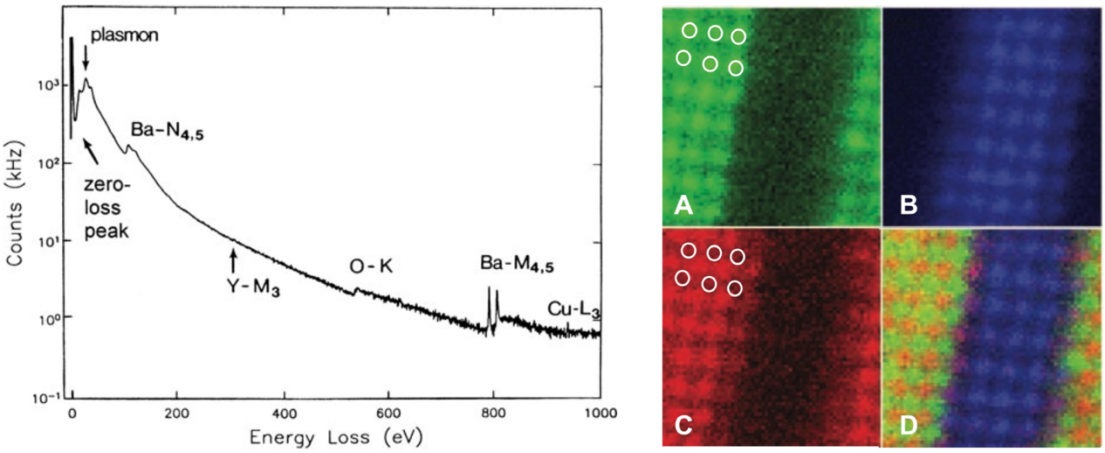

Figure 1.14 Examples of an EELS spectrum and elemental mapping. Left, an EELS spectrum produced from YBCO (log scale). Right, atomic resolution EELS maps of an LSMO/STO multilayer, showing the (a) La M-edge, (b) Ti L-edge, (c) Mn L-edge, and (d) a composite map of the three. Left, reproduced from [56] and right, from [8].

spectroscopy allows these energy losses to be directly measured, revealing many properties about the sample, some of which will be discussed below. To accomplish this, electrons that pass through the sample are deflected by a magnetic prism, dispersing them onto a detector as a function of kinetic energy. The result is a spectrum of counts detected over a range of energy losses, as shown in Figure 1.14 (left). Combined with a focused and scanned STEM probe, EELS can provide maps of composition and bonding with up to atomic-resolution by integrating over a particular energy-loss range in each spatial pixel acquired, as shown in Figure 1.14 (right). Here, we will discuss two regions of the energy-loss spectrum where different types of interactions take place and how the information these regions provide can be utilized to characterize battery materials.

1.2.1.1 Low-Loss EELS

The "low-loss" region of an EELS spectrum extends up to an energy loss of approximately 50 eV, and contains information about a wide variety of sample properties from outer-shell excitations. At the very lowest energies, generally less than

a tenth of an eV [56], collective excitations of the lattice occur in the form of phonons. The typical spread in energies of electrons emitted by a Schottky or Cold Field-Emission Gun (FEG) is a few tenths of an eV or more [57], and phonons therefore fall within the "zero-loss peak" (ZLP) in most microscopes and cannot be detected. Monochromation can reduce the spread in the beam electron energies, however, and the latest monochromation technology has recently begun to provide information about phonons at high spatial resolution [58]. At slightly higher energies, from eV to tens of eV, interband transitions can be detected, which involve transitions across band gaps in insulators and semiconductors, or potentially within a single band in a conductor [56]. These energy losses fall in the energy range of photons in visible light, and can thus be utilized to measure optical properties, for example the optical gap of liquids [41]. Finally, collective oscillations of the valence electrons in the sample can be detected in this energy range as well, and are known as plasma resonances [56]. These resonances were the primary interaction utilized in the low-loss region of the spectrum for the work presented here.

While the valence electron oscillations that define plasma resonances can be described classically by longitudinal waves, excitation of these waves must be described quantum mechanically, and occurs by generation of pseudoparticles called plasmons with discrete energies given by $E_p = \hbar\omega_p$, where $\hbar$ is Planck's constant and ω_p is the frequency of the oscillation (rad/s). While intuition may suggest that these waves should only be generated in materials with free electrons, i.e. metals, the plasmon energy is essentially carried by a single electron at any particular instance, and can therefore exist in any material with electrons capable of transferring energy among themselves [56].

This is consistent with plasmons being excitations of valence electrons, since these electrons extend further away from the atomic nuclei than core electrons, so valence electrons from neighboring atoms therefore have more interactions than core electrons.

Independent inelastic scattering events follow a Poisson distribution, which results in a probability for n scattering events to occur while passing through a sample of thickness t equal to [56]:

$$P_n = (1/n!)(t/\lambda)^n e^{-t/\lambda}, \tag{1.2}$$

where λ is the inelastic mean free path of the beam electrons in the sample material. The resulting distribution of the intensities for zero to two scattering events, as a function of t/λ, is shown in Figure 1.15a. Since plasmons are discrete inelastic events, the total energy loss a beam electron experiences due to plasmon excitations, $E_{p,n} = n\hbar\omega_p$, is just a function of the number of interactions which occur. As seen in Eq. 1.2 and shown in Figure 1.15a, an increased number of interactions occurs in thicker samples. As a result, thin samples generally have a single plasmon peak observable at $\hbar\omega_p$, but thicker samples produce peaks at integer multiples of this value as well. As shown in Figure 1.15b, the integrated intensity of the plasmon peaks fits well to a Poisson distribution in practice [59]. Since thick samples produce plasmon peaks with higher energies, this means that thin samples are essential for measuring low-energy core-loss edges (to be discussed in the next section), since higher-order plasmon peaks will overlap with these edges. This is particularly important for studying lithium battery materials, since the lithium *K*-edge is ~55 eV. Fortunately, the lithium metal plasmon is only ~7.5 eV, so only a very thick sample will cause overlap between the plasmon peaks and the *K*-edge. However, lithium compounds such as lithium oxides have plasmons with energies on

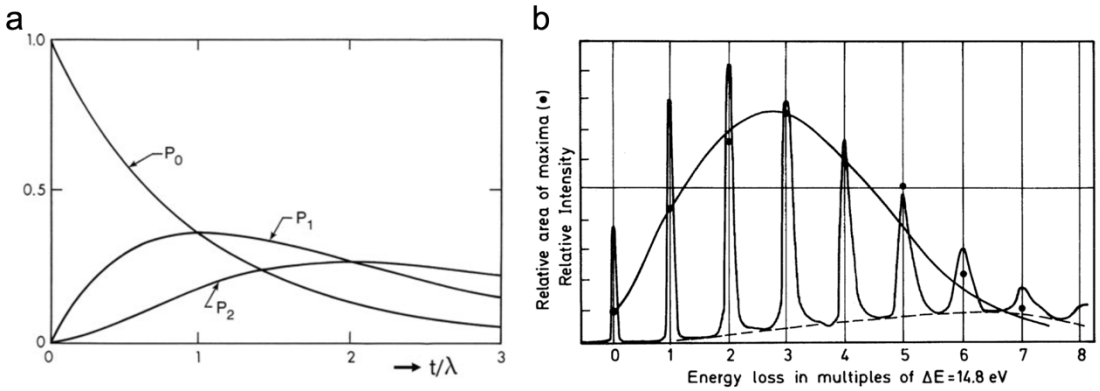

Figure 1.15 Poisson statistics and multiple plasmon scattering. (a) Poisson statistics govern the probability of a certain number of independent inelastic events occurring in a sample as a function of thickness in inelastic mean free paths, t/λ. (b) In thick samples, multiple plasmon excitations occur, and thus form many peaks at multiples of the single plasmon energy. The integrated intensities of these peaks follows a Poisson distribution. Here, a 20 kV electron beam was incident on a 208 nm thick Al film, producing many higher-order plasmon peaks. (a) reproduced from [56], and (b) from [59].

the order of 20 eV or more [60], so significantly thinner samples are therefore needed to avoid overlap in these materials.

By treating the valence electrons as nearly free, the plasma resonance frequency gives a plasmon energy of [56]:

$$E_p = (28.82\ \text{eV})(z\rho/A)^{1/2}, \tag{1.3}$$

where z is the number of free electrons per unit cell (or molecule), ρ is the density of the material (g/cm^3), and A is the atom (molecular) weight of the unit cell (molecule). While this provides a reasonable first approximation to the plasmon energy, as shown in Figure 1.16, other effects can influence the peak locations as well. First, some damping of these "free" electrons occurs in real materials, which causes a broadening and shifting of the plasmon peak to lower energies. If the amplitude of the oscillation is damped by a factor of $1/e$ in a time τ, the full-width at half-maximum (FWHM) of the

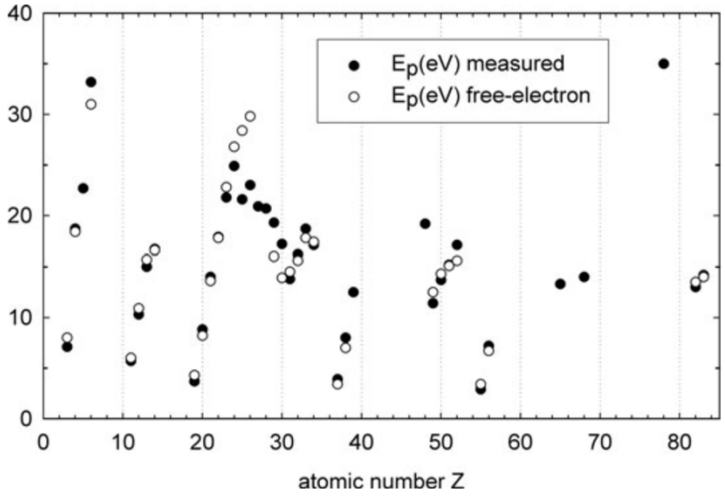

Figure 1.16 Plasmon energies calculated by the free electron model (Eq. 1.3, hollow circles) compared to values measured by EELS (filled circles). The agreement is generally good, with the exception of materials with core-loss edges in the low-loss regions (such as transition metals). Reproduced from [56].

energy-loss function is broadened by a factor of $\Delta E_p = \hbar/\tau$, and is generally in the range of tenths of an eV to multiple eV [56]. The corresponding downward-shifted peak energy is given by:

$$E_{max} = \left[E_p^2 - \left(\Delta E_p^2/2\right)\right]^{1/2}. \tag{1.4}$$

In addition, if large collection angles are used (semi-angle not $\ll \theta_{E_p}^2$, where $\theta_{E_p} = E_p/\gamma m_0 v^2$ and γ, m_0, and v are the Lorentz factor, electron rest mass, and velocity, respectively) momentum transfer from the incident electron to the plasmon can occur, increasing the plasmon energy according to the dispersion relation:

$$E_p(q) = E_p + \alpha\,(\hbar^2/m_0)\,q^2 \tag{1.5}$$

where $\alpha = (3/5)\,E_F/E_p$, and q and E_F are the momentum transfer and Fermi energy of the material, respectively [56].

In contrast, if the valence electrons are bound to the nuclei of the sample, such as in semiconductors and insulators, an additional term enters which shifts the plasmon

energy upwards. If the bound electron has a natural frequency ω_b, then the plasmon is shifted to an energy:

$$(E_p^b)^2 \approx E_p^2 + E_g^2 \tag{1.6}$$

where E_g is the band gap of the material [56]. For materials with large band gaps, this can result in a shift of an eV or more. For example, is we assume 1 valence electron per Li and H atom in LiH, Eq. 1.3 gives $E_p = 12.7$ eV for LiH. If we include a 7 eV band gap, based on experimental values that range from ~5-9 eV [61], the plasmon energy becomes $E_p^b \approx 14.5$ eV according to Eq. 1.6. This is an increase of ~1.8 eV, and estimates the peak energy closer to the experimentally measured value of ~15 eV (see Chapter 4). Finally, interband transitions above or below the plasmon energy can also shift it to lower or higher energies, respectively [56].

While plasma resonances generally do not carry chemical information, they can often be used effectively to map the spatial distribution of materials with low electron doses, since plasmon excitations are the dominant inelastic scattering mechanism for many materials [56], as in the spectrum shown in Figure 1.14. For example, if the plasmon peaks of materials in a sample are distinct, and the materials can be identified by another means like core-loss EELS (to be discussed in the next section), the plasmons can often be used to map the distribution of the materials at lower electron doses than mapping with core-loss edges would require (or with higher signal-to-noise at the same dose). In principle, the plasmon peaks should be more delocalized than core-loss edges, which provide atomic-scale information, but this delocalization is typically less than 1 nanometer [62] and does not impose a limit on dose-sensitive samples such as battery materials.

In Chapter 4 we use this to our advantage to map lithium and LiH materials in two distinct types of dendrites formed in a LMB coin cell. Summing the lithium *K*-edge over large areas produced high signal-to-noise ratio (SNR) spectra that could be used to identify the materials. The signal in individual pixels was low, however, resulting in low SNR maps. The corresponding lithium and LiH plasmons had much higher intensities than the *K*-edges, and were distinct at 7.5 eV and 15 eV, respectively. This allowed us to generate high SNR maps of the two materials within the dendrites by mapping the plasmon peaks.

1.2.1.2 Core-Loss EELS

As the electron beam passes through the sample, excitations of individual core electrons to higher energy orbitals can occur as well. Core electrons often fall hundreds of eV or more below the Fermi level of solids or the HOMO of molecules, and inelastic scattering of the beam provides the required energy to excite these electrons to available states above these levels [56]. Core-loss EELS thus involves measuring the energy losses due to these excitations, which typically result in much higher energy losses than the plasmon peaks discussed previously (as shown in Figure 1.14). An important exception for studying battery materials is the lithium *K*-edge, or 1*s* to 2*p* excitation, which occurs at ~55 eV and can overlap with plasmons if samples are not thin. Since each element has unique orbital energy levels, there are characteristic energies for various excitations that can be used to identify the elements present, as long as no overlap between edges occurs (for example, between excitation from a lower level in a light element and a higher level in a heavier element). In this case, multivariate statistical analysis may still be able to identify and separate the two components if multiple spectra are acquired

(such as in a line profile or spectrum image) [57]. In addition to the characteristic energy of the edges allowing elemental identification, the local environment of the measured element affects the structure of the edge, which allows bonding information to be extracted as well. This can be used, for example, to measure the valence state of electrode materials at different states of charge [63], identify which compounds of an element are present (such as metal, oxides, or hydrides), or examine the bonding environment of SEI layers compared to an electrolyte (see Chapter 4).

The theoretical underpinnings of EELS involve collisions of "fast" electrons with matter, defined as electrons with a velocity much greater than the orbital velocity of the atomic electron with which the interaction occurs [64]. Niels Bohr was the first to work out a theory of the interaction of fast electrons with matter [65,66], but quantum mechanics was not established at the time, and thus some effects could not be calculated. In 1930, Hans Bethe applied quantum mechanics to these interactions [67], laying the theoretical groundwork behind modern core-loss EELS.

To a first approximation, core-loss excitations can be approximated by an interaction between the incident electron and a single atom in the sample [56]. Additionally, in the regime of fast electron collisions, the effect of the incident electron can be approximated by a "sudden and small external perturbation" [64], and as such can be treated using the first Born approximation, using only the lowest order interaction term between the incident electron and the target atom [64,67]. In this case, the differential cross section for a non-relativistic electron to excite an atom from a particular initial state $|\, i \,\rangle$ to a final state $|\, f \,\rangle$ can be written:

$$\frac{d^2\sigma_{ij}}{d\Omega\, dE} = \left(\frac{M}{2\pi\hbar^2}\right)^2 \left(\frac{k'}{k}\right) \left|\langle f \left| V e^{(i\vec{q}\cdot\vec{r})} \right| i \rangle\right|^2, \tag{1.7}$$

where Ω represents the solid angle and E represents energy, V is the interaction potential of the incident electron with the target atom, $M = m_e m_a/(m_e + m_a)$ is the reduced mass of the system where m_e and m_a are the incident electron and target atom mass, respectively, $\vec{k}$ and $\vec{k}'$ are the incident and scattered electron wavevectors, respectively, $\vec{q} = \vec{k} - \vec{k}'$ is the scattering vector, and $\vec{r}$ represents incident electron coordinate. Up to an incident electron energy of around 300 keV [56], a Coulomb potential can be utilized for the interaction of the electron with the atom:

$$V = \frac{Ze^2}{4\pi\varepsilon_0 r} - \frac{1}{4\pi\varepsilon_0} \sum_{j=1}^{Z} \frac{e^2}{\left|\vec{r} - \vec{r}_j\right|}, \tag{1.8}$$

where e is the elementary charge, ε_0 is the permittivity of free space, Z is the atomic number of the target atom, and $\vec{r}_j$ are the positions of the electrons in the atom. The first term represents attraction to the nucleus, and the second term represents repulsion from each of the atomic electrons. Inserting this into Eq. 1.7 gives

$$\frac{d^2\sigma_{ij}}{d\Omega\, dE} = \left(\frac{1}{2\pi a_0}\right)^2 \left(\frac{k'}{k}\right) \left|\left\langle f \left| \Sigma_{j=1}^{Z} \frac{e^{(i\vec{q}\cdot\vec{r})}}{\left|\vec{r} - \vec{r}_j\right|} \right| i \right\rangle\right|^2, \tag{1.9}$$

since the atomic electron states are orthogonal wavefunctions (and hence the nuclear term in the potential integrates to zero). As a result, inelastic scattering events involve only the electrons of the atom, not the nucleus. An additional simplification was made using $a_0 = 4\pi\varepsilon_0\hbar^2/m_e e^2$, where and a_0 is the Bohr radius (and $M \approx m_e$, since $m_e \ll m_a$). Bethe showed that the integral over $\vec{r}$ could be evaluated by substituting:

$$\int \frac{e^{(i\vec{q}\cdot\vec{r})}d\vec{r}}{\left|\vec{r}-\vec{r}_j\right|} = \frac{4\pi}{q^2}e^{(i\vec{q}\cdot\vec{r}_j)}. \tag{1.10}$$

Additionally, only single electron-electron interactions are typically considered for core-loss events, since multiple interactions are considered significantly less probable [68], so we will take $\sum_j \vec{r}_j \rightarrow \vec{r}'$, now a single atomic electron coordinate. The cross section is also relativistically corrected for by addition of a Lorentz factor [69]. Combined, these result in a differential cross section of:

$$\frac{d^2\sigma_{ij}}{d\Omega\, dE} = \left(\frac{2\gamma}{a_0}\right)^2 \left(\frac{k'}{k}\right) \left|\frac{\langle f|e^{(i\vec{q}\cdot\vec{r}')}|i\rangle}{q^2}\right|^2. \tag{1.11}$$

Due to the strong q dependence, small momentum transfers dominate, and typically a small angle ($\vec{q}\cdot\vec{r}' \ll 1$), or dipole, approximation can be taken by expanding $e^{(i\vec{q}\cdot\vec{r}')}$ and keeping only the linear term (the lowest-order constant term goes to zero, due to the orthogonality of the atomic wavefunctions) [56,70]. Additionally, if the scattering angle is small and the beam energy is much greater than the energy transferred during scattering, $k' \approx k$ as well [71]. As a result, the differential cross section becomes:

$$\frac{d^2\sigma_{ij}}{d\Omega\, dE} = \left(\frac{2\gamma}{a_0}\right)^2 \left|\frac{\langle f|\vec{q}\cdot\vec{r}'|i\rangle}{q^2}\right|^2. \tag{1.12}$$

An additional consequence dipole transitions is that these core level excitations must transition to a final state with angular momentum one step higher or lower than the initial state, i.e., $l \rightarrow l' = l \pm 1$. In general, both $l \pm 1$ transitions should be considered, however in some instances, such as excitation from an *s* state, only $l + 1$ can occur, and some transitions strongly favor $l + 1$ over $l - 1$ [72].

EELS edges are labeled based on the principal quantum number of the initial state,

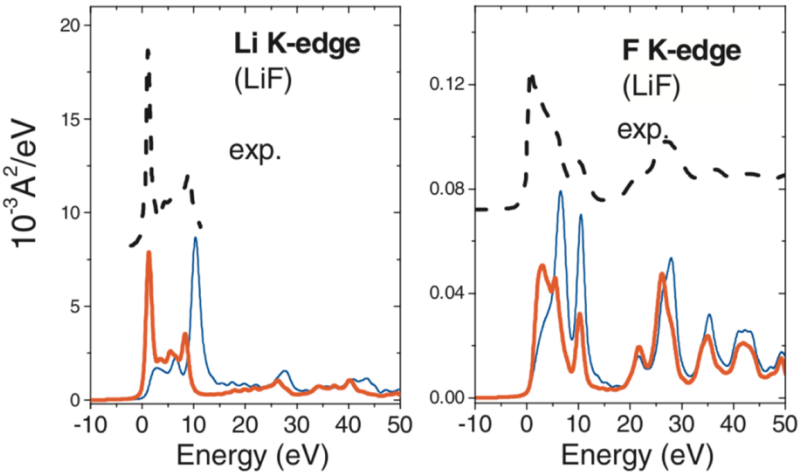

Figure 1.17 An example of the importance of core-hole effects in the spectra of some battery materials. Here, theoretical core-level excited spectra including (red) and not including (black) core-hole effects are shown for the lithium and fluorine *K*-edges of LiF, a material commonly found in lithium batteries. The experimental spectra are shown above in the dashed line. Reproduced from [76].

starting with "*K*" for $n = 1$, "*L*" for $n = 2$, and so on. As a result, *K*-edges are the highest energy edges for a particular element, and decrease through *L*, *M*, etc. The energy of each edge also increases with the target atom's atomic number, since the core electrons sit in deeper potential wells around larger nuclei, and combined with the energy range typically detected in EELS experiments (up to around 2000 eV), this means *K*-edges are often utilized for light elements, and *L*- or *M*-edges for heavier elements.

While each element has well-defined energies for different excitation edges, which can be used to identify the elemental composition of a sample, details about the edge including small shifts in energy and its particular form can provide more information about the sample. In the simplest picture, the entire edge can shift in energy due to a change in charge on an atom. This could be due, for example, to variations in the electronegativity of neighboring atoms, causing a change in the number of electrons on

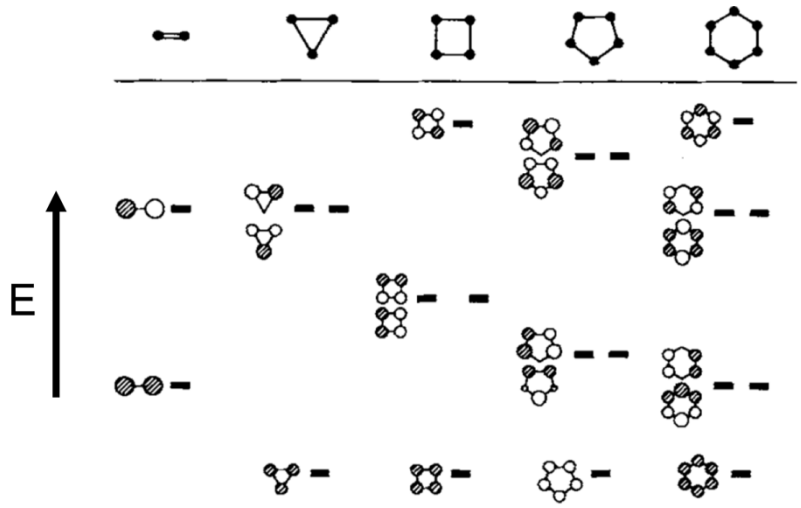

Figure 1.18 An example of the formation of molecular orbital energy levels in a model system containing up to six atoms with only a single atomic orbital (i.e. hydrogen). The size and contrast of the circles represent the magnitude and phase of the orbitals at those locations. Reproduced from [78].

the target atom and therefore the screening of the nuclear potential. This then changes the energy needed to excite an electron to a higher energy orbital further from the nucleus, shifting the edge by up to a few eV [56]. While this often provides a good intuition, the situation can be more complicated and the chemical shifts do not always behave in this way [73]. Additionally, by examining Eq. 1.12, we see that the density of accessible final states around the edge onset energy will define the exact shape of the edge, and this can result in significant modulations of the edge known as its "fine structure." This fine structure can reveal electronic structure, bonding, and crystallographic information about the sample.

The fine structure of EELS spectra can be related to the density of states of the material [56,72]. As discussed above, transitions occur between a core level and empty states above the Fermi level, and also obey the dipole selection rule. The density of states probed by EELS is therefore an angular-momentum-resolved unoccupied density

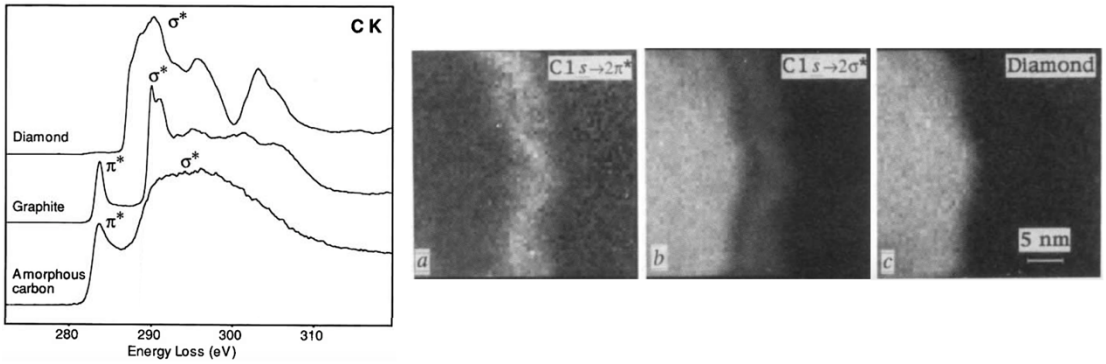

Figure 1.19 Spectra for various allotropes of carbon and nanometer-scale mapping of bonds in these materials. Left, C *K*-edge spectra for diamond, graphite, and amorphous carbon, showing diamond contains no π^* orbitals. Right, mapping of diamond on a silicon substrate with an amorphous carbon layer in between. The distinct σ^* and π^* bond peaks were separately mapped, and the diamond region extracted by subtracting the sp^2 contribution from the σ^* map. Left reproduced from [79] and right from [80].

of states. Additionally, since core electrons are localized to a particular atom, the density of states measured is therefore a local property. This can be used to map bonding states in materials at atomic resolution, for example [8,74]. Finally, the density of states can be modified from its ground-state form by the presence of the core-hole left behind by the excited electron. The importance of this core-hole varies by material, and can often be ignored (for example, in metals) [72]. However, core-hole effects tend to be important for ionic materials, particularly for the cation, and have been found to significantly affect the calculated spectra of some battery materials, such as Li_2O and LiF [75,76]. An example demonstrating this effect for LiF is shown in Figure 1.17.

In materials where electrons are more localized, such as in organic or ionic materials, a tight-binding or linear combination of atomic orbitals (LCAO) approach can be useful for understanding the available states that give rise to the spectra produced by these materials [72,77]. For every pair of atomic orbitals from neighboring atoms combined, a pair of molecular orbitals is formed. The lowest energy molecular orbital

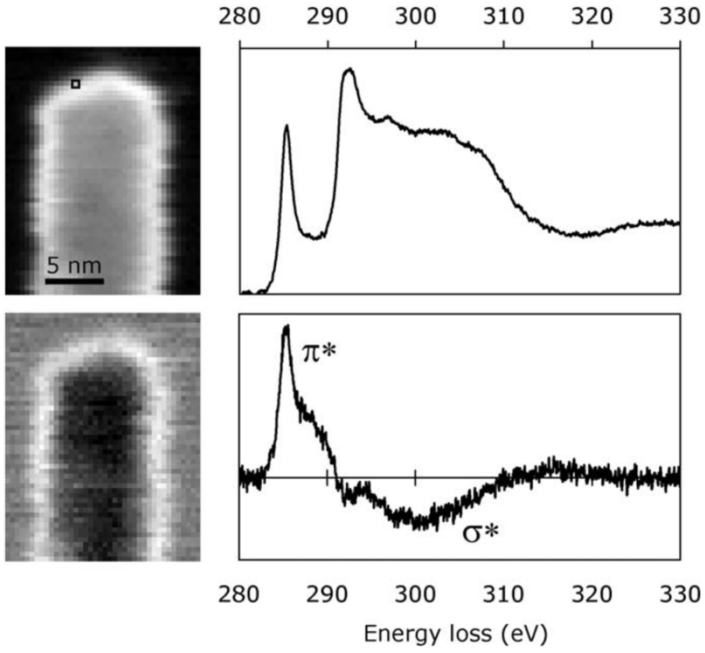

Figure 1.20 Mapping of bond orientations in a multi-walled carbon nanotube. The top spectrum is the average over the whole nanotube, and the second is the first component extracted from a principle component analysis, showing an increased intensity in the π^* peak and a decreased intensity in the σ^* peak. The contrast in the adjacent map shows this corresponds to an increased number of these bonds oriented perpendicular and parallel to the incident beam, respectively, at the edges of the nanotube, and vice versa in the center. Reproduced from [84].

has no nodes in the phase between the atoms. This is known as a bonding orbital, and the electrons reside here in the ground state. When a node in the phase exists between the atoms, this results in a higher-energy state known as an antibonding orbital. These general principles can be extended to larger molecules as well [78], where an increasing number of nodes gives a higher energy state, as shown in Figure 1.18. Bonding and antibonding molecular orbitals that are rotationally symmetric about the axis connecting the atoms are called σ and σ^* states, respectively. Non-rotationally symmetric bonding and antibonding orbitals are denoted π and π^*. The energy levels of the σ/σ^* orbitals tend to split to a larger degree than the π/π^* orbitals since they tend to contain atomic

orbitals that overlap more significantly, and therefore the lowest unoccupied state is often a π^* state. This allows the bonding state of organic materials to be determined by EELS, even when they are composed of a single element. For example, various carbon allotropes such as diamond, graphite, and amorphous carbon, have different carbon-carbon bonds. In particular, diamond contains only σ and σ^* bonds, while graphite and amorphous carbon contain a combination of σ/σ^* and π/π^* bonds [79], as can be seen in the EELS spectra shown in Figure 1.19. Since the energy levels of these types of bonds differ, the ratios of the corresponding peaks in the C *K*-edge can be used to map the location of different carbon materials with subnanometer resolution [80]. For example, the σ^* and π^* C *K*-edge peaks were mapped in amorphous carbon and diamond and used to locate the diamond region in Figure 1.19. In addition to providing information about allotropes of a material, bonds between elements with different electronegativities result in shifted fine structure peaks, and as a result, EELS can be used to differentiate between bonded atoms as well [81,82]. This allows, for example, the local bonding environment of organic materials to be determined and mapped. In Chapter 4, we use this to identify the composition of an intact extended SEI layer formed on a lithium dendrite. Finally, since many of these orbitals are directional, the orientation of these bonds can be detected in anisotropic materials according to Eq. 1.12, within the tight-binding model [71,83]. This enables the orientation of these materials to be mapped as well, as shown in Figure 1.20 [84,85].

One final important point to note for core-loss spectroscopy is that sample thickness impacts the data acquired, which is of particular importance for spectroscopy of beam-sensitive battery materials. Since only a limited dose can be applied to materials that

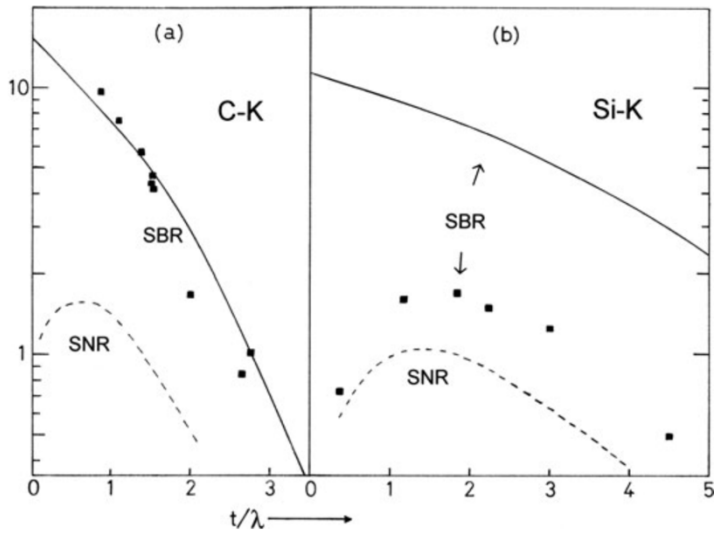

Figure 1.21 Signal-to-background and signal-to-noise ratios of carbon and silicon *K*-edges as a function of sample thickness. (a) For low-energy edges, the SBR decreases monotonically, while the SNR has a maximum at an intermediate value. (b) For higher-energy edges, the SBR can also have a maximum at an intermediate value, due to contributions to the background from the spectrometer. Reproduced from [56].

damage easily under the beam (the mechanisms of which will be covered in the following section), the attainable SNR will therefore be lower than for more robust materials. Optimizing the sample to obtain the maximum SNR possible is then important for beam-sensitive samples. For traditional STEM, very thin samples, on the order of 10-20 nm thick [8], are typical and allow multiple scattering to be avoided and high-quality atomic-resolution spectral images to be acquired. For beam-sensitive samples, however, thicker samples may be beneficial. Thicker samples generate more signal as the beam passes through them, while the damage per unit volume remains the same [86]. While very thin samples may increase the signal to background ratio (SBR) since less multiple scattering is present, the number of counts detected is also decreased, and the SNR is correspondingly decreased due to the increased proportion of shot noise. The background beneath the edges due to single-electron inelastic scattering events

from valence and lower-energy core electrons also increases with sample thickness, however, and multiple scattering effect begin to come in to play. There is therefore an optimal sample thickness for maximizing the SNR of data acquired from beam-sensitive materials. These trends are displayed in Figure 1.21.

1.2.2 Damage Mechanisms in Electron Microscopy

Two of the primary sources of radiation damage exhibited by materials exposed to high-energy electrons are knock-on damage, an elastic collision with an atomic nucleus sufficient to cause displacement, and radiolysis, an inelastic collision with the sample electrons where the excited system does not return to its initial state, and therefore breaks bonds [87]. Specimen charging and heating can also be important in specific instances. Here, we will discuss the details of the most important damage mechanisms, how damage limits imaging and spectroscopy of battery materials, and how cryogenic sample temperatures can help reduce sample damage.

1.2.2.1 Knock-on Damage

Knock-on damage is considered the only type of damage that occurs in conductive materials. This is due to the fact that the high density of mobile electrons enables filling of the hole left by the excited electron in <1 fs, while breaking of bonds requires the hole to be present until the affected nucleus can travel away from its original location, which happens on the timescale of atomic vibrations, ~100 fs [88]. As a result, physical displacement by a transfer of momentum to the atomic nucleus is the only mechanism for damage in conductive materials. The energy transferred to a nucleus by a fast electron through an elastic collision is given by:

$$E = E_{max}\sin^2(\theta/2), \tag{1.13}$$

where θ is the scattering angle of the incident electron, and E_{max} is the energy transferred when the electron is backscattering exactly opposite of the incident direction. This value depends on the atomic mass, A, of the target nucleus, and the incident electron energy, E_0 (in keV):

$$E_{max} = (1.1/A)(2 + E_0/m_e c^2)E_0, \tag{1.14}$$

where $m_e c^2 = 511$ keV is the rest mass energy of the incident electron. For most scattering events detected in the standard TEM diffraction regions, $E < E_{max}/300$, and very little energy is transferred and the atoms are not displaced [88]. As a result of this maximum energy transfer, there is a threshold beam voltage below which displacement of atoms by knock-on damage cannot occur. If an energy E_d (in eV) is required to displace an atom in a material, the threshold beam energy for displacement can be conveniently written:

$$E_0^{th} = (511 \text{ keV})\left([1 + AE_d/(561 \text{ eV})]^{1/2} - 1\right). \tag{1.15}$$

Since this threshold energy depends on the energy required to displace an atom, less strongly bound atoms at the surface of a sample will typically be displaced more easily than those in the sample interior. If this occurs on the bottom surface of the sample, atoms can be sputtered out of the sample and mass loss can occur. For most materials, the threshold for knock-on damage is above 100 keV, and for many materials it is 200 keV or greater. Thresholds for surface sputtering, however, are often below 100 keV [86].

While a beam energy below these threshold values can be chosen to prevent atomic displacement in many materials, this may not be true for those used in batteries. Since

high energy density is a goal for many batteries, light materials are often sought for electrodes, such as lithium metal. It is clear in Eq. 1.15 that for a given displacement energy, decreasing the atomic mass of target atoms will decrease the threshold beam energy, making it difficult to eliminate knock-on damage of light atoms. For example, the threshold voltage for preventing sputtering from the lower surface of lithium is just above 5 kV, and therefore any TEM voltage used will inevitably cause some mass loss [86]. While many organic materials, such as electrolytes commonly used in batteries, contain light elements as well, knock-on damage typically contributes significantly less to overall damage of these materials than radiolysis (discussed below), with a cross section up to 10^5 times smaller than inelastic events [88]. Hydrogen in these materials, however, may be more strongly affected [87,88]. In organic materials, the C-H bond energy is generally ~3.5-5.5 eV [89], and combined with hydrogen's low mass, the resulting threshold energy for displacement is very low, at around 2 keV according the Eq. 1.15, and knock-on damage is thus increased. For example, the cross section for this type of knock-on damage is less than 10^3 times lower than values of radiolysis in copper phthalocyanine [88]. Combined with the fact that not all inelastic events break a bond, knock-on damage of hydrogen may contribute appreciably to damage in organic materials.

1.2.2.2 Radiolysis

In contrast to knock on damage in conductors, radiolysis is the most prominent source of damage in insulating materials. This is especially true for organic materials and alkali halides [86], both of which are important for batteries as electrolyte and SEI layer materials [90–93]. Since insulating materials do not contain free electrons like

conductors, the system may not relax to its initial electronic state before the nucleus has had time to physically move. When this occurs, the system relaxes to a new state and the affected bond is broken, causing damage. As mentioned previously, the cross section for radiolysis in these types of materials can be up to 10^5 higher than for knock-on damage, though not every inelastic excitation results in a broken bond, so the relevant value would be lower than this [88]. Radiolysis is generally still considered the predominant damage factor for insulating samples, however.

The rate at which radiolysis occurs can vary widely between different organic compounds, but is typically more rapid for aliphatic than aromatic compounds, likely due to the stability of the ring structures that contain π-electrons with a high resonance energy [87]. Additionally, loss of hydrogen is known to be particularly quick compared to many other elements in organic materials [87]. This may result from the fact that hydrogen can only form one single-bond, and its increased sensitivity to knock-on damage.

Damage can typically be characterized by a "critical dose", at which some measure of the sample's structure begins to appreciably degrade [86], and different critical doses can be defined for different structural or electronic changes that occur within the sample [87]. The critical dose for reducing the long-range order of a sample, measured by damping of diffraction peaks, is typically the lowest. This initial structural change may be due to loss of hydrogen from the sample, since hydrogen is known to be particularly prone to mass loss as discussed above. As evidence for this, it has long been known that substituting other elements for hydrogen in organic molecules significantly decreases their dose sensitivity. For example, substituting the peripheral hydrogens with halogen

atoms in the organic molecule Cu-phthalocyanine increases its critical dose by an order of magnitude [59]. At higher doses, notable mass loss begins to occur, as other elements begin to be liberated as well. The corresponding change in sample thickness can be monitored by a reduction in the magnitude of the signal recorded by various techniques (such as annular dark-field STEM, EELS, or EDX). Appreciable changes in short-range molecular order due to a high number of bond breakages typically require the most dose, and can be observed by changes in the fine structure of EELS edges [87,94]. In order to accurately characterize the bonding environment of battery materials, it is necessary to keep the applied electron dose below this final critical value, which we have measured on the order of 10^3 $e^-/Å^2$ for the organic electrolyte material used in Chapter 4, and an order of magnitude or more higher for the lithium compounds tested, which are considered "beam-sensitive" compared to traditional STEM samples [95].

1.2.2.3 Benefits of Cryogenic Techniques for Damage

In addition to preserving the native structures and liquids at solid-liquid interfaces, cryogenic sample temperatures can reduce the critical dose for damage observed in materials. Cooling the sample to liquid nitrogen temperature has been observed to raise the critical dose by a wide range of factors, often 2-3 times, but up to a maximum of 10^2 for some materials [87]. This can be explained by the decreased atomic velocities and diffusion rate in the sample, likely resulting in fewer broken bonds by radiolysis, since the atoms move away from their equilibrium sites more slowly, and constricting their movement after the bond is broken, preventing mass loss. In fact, it has been shown that mass lost does occur after warming samples exposed to the beam back to room temperature, with no additional beam exposure, since the ability for the atoms with

broken bonds to diffuse out of the material is restored [96]. Additionally, coating TEM samples with thin layers of different materials, typically carbon or metals, has also been shown to decrease mass loss in samples by up to a factor of around five, possibly by forming a barrier to diffusion of light elements out of the sample [87]. At cryogenic temperatures, thin amorphous ice layers can be deposited on the sample surface from trace water contaminants in the vacuum, and these may act as protective barriers and increase the critical dose of the sample as well.

Finally, while not technically a damage mechanism, the composition of reactive materials can become altered during preparation, transfer, or in the microscope itself, due to reactions with the atmosphere or trace molecules in the vacuum, and is often accelerated by the electron beam. For example, lithium is known to react with trace water or oxygen molecules in the TEM column under exposure to the beam at room temperature, forming lithium oxide [60]. This has significant implications for both the ability to characterize many battery materials and the accuracy of the results produced. Use of cryogenic techniques can enable highly air sensitive materials to be characterized in their native state without compositional changes as well. For example, by utilizing cryogenic sample preparation and transfer techniques we were able to study the lithiation processes in monolayer MoS_2 at the atomic-scale, as shown in Figure 1.22. Due to the highly reactive nature of the lithiated materials, preparation and transfer at room temperature would have compromised the structure and chemistry of the samples.

To gain an intuition for why cryogenic temperatures provide this protection against chemical reactions, we will briefly discuss the mechanism for the slowing of reaction

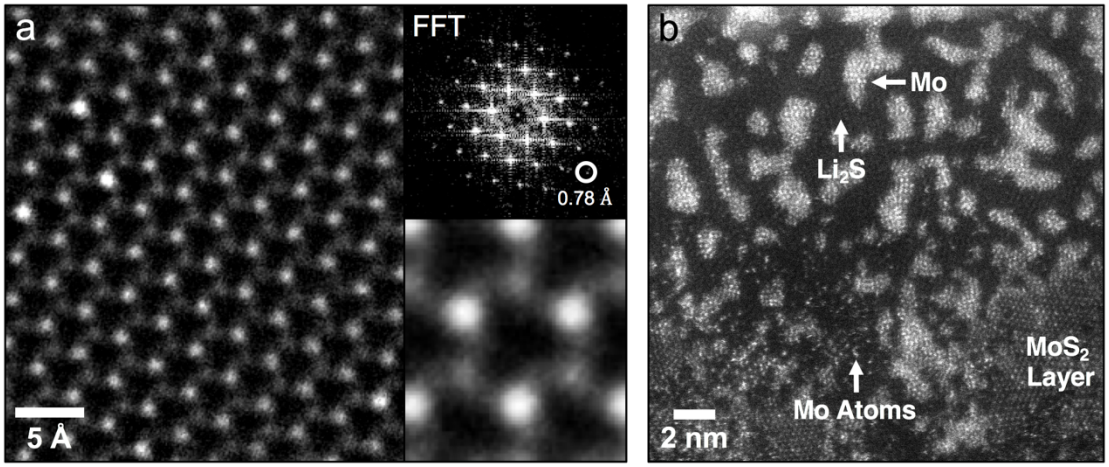

Figure 1.22 Atomic-scale study of lithiation processes in a monolayer MoS_2 cathode material. (a) Annular dark-field cryo-STEM image of a pristine MoS_2 monolayer, with 0.78 Å resolution, and the corresponding fast Fourier transform and averaged structure. (b) Annular dark-field cryo-STEM image of a transition region in a lithiated MoS_2 sample. In the unreacted region the MoS_2 layer can still be observed. In the transition region, individual Mo atoms are present, and in the fully reacted region the material is converted to Mo and Li_2S nanoparticles. Images were acquired with a 120 keV beam.

rates at low temperature. In order to react, two atoms must cross an energy barrier separating them, with a height defined as the activation energy [11]. Assuming N is the frequency of atomic interactions and the kinetic energies of the atoms follow a Boltzmann distribution, the rate of interactions between atoms with energy sufficient to cross the barrier should be Ne^{-E_a/k_BT}, where E_a is the activation energy and k_B is Boltzmann constant. This is, in fact, the form of the empirical Arrhenius Equation, which governs the rate constants of chemical reactions [11]. The change in reaction rate as a function of temperature is highly dependent on the activation energy of the reaction, dramatically increasing with increased activation energies.

As an example, we can choose a relatively low activation energy of 0.25 eV (appropriate for $2Li + 2H_2O \rightarrow 2LiOH + H_2$, for example [97]) and do a back-of-the-envelope calculation to compare the time for the full sample surface to react. By

normalizing the Boltzmann distribution (to $e^{-E_k/k_BT}/k_BT$, where E_k is the kinetic energy of the atoms), we see the probability of an atom having a kinetic energy higher than the activation energy is ~10^{-4} at 300 K and ~10^{-13} at 100 K. The kinetic theory of gases says that the frequency of gas molecule collisions with a surface, per unit area, is $f = n\langle v\rangle/4$, where n and $\langle v\rangle$ are the density and average velocity of the particles in the gas, respectively. Combining this with the ideal gas law, $P = nk_BT$, and assuming atmospheric pressure, an average velocity equal to the speed of sound in air, and an average sample surface atom spacing of 4 Å, we can estimate the time for every surface atom to be impacted by a gas molecule, on the order of a nanosecond. Assuming any atom in the gas with sufficient energy to react (the probabilities of which were estimated above) will do so upon contact with a gas molecule, we can finally estimate the time necessary for every surface atom to react. At room temperature (300 K) and 100 K, this is on the order of 10 milliseconds and 10^4 seconds, respectively. While the situation is undoubtedly more complicated in reality, this simple model illustrates clearly how cryogenic sample temperatures can significantly reduce reaction rates and enable transfer without significant compositional changes. Additionally, since the pressures in the FIB and STEM are nine orders of magnitude or more lower than atmosphere [7,98], the reaction times would be correspondingly reduced after transfer. Finally, by reducing the average kinetic energy of the atoms in the sample by cooling, the fraction of elastic collisions that transfer sufficient energy to cause a reaction is reduced as well. We have observed that reactive materials such as lithium can withstand exposure to fairly high doses with little reaction, in agreement with other recent studies [95,99]. As part of Chapter 4, we carefully characterize the critical doses for EELS fine structure changes

in a variety of lithium battery materials at cryogenic temperatures, such as lithium metal, hydride, and oxides.

1.2.3 Cryogenic Electron Microscopy Techniques

With the primary objective of preserving structures and chemistry at solid-liquid interfaces for high-resolution characterization, and with the added benefit of reducing sample damage, the work described here involves applying cryogenic electron microscopy and focused ion beam techniques to systems that contain such interfaces. In this section, we will introduce the basic physics of vitrification, or rapid sample freezing to preserve a liquid in an amorphous state, describe some common techniques that enable vitrification, and outline previous applications of cryogenic techniques used to enable electron microscopy of biological specimens.

1.2.3.1 The Physics of Sample Vitrification

While water molecules are attracted to each other due to their dipole moments, thermal motions at room temperature are sufficient to prevent large-scale crystallization, and the water remains a liquid. As the temperature of the water is decreased, small clusters of a few molecules form, which may then nucleate formation of larger crystals [100]. Molecules on the interior of these crystallites contribute negatively to the free energy of the structure, and assuming this structure is spherical with radius r, this contribution is proportional to r^3. Molecules on the surface of the crystallite are less stable, however, and contribute positively to the free energy of the structure, proportional to r^2. Since the total free energy of the structure is the sum of these two factors, the small crystallites that form are not stable, as shown in Figure 1.23. In order for the crystallite to grow, the

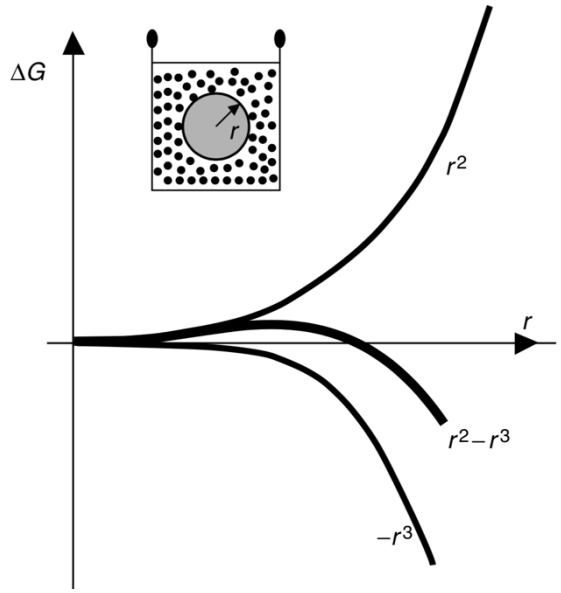

Figure 1.23 Free energy of a crystallite in a liquid. Molecules on the interior contribute negatively, proportional to r^3, while molecules on the surface contribute positively, proportional to r^2. The total free energy is therefore only negative above a critical size, and small crystallites are not stable. Crossing the threshold size results from random statistical fluctuations and does not occur frequently, but once above the critical size it is energetically favorable for the crystallite to grow, solidifying the liquid. Reproduced from [100].

size must cross a certain threshold where the r^3 factor becomes larger than the r^2 factor, and increasing the size of the crystallite becomes energetically favorable. Since small crystallites are not stable, crossing the threshold size is due solely to statistical fluctuations, and does not occur frequently. As evidence for this, up to ~10^9 water molecules can be cooled to liquid nitrogen temperature fast enough (around one millisecond) to be frozen without crystallization. This means every one of the billion molecules has time to move between roughly one billion positions, but no nucleation of large crystals occurs [100]. Once nucleation does occur, however, the crystallite will grow until the liquid fully crystallizes into a solid.

Once the critical cluster size is achieved and nucleation of crystallization begins, the

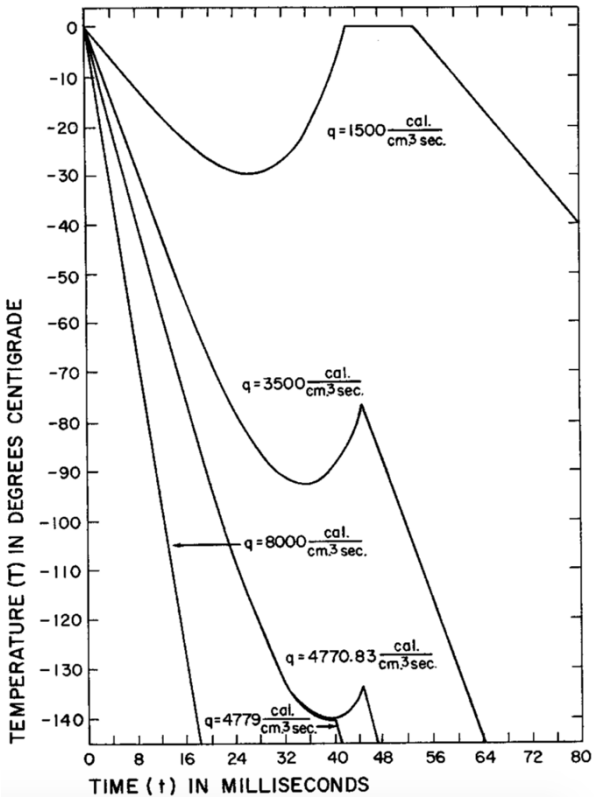

Figure 1.24 Theoretically calculated temperature of water as a function of time for different cooling rates. The heat of crystallization can warm the growing ice crystals, up to a critical cooling rate, where energy is removed sufficiently fast to enable vitrification. Reproduced from [101].

growth rate is self-limiting. As molecules are added to the growing crystal, they deposit energy into the structure, and this added energy can be sufficient to raise the temperature of the crystal, as can be seen in Figure 1.24 [101], resulting in a maximum rate of crystal formation that depends on the rate of cooling. By cooling more rapidly than a critical rate, however, the molecules don't have time to nucleate and crystallize, and the result is an amorphous solid. This process is known as vitrification, and for pure water requires a cooling rate of around 10^4 K/s or more to achieve [102]. Thus, when cooling to liquid nitrogen temperature (77 K) from room temperature, the full temperature drop must be achieved in on the order of 10 milliseconds or less. Since heat must be conducted out of

the interior of a sample during this process, larger samples have reduced cooling rates, and this limits the physical size of a sample that can be vitrified to around one micron thick water layers or droplets of a few microns in diameter [100]. Additionally, while the heat transfer near the surface of samples may be greater than the interior, there has been no conclusive evidence that even surface layers on larger samples can be vitrified, likely due to heat released in the interior devitrifying the surface layer [100]. While vitrification of pure water is limited to layers around one micron thick, this can be increased by methods such as introducing a solute or increasing the pressure during cooling [100,102].

Vitrifying a sample preserves it in nearly its native state, which is critical for accurate characterization. In order to maintain a sample in a vitreous state, however, it is not sufficient to simply keep the temperature below the melting point. Vitreous ice is metastable, and sufficient thermal motion of the atoms can enable them to reorient into small crystals, a process known as devitrification, which occurs in pure water around 140 K [100]. Once devitrification has occurred, the nucleation sites can result in large-scale ice crystal growth, or recrystallization [102]. Devitrification and recrystallization can cause structural damage to samples, and are therefore important to avoid. As a result, frozen-hydrated samples must be maintained below approximately 140 K during preparation, storage, transfer, and experiments.

1.2.3.2 Sample Vitrification Techniques

A common method for vitrification of thin samples is plunge freezing, where a sample is “plunged” into a liquid cryogen, typically on a holder accelerated by gravity or a spring. Thin liquid layers up to around one micron thick on copper TEM grids can be

vitrified by this method [102]. While liquid nitrogen is usually used to cool the region where samples are frozen, it does not provide a sufficient cooling rate to do the sample vitrification itself due to the Leidenfrost effect, or formation of an insulating gas layer around the sample. This is because the liquid nitrogen is at its boiling point, so any heat added immediately boils the liquid. As a result, other cryogens, typically liquefied organic gases such as propane or ethane, are used [102]. These liquids have a higher boiling point and are cooled by the liquid nitrogen, and therefore don't form an insulating gas layer upon contact with the sample. Unfortunately, these materials also solidify above liquid nitrogen temperature, and in pure form require heating to use. A mixture of these materials has a melting point below liquid nitrogen temperature [103], however, so this mixture is commonly used for vitrification of thin aqueous solutions on TEM grids by plunge freezing.

It has been shown, however, that organic cryogens dissolve or etch organic liquids in the process of vitrification [104–108], which we have observed as well. As a result, these preferred cryogens cannot be used to vitrify many common lithium battery electrolyte materials. Fortunately, many organic liquids require significantly lower cooling rates for vitrification than aqueous solutions [105,108], and alternative cryogens can be used. For our battery work, we have chosen to vitrify samples using slush nitrogen, which is a mixture of solid and liquid nitrogen at its melting point, 63 K, produced by vacuum pumping on liquid nitrogen. Since this nitrogen is not at the boiling point the cooling rate is increased [102], and we have found that this allows organic electrolyte layers on the surface of large samples such as metal battery electrodes to be vitrified (see Chapters 2 and 4).

As mentioned previously, increased pressures during freezing allow larger sample volumes to be vitrified. An additional technique used for vitrification is therefore called high-pressure freezing, and involves subjecting the sample to a room-temperature jet of liquid propanol at up to approximately two-thousand times atmospheric pressure, followed milliseconds later by a jet of liquid nitrogen, which cools the sample [102]. This allows vitrification to a depth of around ten microns in pure water, but up to hundreds of microns in other hydrated samples, such as tissues. While this technique was not used for the work presented here, if microbatteries with liquid electrolytes could be produced, we could envision utilizing high-pressure freezing to vitrify the device without disassembly, which would allow, for example, preparation of cross sections containing the full width of the battery cell by cryo-FIB lift-out (see Chapter 3).

1.2.3.3 Previous Applications in Biology

Use of cryogenic techniques in electron microscopy is not a new concept. In fact, it has been used since the 1980's to image small biological molecules in thin aqueous solutions vitrified on TEM grids, such as the T4 bacteriophages as shown in Figure 1.25a [10]. Today, great strides have been made in cryo-TEM, and "single-particle" techniques now allow the 3D structure of biological molecules such as proteins to be reconstructed down to nearly the atomic scale, as shown in Figure 1.25b [109]. In fact, cryo-TEM has become such an integral tool for structural biology that three early cryo-electron microscopists recently won the Nobel Prize in Chemistry for "developing cryo-electron microscopy for the high-resolution structure determination of biomolecules in solution" [110]. While these cryogenic techniques have been very successful for studying the structure of small molecules in their native environment, larger biological

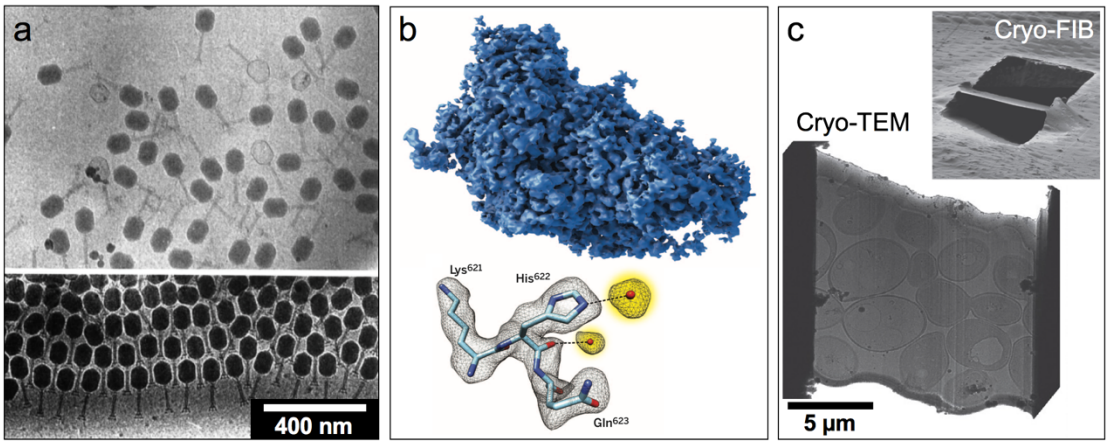

Figure 1.25 Cryogenic electron microscopy of biological specimens. (a) Since the 1980's cryo-TEM has been used to image small biological molecules in thin aqueous solution layers vitrified on TEM grids, such as the T4 bacteriophages here. (b) Today, techniques such as single-particle cryo-TEM allow nearly atomic resolution 3D reconstructions of the structure of biological molecules such as proteins, like this β-galactosidase with its structure determined to 2.2 Å. (c) For thicker samples, cryo-FIB thinning techniques give cryo-TEM access to the interior structure of cells, for example. (a) reproduced from [10], (b) from [109], and (c) from [111].

specimens, such as cells, cannot be directly imaged after vitrification on a TEM grid and must undergo further preparation. The traditional method for preparing thin sections from thicker biological materials is cryo-ultramicrotomy, which involves shaving thin slices from a frozen specimen with a diamond blade, but this technique is non-site-specific and physically cutting the sample results in many artifacts [10]. As a result, cryo-FIB techniques have recently been developed to enable site-specific thinning of biological materials to electron transparency on a TEM grid, as shown in Figure 1.25c [111]. Additionally, initial reports of cryo-FIB lift-out techniques have now been demonstrated [112–114], which allow preparation of even larger biological specimens for cryo-TEM by extraction of electron transparent cross sections, analogous to room temperature FIB lift-out, which is commonly used to prepare solid samples for TEM and STEM [7].

1.3 Thesis Outline

While cryogenic electron microscopy techniques have been very successful in the biological sciences, they have thus far not contributed significantly to the physical sciences. In this thesis, adaptation of a variety of cryogenic electron microscopy and focused ion beam techniques for high-resolution characterization of intact solid-liquid interfaces in bulk materials and devices is described, including cryo-FIB/SEM, cryo-FIB lift-out, cryo-TEM, and cryo-STEM/EELS techniques, and initial results obtained by these techniques are presented.

Chapter 2 describes how cryo-FIB milling paired with cryo-SEM imaging and spectroscopic techniques allows the structure and elemental concentrations at intact solid-liquid interfaces in devices such as batteries to be revealed. The benefits of cryogenic techniques for transfer, FIB milling, and characterization of solid-liquid interfaces and reactive materials are demonstrated, and limitations of the technique are discussed.

Chapter 3 discusses the details of a cryo-FIB lift-out technique for preparing electron transparent cross sections of intact solid-liquid interfaces from bulk materials and devices for cryo-STEM characterization. Additionally, it outlines methods for locating and extracting structures buried beneath the surface, and presents the first analytical cryo-STEM data produced from cryo-FIB lift-out samples.

Finally, Chapter 4 demonstrates the first pairing of cryo-FIB/SEM, cryo-FIB lift-out, and aberration-corrected cryo-STEM/EELS techniques, which were utilized to reveal the structure and composition of unaltered lithium dendrites and their intact SEI

layers in lithium metal battery coin cells for the first time. Two distinct dendrite morphologies are identified using cryo-FIB/SEM, and cryo-FIB lift-out is used to prepare dendrite-electrolyte interfaces for nanoscale structure and bonding studies by cryo-STEM/EELS. Using these techniques, the two dendrites types are discovered to be composed almost uniformly of lithium metal and lithium hydride, which has not been observed before. Additionally, the lithium metal dendrites have an extended SEI layer around 400 nm thick, much larger than previously thought, and is likely composed of lithium ethylene dicarbonate. Using the results obtained, potential pathways to inhibit formation of LiH dendrites are proposed, and proof-of-principle experiments are performed to verify these ideas.

CHAPTER 2

NANOSCALE IMAGING AND ELEMENTAL MAPPING OF INTACT SOLID-LIQUID INTERFACES AND REACTIVE MATERIALS IN ENERGY DEVICES ENABLED BY CRYO-FIB/SEM

Many modern energy devices rely on solid-liquid interfaces, highly reactive materials, or both, for their operation and performance. The difficulty of characterizing such materials means these devices often lack high-resolution characterization in an unaltered state. Room temperature FIB/SEM routinely enables nanoscale surface and cross-sectional characterization of solid devices, but is limited to dry samples and non-reactive materials. Here, we demonstrate the extension of FIB/SEM techniques to samples including reactive materials and solid-liquid interfaces common to energy devices by utilizing cryogenic sample temperatures. We show that this allows liquids at solid-liquid interfaces to be preserved, chemically reactive samples to be transferred into the instrument without reaction with the environment, and clean milling to be performed in materials typically problematic at room temperature, such as lithium. Additionally, we demonstrate the ability of cryo-FIB/SEM to achieve nanoscale structural and elemental characterization of reactive materials and intact solid-liquid interfaces in devices by performing imaging and spectroscopic mapping on cross sections produced in these materials. Our results suggest that cryo-FIB/SEM will be a useful technique for many fields where solid-liquid interfaces or reactive materials play an important role and could thus far not be characterized at high resolution in an unaltered state.

2.1 Introduction

Devices that rely on solid-liquid interfaces or reactive materials are ubiquitous in modern society, and will continue to play an important role in the future. Examples are dye-sensitized solar cells for energy generation [115], fuel cells for electrolysis and conversion of fuels to electricity [116], and supercapacitors and batteries for energy storage [5,117]. Energy devices such as these, however, present a problem for characterization since they contain liquids and/or highly reactive materials. Typically, liquids are removed from such samples before characterization in high-vacuum instruments to prevent immediate evaporation. The associated washing and drying process can result in structural and chemical modifications of soft or brittle materials present at the sample interface, however [9]. Additionally, samples containing highly reactive materials, such as alkali metals, present additional challenges for characterization since exposed regions react quickly with air during transfer to the instrument or with contaminants in the vacuum during characterization, altering the sample's surface chemistry [60].

While the devices mentioned above are macroscopic in size, the electrode structures and processes at the solid-liquid interfaces inside may have features down to the nanoscale [118]. A technique capable of bridging this significant size gap is therefore needed to study these features within actual devices. Focused ion beam/scanning electron microscopy (FIB/SEM) techniques combine the milling capability of a FIB with the imaging and spectroscopic capabilities of an SEM to enable nanoscale characterization of surface and cross-sectional structures on samples up to tens of centimeters in size [7]. These techniques are used commonly in both academia and

industry for characterization, failure analysis, and editing of solid devices such as silicon wafers and integrated circuits, micro-electrical-mechanical systems, and solid-state batteries [7,119–121]. Despite the power and versatility of FIB/SEM techniques, they are currently limited to solid samples due to the issues discussed above, and non-reactive materials due to interactions with the gallium beam.

Here, we demonstrate the extension of these FIB/SEM capabilities to devices that include solid-liquid interfaces and reactive materials by adapting cryogenic-electron microscopy techniques traditionally used for imaging small biological molecules and cells [10,111]. We show that by rapid freezing and careful sample transfer into the instrument, liquids and soft materials present at interfaces are preserved, and exposed reactive materials experience minimal reactions during transfer. Additionally, the cryogenic sample temperature suppresses the chemical kinetics of reactive materials sufficiently to be milled without significant interactions with contaminants in the vacuum or alloying with the gallium ions, as is the case at room temperature. We demonstrate these techniques using bare lithium metal electrodes, lithium deposited on an electrode with an artificial solid-electrolyte interphase (SEI) layer in a coin cell battery, and aqueous solution-solid oxide interfaces. By performing imaging and spectroscopic mapping on cross sections produced by cryo-FIB milling, we reveal the morphology and elemental composition of the unaltered materials and intact interfacial layers present, and demonstrate that these features can be characterized down to the nanoscale. We also discuss the limitations of these techniques and future developments that could broaden the capabilities of cryo-FIB/SEM.

2.2 Materials and Methods

To enable the use of cryogenic sample temperatures in our FIB it was outfitted with a Quorum Technologies, Inc. PP3010T Cryo-FIB/SEM Preparation System. This system includes a cold stage and anticontaminator in the FIB, as well as a preparation chamber with a separate cold stage and anticontaminator, a workstation and liquid nitrogen pot, and a vacuum transfer device. Frozen samples are transferred from the workstation to the preparation chamber via the vacuum transfer device. Once in the preparation chamber, techniques such as metal sputter coating can be performed. The samples are then shuttled into the FIB chamber through a valve connecting the preparation chamber to the FIB. The cold stages in both the preparation and FIB chambers maintain the sample near liquid nitrogen temperature, typically -165 ˚C, while the anticontaminators are set at -192 ˚C to preferentially adsorb contaminants in the vacuum.

To immobilize liquids present in samples, rapid freezing in a liquid or slush cryogen is used. Consideration of the type of liquid in the sample is necessary for choosing an appropriate cryogen. If the liquid in the sample must be vitrified, or preserved in an amorphous state, the cooling rate must be larger than a critical value [10,102] that depends on the liquid being frozen. Aqueous solutions are typically frozen in liquefied organic gasses, such as propane, ethane, or a mixture of the two [103], since they generate higher cooler rates than liquid or slush nitrogen [102]. If the sample contains organic liquids, however, organic cryogens can dissolve this material during the freezing process [104,105,107,108,122]. As a result, an alternative cryogen that does not interact with organic liquids must be chosen for these samples. Here, we use slush nitrogen for this purpose, which is produced by vacuum pumping on liquid nitrogen

until it solidifies, and returning it to atmospheric pressure. This results in a slush containing both solid and liquid nitrogen, with an enhanced cooling rate compared to liquid nitrogen since the Leidenfrost effect is avoided. Although slush nitrogen has a cooling rate lower than organic cryogens, the rate necessary for vitrification of organic liquids is less than that of aqueous solutions [105,108]. As a result, we have found that organic electrolyte up to at least microns thick on the surface of large samples such as coin cell battery electrodes can be vitrified by plunge freezing in slush nitrogen.

Once the sample is frozen in the workstation, it is placed on a shuttle and the vacuum transfer device is attached to the liquid nitrogen pot. The transfer device is then pumped to a moderate vacuum (approximately three orders of magnitude below atmospheric pressure), the shuttle is retracted into the transfer device and sealed inside of a small vacuum chamber, and it is transferred to the preparation chamber attached to the FIB. Here, the sample surface is typically coated with 5-10 nm of metal, either platinum or gold-palladium, to increase sample conductivity. Once this process is complete, the sample is transferred through a valve to the cold stage in the FIB chamber.

In the FIB, imaging or spectroscopic mapping by energy dispersive X-ray spectroscopy (EDX) can be immediately performed on the sample to locate regions of interest. In certain cases, even subsurface features can be localized, since the accelerating voltages used enable the beam to penetrate below the sample surface [123]. The sample surface is then tilted perpendicular to the Ga^+ ion beam and a cross section is milled site-specifically at the point of interest. Cross sections are typically ten or twenty microns deep and of similar width, though larger or smaller regions can be milled based on the material properties and the patience of the user. Milling typically takes

place in two steps. First, a "regular cross section" is milled at high beam current, on the order of nanoamps, to quickly remove a large amount of material. This milling pattern results in multiple passes over the defined area, with an increased number near the cross section surface, resulting in a trench with a depth gradient. While this removes material quickly, a layer of redeposited material can be left on the final cross section surface. To remove this material, a "cleaning cross section" is used, which makes a single slow pass over the defined milling area, ending with a final mill at the cross section surface, which leaves it free of redeposited material. This final step can also be performed with a lower ion beam current to reduce probe tails, minimizing the "curtaining" effect that produces a rough final cross section surface. Some materials, however, produce redeposited material that cannot be effectively removed by such a final cleaning step. In this case, a single cleaning cross section must be used to mill the entire trench, including the final surface, in one pass.

To further increase the quality of the final cross section surface when milling frozen soft or liquid samples, deposition of a platinum material on the sample surface prior to milling can be used, as has been shown for biological samples [124]. Site-specific deposition of platinum metal is used regularly to aid room temperature preparation of TEM samples by FIB [7], but cryogenic sample temperatures result in the organometallic platinum precursor gas adsorbing to the sample surface. This results in an extended and non-site-specific deposition of the material. This broadly deposited material still has beneficial qualities for milling, however, and a deposition of around 2-3 μm provides sufficient protection from probe tails to significantly reduce curtaining. Unlike platinum metal, this organometallic material is non-conductive and charges

under the electron beam without additional processing. To address this, a "curing" process is performed, where the material is exposed to the ion beam [124]. This exposure releases the organic portion of the molecule near the surface of the material while leaving the platinum behind, resulting in a conductive surface. Using these techniques results in a clean and smooth final cross section surface that allows accurate high-resolution imaging and spectroscopic mapping to be performed.

2.3 Results

2.3.1 Transfer of Reactive Materials into the Instrument

To prepare coin cell batteries for characterization by cryo-FIB, the cells are manually opened, and the electrode of interest removed for plunge freezing. A schematic of a typical coin cell configuration is show in Fig. 2.1a. For many experiments, the reactive electrode surface is protected from interaction with the air during the brief transfer into the slush nitrogen pot by the liquid electrolyte on its surface. In order to test the minimum rate of transfer needed to avoid contamination under any conditions, however, we prepared dry coin cells with bare lithium metal electrodes inside. Electrodes that were removed from the cells and immediately plunge frozen in slush nitrogen showed no signs of contamination, as shown in Fig. 2.1b. Intentionally exposing the electrodes to air for approximately one minute prior to plunge freezing resulted in oxide formation initiating at specific locations on the surface, such as grain boundaries. An example of one of these oxide growths is shown in Fig. 2.1c, with the corresponding oxygen EDX map. An EDX spectrum of the lithium surface is also shown in Fig. 2.1d. Additionally, while molecular nitrogen is generally considered inert due to its strong triple bond, the

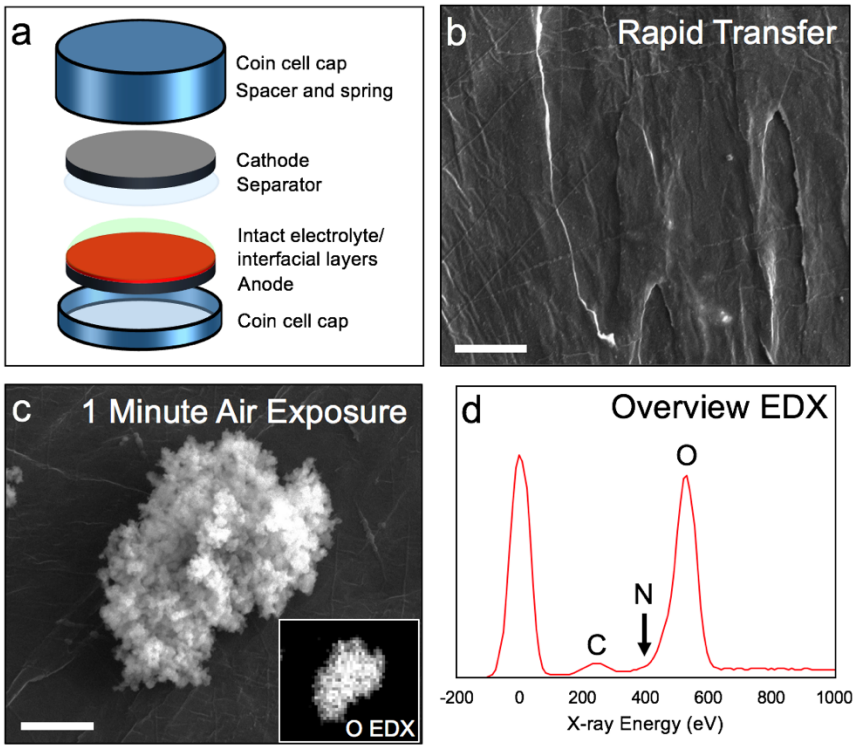

Figure 2.1 Contamination test of bare lithium metal during transfer of electrodes from a coin cell battery to a slush nitrogen pot where liquids are typically preserved on the electrode surface. (a) A schematic of a typical coin cell used for cryo-FIB experiments, where the lower electrode with an interfacial layer of interest and electrolyte to be preserved are removed and rapidly frozen in slush nitrogen. (b) In a test of the reactivity of bare lithium removed from a coin cell, rapid transfer to the slush nitrogen pot results in minimal surface reactions. (c) Intentional exposure to air for approximately one minute before plunging into slush nitrogen results in formation of oxide growths at grain boundaries on the electrode surface. (d) Despite the direct contact with liquid/solid nitrogen, no reaction with the lithium to form lithium nitride occurs during preparation. Scale bars are 3 μm.

highly reducing nature of lithium provides the potential for a reaction to form lithium nitride, a potential concern for plunge freezing into liquid or slush nitrogen. We found, however, that the cryogenic temperature of the nitrogen and the rapidly reduced sample temperature prevent these reactions from occurring, and nitrogen is not observed on the sample surface, for example as displayed in the spectrum in Fig. 2.1d. Therefore, rapid plunge freezing of electrodes into slush nitrogen not only preserves liquids and

interfacial structures present, but also enables transfer into the instrument with minimal contamination.

2.3.2 Enabling FIB Milling of Reactive Materials

With the sample maintained near liquid nitrogen temperature in the instrument, its chemical reactivity is dramatically reduced. This enables FIB milling of samples that are typically problematic at room temperature due to interactions with the gallium-ion beam. For example, lithium can form alloys with gallium [125,126], and this results in formation of extraneous material during milling at room temperature, rather than a simple sputtering of the target material. Regular cross sections milled in lithium at room temperature therefore generate a large amount of redeposited material that covers the final cross section surface (Fig. 2.2a). The same milling performed with the sample at cryogenic temperature, however, produces a clean surface with very little redeposited material (Fig. 2.2c). While cleaning cross sections milled at room temperature do result in a clean final cross section surface, they generate large structures in the trench (Fig. 2.2b) that are likely composed of a lithium-gallium alloy and can impede the view of the cross section surface. Milling at cryogenic temperature significantly increases the quality of the milled area, and the material redeposited in the trench appears similar to that of materials that don't interact with the gallium beam at room temperature. It is also worth noting that the samples shown in Fig. 2.2 were loaded into the FIB using the full cryogenic loading technique described above, and the sample was subsequently warmed to room temperature for the corresponding portion of the experiment. This enabled us to avoid the significant oxidation that the lithium surface undergoes during the extended

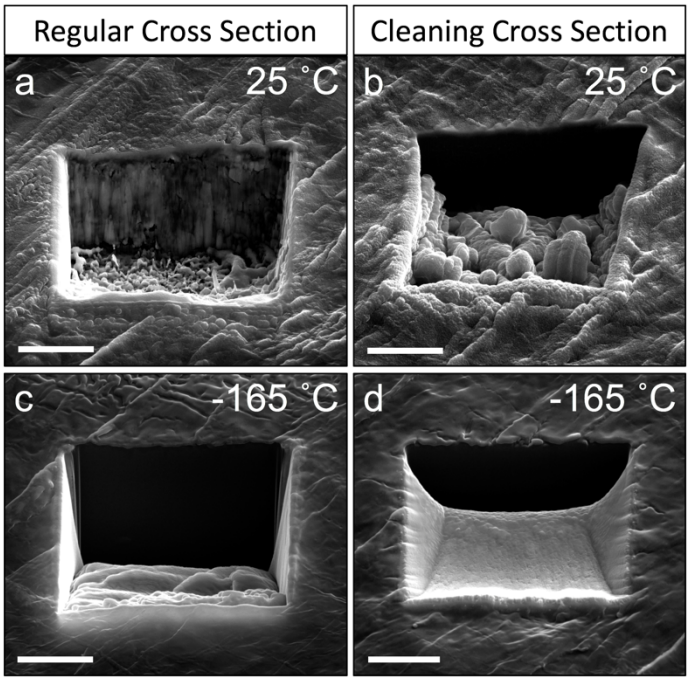

Figure 2.2 FIB milling of lithium metal with a room versus cryogenic sample temperature. (a) At room temperature a "regular cross section", which removes material quickly by making multiple milling passes over the sample, results in formation of extraneous material, likely an lithium-gallium alloy, which redeposits in the surrounding area and on the cross section surface. (b) Likewise, a "cleaning cross section", which makes a single slow milling pass over the sample to leave a clean cross section surface, results in formation of large structures in the trench, potentially blocking the view of the cross section surface. Milling (c) regular cross sections and (d) cleaning cross sections with a cryogenic sample temperature, however, enables clean trenches and final cross section surfaces to be produced in reactive materials such as lithium. Scale bars are 5 μm.

loading period required for room temperature FIB preparation.

2.3.3 The Native Structure and Composition of Deposited Lithium

By preventing surface reactions and increasing the quality of the cross sections through the use of cryogenic techniques, accurate characterization of reactive materials such as those used in batteries is enabled. An example of this is demonstrated in Fig. 2.3. Here, lithium was deposited in a coin cell battery onto a copper electrode coated with a thin

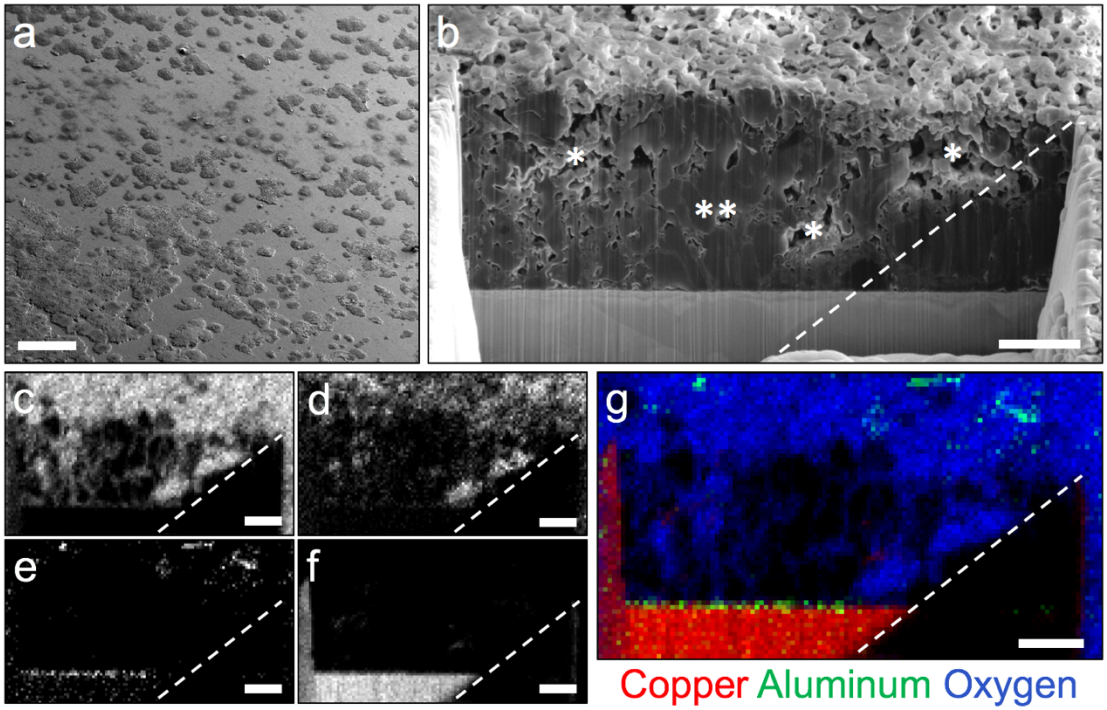

Figure 2.3 Accurate characterization of reactive material cross sections. (a) Lithium was deposited on a copper coin cell electrode with a thin alumina artificial SEI layer ~15 nm thick, resulting in localized lithium deposits. (b) Cross-sectional cryo-FIB milling allowed internal dense and porous regions to be identified in the lithium deposits (marked by ** and *, respectively). (c-g) EDX mapping of oxygen (c), carbon (d), aluminum (e), and copper (f), revealed no elements in the dense regions, indicating pure lithium deposition, but the porous regions contained elevated levels of carbon and oxygen, suggesting these regions contained lithium carbonates and oxides. These insights could not have been reliably provided by room temperature FIB/SEM due to sample reactions during transfer, milling, and characterization. The ~15 nm thick alumina layer is seen here as well. Also, note the shadowing in the EDX maps, due to the placement of the detector, indicated by the dashed lines. (a) scale bar is 300 µm, and (b-g) scale bars are 5 µm.

artificial SEI layer consisting of ~15 nm of alumina. Inhomogeneities in the alumina layer guided the deposition and resulted in formation of localized lithium deposits (Fig. 2.3a). The cryogenic sample temperature allowed us to mill cleanly through the deposits, revealing their native interior structure, as shown in Fig. 2.3b. Both dense and porous regions were found within the deposited lithium (marked by ** and *, respectively), with differing contrast in the secondary electron images. In addition to

imaging of cross sections produced by cryo-FIB, EDX mapping can be performed to track the distribution of elements in the cross section. This is shown in Figs. 2.3c to 2.3f for the carbon, oxygen, aluminum, and copper signals present in the cross section through the lithium deposit. First, the ~15 nm thick alumina layer can be seen in the aluminum map, indicating that layers at least this thin can be identified by EDX in the cryo-FIB. This layer is thin enough that the oxygen signal is likely much weaker than the signal coming from the lithium deposit, and therefore not visible adjacent to it. Additionally, while no elements were detected in the dense deposition regions, a significant concentration of oxygen and carbon was observed in the porous regions. Since low-energy Li *K*-edge X-rays are undetectable by most EDX spectrometers, the apparent lack of elements in the dense regions indicates these are areas of pure lithium deposition. In contrast, the material in the porous regions is likely composed of lithium oxide and/or carbonate, due to the combined oxygen and carbon signals in these regions. This suggests that porous or dendritic type lithium deposits may involve additional chemistry. Here, the advantages of cryo-FIB/SEM are clear, since sample transfer, milling, and even exposure to the electron beam at room temperature can each induce compositional changes in sample. Therefore, the inherent nature of these materials established by the cryogenic results could not be concluded by room temperature FIB/SEM.

2.3.4 Intact Solid-Liquid Interfaces and Interfacial Layers

In addition to enabling accurate characterization of clean cross sections produced in reactive materials, the rapid freezing process preserves liquids present on the sample.

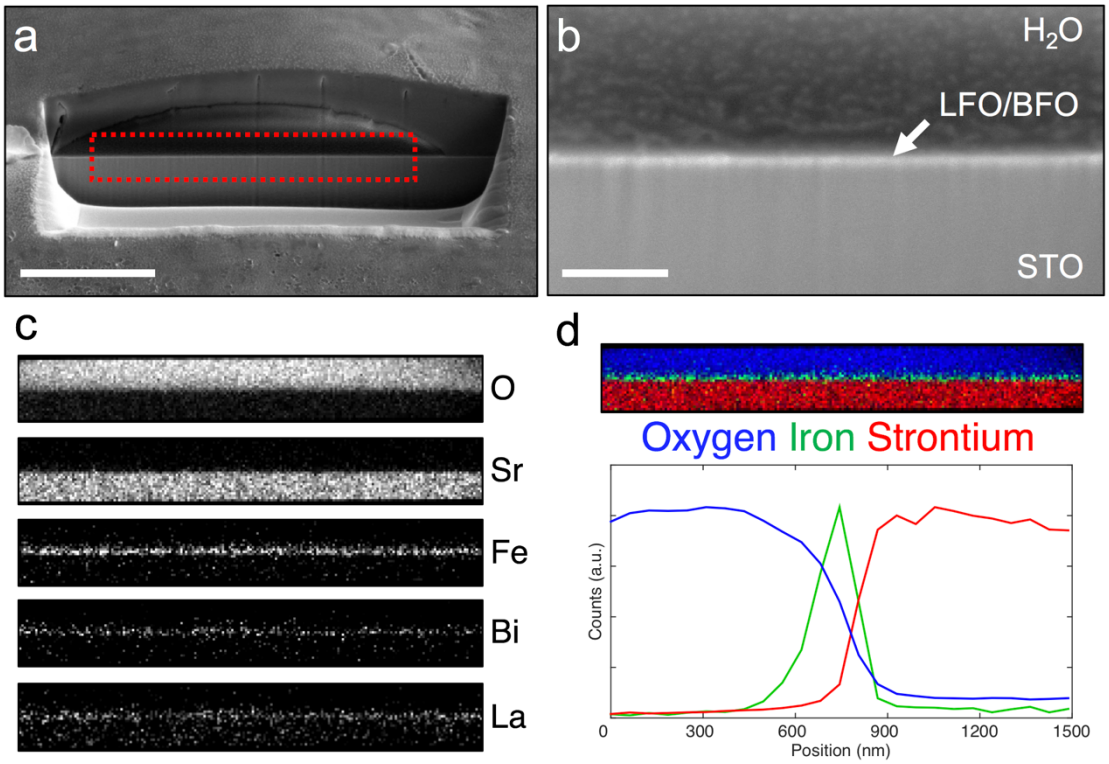

Figure 2.4 Nanoscale imaging and mapping of an intact solid-liquid interface cross section. (a) A droplet of aqueous solution was rapidly frozen on the surface of a strontium titanate (STO) substrate, with a ~50 nm thick interfacial layer of alternating lanthanum ferrite/bismuth ferrite (LFO/BFO) unit cells. An organometallic platinum layer was deposited on the surface of the sample before milling to enable a smooth cross section surface to be formed. (b) SEM imaging of the interface confirmed the ~50 thick interfacial later. (c) EDX mapping of the interface revealed oxygen present throughout the sample but strongest in the aqueous solution, and strontium only in the substrate. A strong Fe-*L* signal and weaker La-*M* and Bi-*M* signals were present at the interface. (d) An integrated line profile of the iron signal showed a strong peak centered at the interface, with a tilt-corrected FWHM of around 200 nm due to beam penetration and broadening combined with the sample tilt. This is apparent on the aqueous solution side of the interface, where a tail in the iron signal is present. (a) scale bar is 5 µm and (b) scale bar is 500 nm.

This allows cross sections to be produced through intact solid-liquid interfaces, enabling nanoscale imaging and spectroscopy of structures and layers at these interfaces in their near-native environment. Fig. 2.4 demonstrates these capabilities, displaying a cross section milled through a droplet of aqueous solution in contact with an oxide substrate, similar in structure to a liquid-gated field-effect transistor [127,128]. Between the

strontium titanate (STO) substrate and the aqueous solution is a ~50 nm thick interfacial layer consisting of alternating lanthanum ferrite (LFO) and bismuth ferrite (BFO) unit cells produced by molecular beam epitaxy. To form the small aqueous droplets on the surface, an atomizer was used to deposit the liquid. For this sample, approximately 2 μm of organometallic platinum was deposited on the sample surface prior to milling to protect the soft aqueous material and enable a smooth final cross section surface. Imaging of the interface revealed that the LFO/BFO interfacial layer was easily resolved, as displayed in Fig. 2.4b. The tilt-corrected full-width at half-maximum (FWHM) of the secondary electron signal from this layer was within 20% of the actual width of the layer. Additionally, spectroscopic mapping of the interface was performed, and the resulting oxygen, strontium, iron, bismuth, and lanthanum maps are shown in Fig. 2.4c. While oxygen is present in all of the layers across the interface, the signal is strongest in the aqueous solution, and the strontium is present only in the substrate. The iron, bismuth, and lanthanum signals, however, are localized to the interfacial LFO/BFO layer, demonstrating that interfacial layers 50 nm thick or less can be mapped at intact solid-liquid interfaces by cryo-FIB EDX. A composite map of the oxygen, iron, and strontium signals is also shown in Fig. 2.4d, along with a line profile of these elements across the interface. While the LFO/BFO layer is ~50 nm thick, the iron line profile displays a value larger than this, with a tilt-corrected FWHM of ~200 nm, which will be discussed further in the following section.

2.4 Discussion

2.4.1 Factors that Influence Resolution

One primary factor that limits characterization of solid-liquid interfaces is the total electron dose that can be applied to the sample. Soft materials such as frozen liquids are typically much more beam-sensitive than hard materials, and this limits the total dose that can be applied, and consequently the signal-to-noise ratio (SNR) and resolution attainable [129]. As an example, the alumina layer present at the interface between the electrode and the lithium deposit in Fig. 2.3 was only ~15 nm thick, yet easily resolved, while resolving the 50 nm LFO/BFO layer at the solid-liquid interface shown in Fig. 2.4 required much more optimization. This was due to the fact that the aqueous layer limited the total dose that could be applied, resulting in either a low SNR or damaged materials for conditions that were less than optimal. Assuming the probe is well-focused (smaller than the spacing between pixels), one method that usually allows a higher dose to be applied during acquisition of an EDX map is to increase the number of probe positions through acquisition of a high-resolution map to more evenly spread the dose over the sample, even if this results in lower SNR data. The resulting map can then be binned to a lower resolution to increase SNR.

As stated previously, the apparent width of the LFO/BFO layer at the solid-liquid interface shown in Fig. 2.4 is larger than the actual thickness of the layer. Many factors influence the localization achievable at interfaces such as these. One of these is the penetration depth of the electrons that generate the X-ray signal combined with the geometry of the sample within the instrument. While the interfacial layer of interest for this work lies parallel to the sample surface, the sample can be tilted to a maximum of

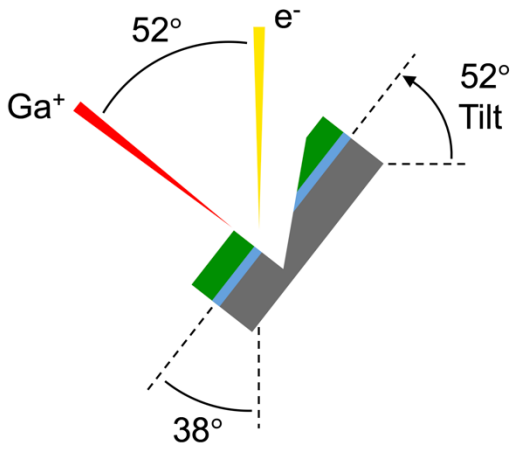

Figure 2.5 Geometry of a sample containing an interfacial layer parallel to the sample surface in the cryo-FIB.

approximately sixty degrees (for an example of the geometry of this type of sample in the cryo-FIB, see Figure 2.5). The surface of the sample is initially perpendicular to the electron beam, and therefore the minimum angle between the layer of interest and the electron beam is around thirty degrees. More fundamentally, interface layers that aren't near the edge of a sample cannot be viewed exactly parallel to the beam unless the sample has a significant curvature to its surface. This is apparent, for example, if the sample in Figure 2.5 is tilted further to ninety degrees. While this is not an issue when using surface sensitive techniques, such as secondary electron imaging, it introduces additional challenges when using techniques that probe below the sample surface as well, such as EDX mapping. The characteristic X-rays generated to produce the EDX maps can often be excited at depths nearing the primary beam electrons' range in the sample. This range can be approximated by [6]:

$$R_X = \frac{0.064}{\rho}(E_0^{1.68} - E_c^{1.68}) \tag{2.1}$$

where R_X is the depth characteristic X-rays can be generated from in microns, ρ is the

density of the material the electron beam travels through in g/cm^3, and E_0 and E_c are the beam and characteristic X-ray energies, respectively, in keV. For low-density materials such as aqueous solutions, the X-ray generation depth can be many microns deep for high beam voltages. For the low beam voltage of 5 kV used for Fig. 2.4, however, the iron *L*-edge can be excited approximately 900 nm into the material. At a typical sample tilt of fifty-two degrees, this would result in an apparent broadening of the EDX signal generated by a two-dimensional iron layer to maximum width of nearly 500 nm. In reality, the broadening is not this severe, as is apparent in Fig. 2.4, due in part to the fact that X-rays generated deep within the sample are attenuated before reaching the detector. Correspondingly, a tail in the iron signal can be observed on the aqueous solution side of the interface. This tilt-induced broadening is inherent to the system, unless a combination of instrument/sample geometry and milling location allows this to be overcome. For example, a pre-tilted sample may allow an interfacial layer near the edge of a sample to be characterized parallel to the electron beam. Even in this case a broadening would occur, however, since the electron beam generates X-rays in a volume of similar width and depth [6], resulting in the iron signal still being detected in the neighboring regions. Less broadening should occur for denser materials, however, according to Eq. 2.1. For example, if this hypothetical two-dimensional iron layer were placed between two STO layers the maximum broadening discussed above would be reduced to less than 100 nm. Interfacial layers between denser materials, for example in perovskite oxide superlattices, should therefore be able to be localized with more precision.

One way to reduce the apparent broadening of an interfacial layer would be to lower

the beam voltage, thereby decreasing the beam penetration depth and the size of the corresponding excitation volume. There are significant drawbacks to this approach, however, which means its usefulness is often limited. First, the beam voltage provides an energy cutoff above which characteristic X-rays cannot be generated. To a first approximation then, lowering the beam voltage still has the potential to decrease the apparent broadening of elements with low-energy excitation edges. Two factors complicate this, however. The energy resolution of EDX detectors is generally >100 eV [6], and this can result in overlapping peaks in samples containing many elements with low-energy edges. Additionally, peaks in all but the lowest-energy region may be difficult to detect due to a decreased beam overvoltage and fluorescence yield. For a given characteristic X-ray peak energy, the cross section for an inner shell ionization is [6]:

$$Q \propto \frac{1}{U} \ln (c_S U) \tag{2.2}$$

where U is the overvoltage, defined as the E_0/E_c, the electron beam and characteristic X-ray energies again, respectively, and c_S is a constant that depends on the shell being excited. Below $U = 1$ no excitation occurs, but between $U = 1$ and $U \approx 3$ there is a rapid increase in the cross section. Above $U \approx 3$ the cross section begins to slowly decline again. Therefore, very low beam voltages of 1-2 kV only strongly excite peaks at hundreds of eV or less, whereas a 5 kV beam, for example, strongly excites the sample up to nearly 2 keV. An example of these effects is shown in a cross section mapped with a 2 kV electron beam in Fig. 2.6. At this voltage the bismuth edge at >2 keV is not present anymore, and the strontium edge at 1.8 keV is only very weakly excited,

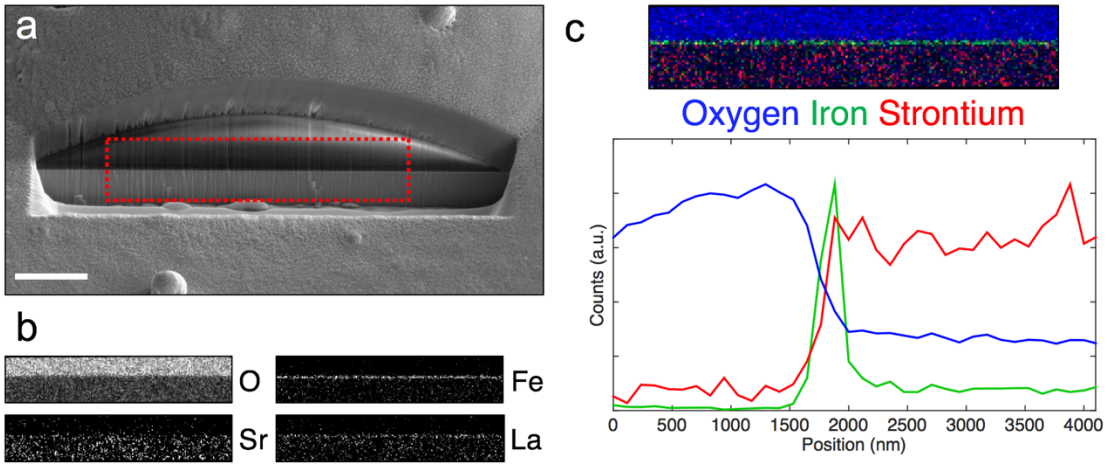

Figure 2.6 Nanoscale imaging and mapping of an intact solid-liquid interface cross section with a 2 kV beam. (a) As in Fig. 2.4, a droplet of aqueous solution was rapidly frozen on the surface of a strontium titanate substrate, with a ~50 nm thick interfacial layer of alternating lanthanum ferrite/bismuth ferrite unit cells. An organometallic platinum layer was deposited on the surface of the sample before milling to enable a smooth cross section surface to be formed. (b) EDX mapping of the interface revealed oxygen present throughout the sample but strongest in the aqueous solution, and strontium only in the substrate. The strontium signal, above 1.8 keV, was significantly weaker than with the 5 kV beam, displayed in Fig. 2.4, and therefore produced a dramatically lower SNR map. An Fe-*L* signal was still strongly excited, while the La-*M* was significantly weaker and the Bi-*M* (> 2 keV) was not present. (d) An integrated line profile of the iron signal still showed a strong peak centered at the interface, with a tilt-corrected FWHM only ~50% larger than the 5 kV case. Scale bar is 5 µm.

resulting in a low SNR. While light elements such as carbon or oxygen may have *K*-edges present at hundreds of eV or less, heavier elements may also have *L*-, *M*-, or *N*-edges in this range. These higher order edges may not generate X-rays as strongly, however. The fluorescence yield, or fraction of excitations that result in characteristic X-ray production, depends on both the element and the shell being excited [6]. While the fluorescence yield for a given shell increases with atomic number, it is significantly reduced for higher order shell excitations. Evidence of this can be seen in the EDX maps of Fig. 2.4, where the iron *L*-edge is more strongly detected than the *M*-edges of lanthanum and bismuth.

Another method for potentially reducing the broadening that occurs would be to mill a lamella-type structure in the material, rather than a simple cross section, by removing material on both sides of the site of interest, leaving a vertical cross-sectional slice. In theory, this method has many advantages. First, the physical thickness of the lamella could be reduced so that the interfacial layer would transition from a two-dimensional plane to a one-dimensional line in the limit of a very thin lamella. This would reduce the apparent width of the tilted interfacial layer. The second advantage would come from the ability to use higher beam voltages. In a normal cross section, high beam voltages cause deep penetration and large beam broadening in the sample, significantly reducing the localization of features at the interface. A high-voltage beam would pass through the lamella with little broadening before exiting the back side, however, enhancing the localization ability. On the other hand, this beam penetration would result in the electrons impacting the substrate behind the lamella, and elements from the substrate would be detected across the interface. If the cryo-FIB is equipped properly for a cryogenic lift-out procedure (see Chapters 3 and 4) [123,130], the lamella could be extracted from the surrounding material before mapping to remove this effect. The use of higher beam voltages would also allow additional characteristic X-ray edges to be utilized at higher energies.

In practice, we have found that there are trade-offs to the lamella structure which limit the results, so we find that this type of structure may only be beneficial in certain cases. One reason for this is that as samples become thin, the ionization cross section discussed above becomes linearly proportional to thickness [6]. The result is that the SNR achievable before the onset of damage is much lower, since the damage per volume

remains constant, while the signal generated per volume decreases with decreasing sample thickness [86]. Therefore, in samples that are not dose-limited this may be a viable method for improving resolution. In addition, while high beam voltages provide access to an increased number of characteristic peaks, the peaks low energies may be more difficult to detect with high beam voltages. As mentioned above, the ionization cross section decreases above an overvoltage of about three, so significantly increasing the beam voltage can suppress excitation of low energy edges. For example, increasing the beam voltage from 5 kV to 30 kV reduces excitation of the silicon *K*-edge at ~1.7 keV by a factor of ~2.5 [6]. In addition to this suppression of low-energy peaks, the SNR of the peaks is further decreased by the increased Bremsstrahlung background due to deceleration of the high-energy electrons. For example, the background at 2 keV due to Bremsstrahlung radiation is approximately an order of magnitude higher for a 30 kV beam than for a 5 kV beam [6]. These effects all combine to reduce the ability to use low-energy peaks at high beam voltages. Therefore, pairing a lamella-type cross section with a high beam voltage may be effective if accessing particular high-energy peaks is necessary, but otherwise the decreased SNR for dose-sensitive samples and the detrimental effects incurred on detection of low-energy peaks may offset any gains in resolution.

Finally, in order for the apparent width of the remaining interface layer to be significantly reduced compared to the results achievable with a cross section, the lamella must be made very thin. For the tilt-corrected width to match the ~200 nm value achieved with the cross section shown in Fig. 2.4, the lamella must approach 200 nm thick. This can be challenging to accomplish, depending on the material [123]. An

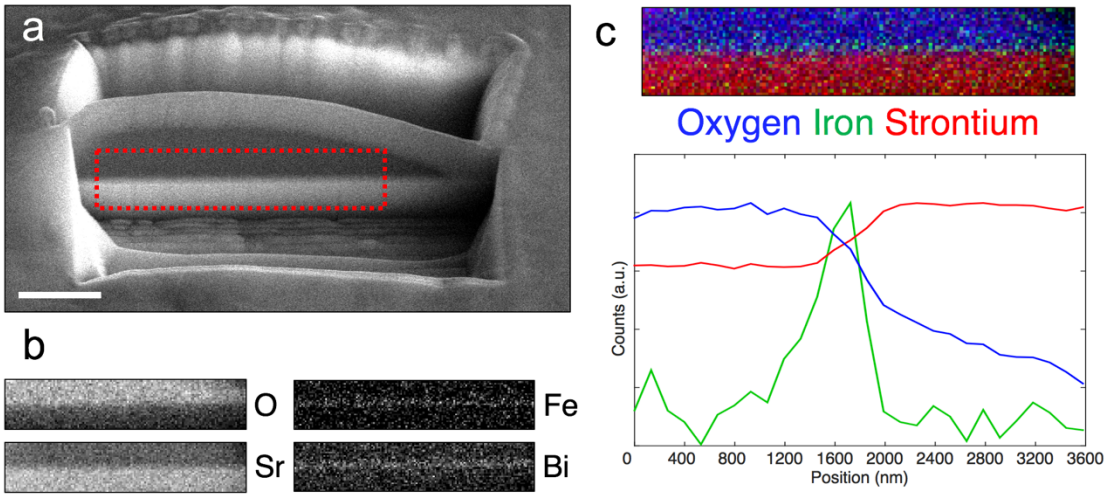

Figure 2.7 Nanoscale imaging and mapping of an intact solid-liquid interface in a cross-sectional lamella structure averaging ~850 nm thick using a 30 kV beam. (a) As in Fig. 2.4, a droplet of aqueous solution was rapidly frozen on the surface of a strontium titanate substrate, with a ~50 nm thick interfacial layer of alternating lanthanum ferrite/bismuth ferrite unit cells. An organometallic platinum layer was deposited on the surface of the sample before milling to enable a smooth cross section surface to be formed. In this case, material was removed on either side of the site of interest, resulting in the formation of a vertical lamella. (b) EDX mapping of the interface revealed oxygen present throughout the sample but strongest in the aqueous solution. Strontium was no longer present only in the substrate, due to the penetration of the beam through the lamella. The signals from the interfacial elements were significantly weaker than the 5 kV cross section case, due to the electrons penetrating through the lamella, even at this thickness. (d) An integrated line profile of the iron signal still showed a strong peak centered at the interface, and while the tilt-corrected FWHM was on the order expected assuming little beam broadening, it was much broader and noisier than the 5 kV beam cross section case. Scale bar is 5 µm.

example of the effects of a lamella larger than this is shown in Fig. 2.7, where a 30 kV beam was used to map a lamella with an average thickness of ~850 nm. The FWHM of the iron signal is on the order of 500 nm, indicating that little beam broadening occurred, but this value is much larger than the cross section result, and the SNR is already noticeably reduced even at this large thickness. Fig. 2.8 additionally shows results from a thinner lamella, <250 nm thick. The integrated line profile of the iron signal still shows peak at the interface, and has a FWHM approximately equal to that of Fig. 2.4, but as

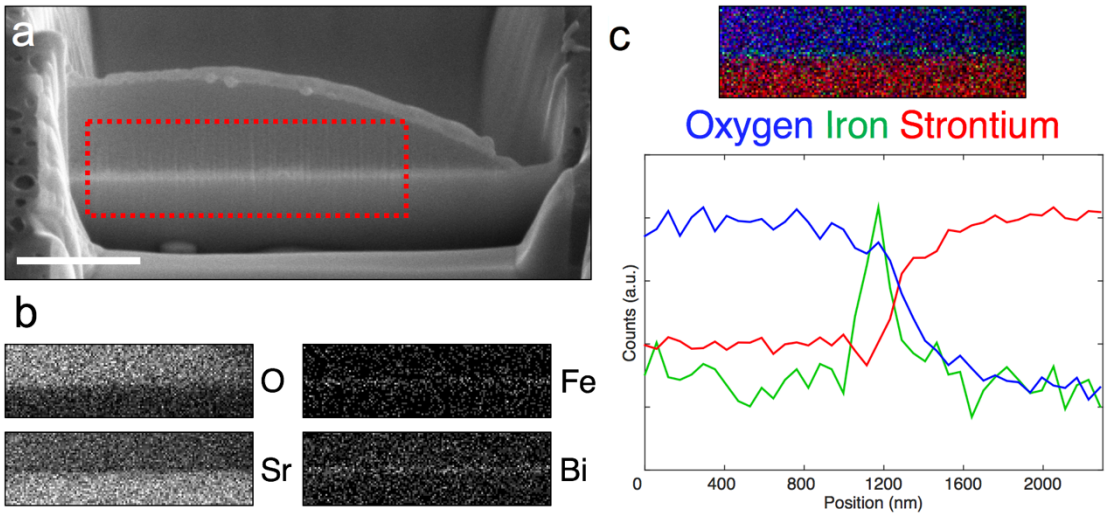

Figure 2.8 Nanoscale imaging and mapping of an intact solid-liquid interface in a <250 nm thick cross-sectional lamella structure with a 10 kV beam. (a) As in Fig. 2.4, a droplet of aqueous solution was rapidly frozen on the surface of a strontium titanate substrate, with a ~50 nm thick interfacial layer of alternating lanthanum ferrite/bismuth ferrite unit cells. An organometallic platinum layer was deposited on the surface of the sample before milling to enable a smooth cross section surface to be formed. In this case, material was removed on either side of the site of interested, resulting in the formation of a vertical lamella. (b) EDX mapping of the interface revealed oxygen present throughout the sample but strongest in the aqueous solution. As in Fig. 2.7, strontium was present across the interface due to the penetration of the beam through the lamella. The signals from the interfacial elements were weaker still compared to Fig. 2.7 due to the sample thinness. (d) An integrated line profile of the iron signal still showed a peak centered at the interface. The tilt-corrected FWHM was similar to the 5 kV beam cross section case shown in Fig. 2.4, but the profiles were dramatically noisier. Scale bar is 3 µm.

expected, the SNR is dramatically reduced. In this case the interfacial layer can still be identified, but less extended features such as nanoparticles may not have been.

Given the above considerations, we found that a beam voltage of 5 kV combined with a single-sided cross section produced the best results for our aqueous solution-oxide interface sample shown in Fig. 2.4. Reducing the beam voltage significantly decreased the signal from many of the edges and eliminated some of the edges in the upper range detected at 5 kV. Producing a lamella structure decreased the signal from

all of the edges present, particularly those at low energies, though edges at higher energies were then available. Since this sample was dose-limited, the decrease in signal per beam electron arising from each of these methods resulted in a much lower SNR, and the quality of the final maps was lower.

2.4.2 Examples for Applications in Batteries

While we have demonstrated the capabilities of cryo-FIB/SEM by performing nanoscale imaging and spectroscopic mapping of cross sections produced in a few example systems, these techniques will be beneficial for studying a wide range of phenomena in energy devices. Electrochemical energy storage, for example, often involves both chemically reactive materials and solid-liquid interfaces [5], and characterization of these materials and interfaces is therefore difficult to achieve in an unaltered state. The ability to directly image and map these materials and interfaces in a near-native state at the nanoscale will be very useful for studying processes at these interfaces. One area where this will be beneficial is in engineering of artificial SEI layers, which has been shown to be a promising method for improving the cyclability and safety of high-energy density rechargeable metal-anode batteries [131–134]. Cryogenic techniques allow the native thickness, morphology, and composition of artificial SEI layers to be tracked. Typically, engineering of these layers relies on *ex situ* experiments to monitor these characteristics, which could provide misleading results. As a result, cryo-FIB/SEM will enhance the design and implementation of artificial SEIs, advancing metal-anode battery technology. An additional area where cryo-FIB could prove useful for electrochemical energy storage is in tracking dissolution of

elements from electrodes, an issue that limits various promising materials. For example, manganese oxide spinels are cathode materials that have generated interest due to their low cost, low environmental impact, high rate capability, and potential for operating at high voltages, but their longevity is limited by dissolution of Mn^{2+} ions out of the cathode and into the electrolyte [90,135,136]. Cryo-FIB techniques may allow this dissolution process to be directly tracked with the electrolyte present, providing useful information to help circumvent this issue and enable use of these materials. Finally, cryogenic temperatures have also been shown to stabilize volatile solids in the instrument vacuum [137]. Therefore, cryo-FIB/SEM will enable accurate characterization of sulfur-containing materials, for example, which is not possible using standard high-vacuum techniques at room-temperature. Sulfur-based cathodes are considered some of the most promising for viable lithium metal batteries, but currently have performance that is limited by issues including dissolution of polysulfides into the electrolyte and shuttling of these materials between the electrodes [20]. Cryo-FIB techniques could therefore significantly aid the development of lithium-sulfur batteries by enabling accurate characterization of sulfur-based cathode structures designed to address these issues, and aid in evaluation of the effectiveness of these structures by tracking the corresponding polysulfide dissolution and shuttling in the electrolyte.

2.4.3 Developments to Broaden and Enhance Cryo-FIB/SEM Capabilities

While cryo-FIB/SEM allows a wide variety of experiments to be performed which were not possible before, additional developments will continue to expand its capabilities in the future. Recently, for example, Xe^{+} plasma FIBs (PFIBs), which allow significantly

larger quantities of material to be removed in a given time than traditional gallium-based FIBs, have been combined with SEM beams to form PFIB/SEM systems [138]. Development of cryo-PFIB/SEM would broaden the capabilities of cryo-FIB techniques. For example, the increased milling rate could enable material to be removed from the edge of the sample all the way to the site of interest, providing a means to characterize interfaces away from the edge of the sample parallel to the electron beam. Cryo-PFIBs would also allow larger devices, or structures further buried within devices, to be characterized. For example, a cryo-PFIB may be able to mill entirely though small batteries. This would allow structures and elements to be tracked across the entire distance between the electrodes, rather than just the region near a single electrode.

An additional benefit of the cryogenic sample temperature could be enabling EDX of lithium over extended time periods. Due to its low energy, the lithium *K*-edge is typically not detectable by EDX. Recently though, EDX detectors capable of measuring the *K*-edge of lithium in high concentrations, such as in lithium metal, have been developed by decreasing the electronic noise and improving the charge collection efficiency of the detectors, as well as removing the vacuum window between the detector and FIB/SEM chamber, which absorbs low-energy X-rays [139]. Similar to oxidation of lithium in the TEM [60], exposing lithium metal to the electron beam in the SEM at room temperature will oxidize the surface of the sample, reducing the lithium signal over time. As a consequence, the lithium signal decreases over time for extended acquisitions, such as during elemental mapping. Pairing these new detectors with cryo-FIB/SEM, however, would minimize this effect and allow lithium to be mapped with increased signal over an extended period of time.

Finally, combining these cryo-FIB/SEM techniques with a cryogenic sample lift-out system enables preparation of cryo-STEM samples as well [123]. This provides a pathway to combining the morphological and elemental information provided by cryo-FIB/SEM with higher resolution structural and bonding information provided by aberration corrected cryo-STEM techniques. This could allow, for example, dissolution of cathode materials to be tracked at very high resolution near the electrode surface.

2.5 Conclusions

While many devices important for current and future energy generation and storage rely on reactive materials and solid-liquid interfaces, characterization of these types of materials at high resolution in an unaltered state is often not possible. Cryo-FIB/SEM techniques combine the nanoscale imaging and spectroscopic capabilities of SEM and the milling capability of FIB with cryogenic sample temperatures, enabling unaltered reactive materials and intact solid-liquid interfaces from devices to be characterized at the nanoscale. These techniques will benefit a wide range of fields, allowing, for example, enhanced design and implementation of artificial SEI layers, tracking of material dissolution from electrodes, and accurate characterization of volatile solids such as sulfur. Cryo-FIB will therefore be an important tool for engineering devices that utilize reactive materials and/or solid-liquid interfaces, and further developments will continue to enhance its capabilities in the future.

CHAPTER 3

SITE-SPECIFIC PREPARATION OF INTACT SOLID-LIQUID INTERFACES BY LABEL FREE *IN SITU* LOCALIZATION AND CRYO-FIB LIFT-OUT

Scanning transmission electron microscopy (STEM) allows atomic scale characterization of solid-solid interfaces, but has seen limited applications to solid-liquid interfaces due to the volatility of liquids in the microscope vacuum. While cryo-electron microscopy is routinely used to characterize hydrated samples stabilized by rapid freezing, sample thinning is required to access the internal interfaces of thicker specimens. Here, we adapt cryo-FIB "lift-out", a technique recently developed for biological specimens, to prepare intact internal solid-liquid interfaces for high-resolution structural and chemical analysis by cryo-STEM. To guide the milling process we introduce a label-free *in situ* method of localizing subsurface structures in suitable materials by energy dispersive X-ray spectroscopy (EDX). Monte Carlo simulations are performed to evaluate the depth-probing capability of the technique, and show good qualitative agreement with experiment. We also detail procedures to produce homogeneously thin lamellas, which enable nanoscale structural, elemental, and chemical analysis of intact solid-liquid interfaces by analytical cryo-STEM. This work demonstrates the potential of cryo-FIB lift-out and cryo-STEM for understanding physical and chemical processes at solid-liquid interfaces.

(Originally published: Zachman, M. J., Asenath-Smith, E., Estroff, L. A. & Kourkoutis, L. F. Site-Specific Preparation of Intact Solid–Liquid Interfaces by Label-Free In Situ Localization and Cryo-Focused Ion Beam Lift-Out. *Microsc. Microanal.* **22** (06), 1338–1349 (2016). Reproduced with permission.)

3.1 Introduction

Solid-liquid interfaces play a pivotal role in many fields, such as crystal growth in solution and hydrogels, which can guide crystals to unique morphologies and properties [140,141]; biomineralization, where biological organisms form composite materials through organic-inorganic interfaces [142]; and energy materials research, where electrode-electrolyte interfaces play a key role in the operation, performance, and safety of batteries [5,25]. Transmission electron microscopy (TEM) and scanning transmission electron microscopy (STEM) provide atomic-resolution structural, elemental, and bonding information about solid-solid interfaces in hard materials [47,74,143], but have thus far been limited in their applications to solid-liquid interfaces. This is due to the fact that in conventional electron microscopy these samples must be dried before entering the high vacuum of the microscope column, which can alter structure and chemistry of solid-liquid interfaces.

Cryo-TEM is a well-established technique in the biological sciences designed to address this issue and allows the near-native structure of thin frozen-hydrated specimens to be investigated at the nanoscale [144–148]. Samples are cryo-immobilized by rapid freezing, which vitrifies the solution and avoids the formation of ice crystals that can damage the biological structure [10,149]. However, specimens that cannot be snap-frozen directly to an electron transparent thickness, such as whole cells, must be thinned prior to analysis in the cryo-TEM. Traditionally, cryo-ultramicrotomy served this function by using a diamond blade to slice thin sections from a larger sample [150]. However, cryo-ultramicrotomy lacks site-specificity, and the physical cutting process induces unavoidable image artifacts [151]. As a result, cryo-focused ion beam (cryo-

FIB) was developed in recent years as an alternative thinning method that addresses these issues.

Traditional FIB lift-out at room temperature is routinely used for site-specific preparation of high quality TEM samples from bulk materials and devices [7]. In this method, a focused beam of ions (typically Ga^+) is used to site-specifically remove material around a site of interest, forming a cross-sectional slice, or lamella, which is extracted from the bulk sample and transferred to a TEM grid using a nanomanipulator. Subsequently, the lamella is thinned to electron transparency for TEM work. The first attempt to modify this technique for preparation of frozen-hydrated biological samples was made by installing a liquid nitrogen cooled stage in a FIB, which enabled thinning of whole frozen cells and subsequent imaging of sub-cellular structures by cryo-TEM [152–154]. In contrast to the traditional FIB lift-out preparation, these cryo-TEM samples were prepared directly on the TEM grid by milling entirely through the frozen specimen at a shallow angle, leaving a thin lamella nearly parallel to the supporting grid. While variations of this "on-grid" cryo-FIB technique have been successfully applied to a range of cells [111,154–158], it is limited to samples on the order of microns thick. Thicker samples may be too thick too mill entirely through or require longer milling times with increased beam currents, which can induce sample damage. For preparation of bulk soft materials or large samples with internal solid-liquid interfaces, such as hydrogels with embedded crystals or electrochemical energy storage devices, a technique similar to the traditional FIB lift-out method was needed, with the added challenge of maintaining the sample temperature below the devitrification point during the entire process. In recent years, developments of cooled nanomanipulators in

combination with existing cryo-stages have enabled proof of concept demonstrations of cryo-FIB lift-out of cryo-immobilized soft materials, such as frozen-hydrated *Caenorhabditis elegans* worms or hydrogels with embedded collagen fibrils [112,114,130,159]. In addition, cryo-FIB lift-out was recently also adapted for preparation of samples with buried solid-liquid interfaces for cryo-STEM analysis [160].

Cryo-FIB lift-out is inherently site-specific, as the user defines the area in which the TEM lamella is prepared. As a result, methods are needed to localize subsurface structures of interest prior to milling, and to guide the sample preparation process. For biological specimens this issue has been addressed recently using a correlative approach, where fluorescent labeling of molecules and cryo-fluorescence light microscopy (cryo-FLM) can be used to localize structures of interest prior to cryo-TEM or cryo-FIB preparation [130,156,161,162]. The sample must then be transferred to the FIB and properly aligned by correlating *in situ* cryo-FIB images with the *ex situ* cryo-FLM images to identify the region of interest. In addition to the inherent limited resolution of the light microscope used, which is worsened by thick or cryogenic specimens [130,161,163], this correlation process itself introduces additional uncertainty to the expected positions of the structures [161,164]. The result is an uncertainty in the final co-localized position of a structure typically on the order of a micron [161,165,166], though with added fiducial markers and a more involved correlation process this can now be reduced by an order of magnitude [158,164,167,168]. Additionally, the added handling and transfer steps introduced by such a two-instrument method increase the likelihood of compromising the sample

integrity through contamination or structural damage, especially at cryogenic temperatures. While these techniques can be used to localize labeled biological specimens with sufficient accuracy for cryo-FIB lift-out, alternative techniques are needed to localize subsurface structures that lack fluorescent labels.

Here, we present an *in situ* localization technique to identify elementally distinct subsurface structures directly in the cryo-FIB. We use energy dispersive X-ray spectroscopy (EDX) mapping to identify structures embedded microns below the surface of a cryo-immobilized material. Using these maps as guides, site-specific cryo-FIB lift-outs of targeted structures can be performed. We demonstrate this capability on silica hydrogel samples with iron oxide particles grown in their interior [169,170]. EDX mapping is used at various stages in the lift-out process to identify regions of interest, localize subsurface particles, and monitor site-specific milling.

A lamella containing the structure of interest can then be lifted out and subsequently thinned uniformly to electron transparency. The high quality of the resulting lamellas enabled the structure of inorganic particles embedded in hydrogel to be examined at the nanoscale by cryo-STEM. Elemental distributions across the interfaces, as well as the local bonding environments of the hydrogel and particles, were obtained using EDX and electron energy loss spectroscopy (EELS) in the cryo-STEM. These results demonstrate for the first time that cryo-FIB lift-out, in combination with cryo-STEM, can provide access to the structure and chemistry of intact solid-liquid interfaces at the nanometer scale.

3.2 Materials and Methods

3.2.1 Sample Synthesis and Freezing

A detailed description of the procedures used to synthesize the silica hydrogel and embedded iron crystals was described previously [169,170]. In brief, the silica hydrogel was produced by acidifying sodium metasilicate nonahydrate (0.5 M) with an equal volume of hydrochloric acid (1.0 M), and allowed to reach full gelation by setting for 24 h at 30 °C. Subsequently, iron chloride hexahydrate solution (180 mM or 900 mM) was added to the surface of the silica hydrogel. The iron chloride solution was allowed to diffuse throughout the interior of the hydrogel by setting for 24 h at 30 °C. To initiate the crystallization of iron (oxy-, hydr-) oxide nanocrystals within the hydrogels, the vessels were sealed and heated to 100 °C. The particular crystallization protocol employed in this work provides a well-documented pathway to the formation of iron oxide (α-Fe_2O_3, hematite) after 4 weeks of reaction, which proceeds through iron oxyhydroxide(s) (e.g., β-FeO(OH)) precursors that can be isolated after shorter reaction times, e.g., 4 h [170,171]. After cooling for 4 h at ambient conditions, specimens (~1 cm^3) were carefully extracted from the hydrogels, taking care to retain the structural integrity of the hydrogel. The specimens were rinsed by soaking in de-ionized water for 2 h; with water exchanges (6x) to remove all soluble salts. The specimens were stored under refrigeration in sealed vials until use.

To preserve the structures in their liquid environment, small pieces of the hydrogels (as seen in Figure 3.6a) were removed with a razor blade and stabilized by rapid plunge freezing into slush nitrogen. Typically, plunge freezing of aqueous solutions can vitrify samples up to microns thick, while high-pressure freezing can vitrify samples up to

hundreds of microns thick, but is slightly more involved to perform [102]. Formation of small ice crystallites in the hydrogel was not deemed prohibitive for the purposes of this study, so the simpler plunge freezing method was used.

3.2.2 Instrumentation

To maintain the sample at a temperature below the devitrification point throughout the lift-out procedure a Quorum PP3010T Cryo-FIB/SEM Preparation System (Quorum Technologies Ltd, East Gristead, West Sussex, UK) was installed on an FEI Strata 400 FIB (FEI Company, Hillsboro, OR, USA). The system provides a cooled stage and anticontaminator in the interior of the FIB, as well as a separate cooled stage and anticontaminator in a preparation chamber attached to the FIB. The preparation chamber enables platinum sputter coating, controlled sublimation, and fracturing of frozen samples in a high vacuum before transfer into the FIB. To cool the system, gaseous nitrogen is flowed through a heat exchanger in a large liquid nitrogen dewar and subsequently through vacuum isolated Teflon lines to the FIB and preparation chamber. Figure 3.1a shows the cryo-FIB stage, thermally isolated from the rest of the FIB by a ceramic plate, and the Teflon cooling lines. During operation the stages are maintained well below the devitrification temperature of the sample, typically -165 °C. The anticontaminators are operated at lower temperatures, typically -192 °C, to reduce ice contamination on the sample. To maintain the sample's vitreous state during lift-out, an OmniProbe 200 Nanomanipulator (Oxford Instruments, Abingdon, Oxfordshire, UK) was fitted with a cooled needle assembly, as shown in Figure 3.1b. A ceramic rod thermally isolates the assembly from the uncooled shaft, and a copper braid attached to

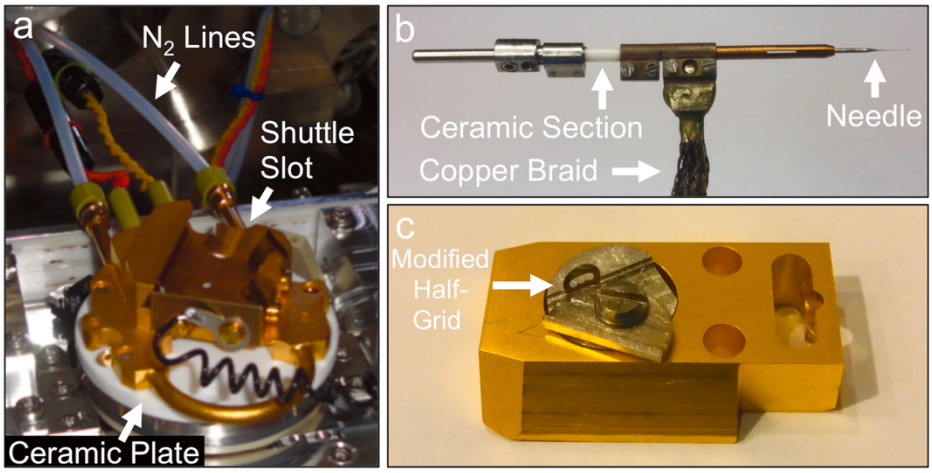

Figure 3.1 Components essential for the cryo-FIB lift out process: (a) A stage cooled to near liquid nitrogen temperature by flowing dry nitrogen through a heat exchanger in a large dewar and subsequently through vacuum isolated Teflon lines to the stage, which is thermally isolated by a ceramic plate. (b) A cooled nanomanipulator needle, thermally isolated from the shaft by a ceramic section, and cooled below the devitrification temperature of the sample through a copper braid attached to the anticontaminator. (c) A shuttle that transports bulk samples and TEM half-grids into and out of the cryo-FIB. Here, a stub modified at Cornell to hold a half-grid replaces the normal sample stub. A custom grid, a half-grid glued to a molybdenum slotted grid to improve handling and loading characteristics, is held in the stub.

the anticontaminator in the FIB provides cooling. Temperature measurements using a Type T thermocouple soldered to the lift-out needle confirmed the minimum temperature is well below the devitrification temperature of water, as shown in Figure 3.2. The cooling rate of the needle nearly parallels the other system components, which confirms good thermal transport through the braid and connections.

Frozen samples are transferred into and out of the FIB on aluminum stubs placed in a shuttle that fits the cryo-stage. Sample stubs are loaded into the shuttle under liquid nitrogen in a workstation outside the FIB, and a vacuum transfer device is used to transport the shuttle from the workstation to the preparation chamber and back. The thermal mass of the shuttle ensures that no significant temperature change occurs during the <1 min transfer. The shuttle is further transferred into and out of the cryo-FIB

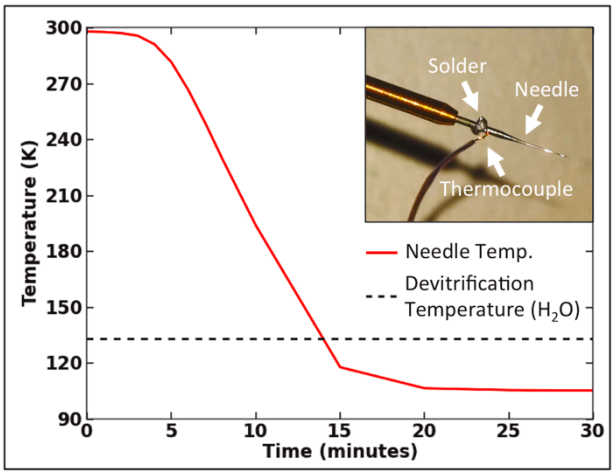

Figure 3.2 Nanomanipulator needle cooling profile. The needle must be maintained below the devitrification temperature of the sample to prevent structural alterations and damage due to crystallization during lift-out. A T-type thermocouple was soldered to a cooled nanomanipulator needle (inset) and the temperature was measured as a function of cooling time. The approximate minimum devitrification temperature of water is shown as a dashed line, which the needle surpasses with under 15 minutes of cooling and stabilizes well below.

chamber through a valve connecting it to the preparation chamber. Once the final lamella has been prepared and the shuttle is transferred back to the workstation, the lamella is removed from the shuttle under liquid nitrogen, placed in a cryo-TEM grid storage box, and stored in a liquid nitrogen dewar.

To attach a lamella to the cooled nanomanipulator needle in preparation for lift-out and subsequently to a TEM half-grid for thinning, an FEI Selective Carbon Mill (SCM) gas injection system (GIS) is used. The SCM introduces water vapor into the chamber, which has previously been shown to selectively enhance FIB milling of polymer-based materials at room temperature [172]. The cryogenic sample temperature in cryo-FIB, however, results in the water vapor depositing nearly uniformly as amorphous ice, enabling sample attachment. A schematic of these cryo-FIB components is provided in Figure 3.3a. To ease handling and storage of the final lamella, as well as prevent the

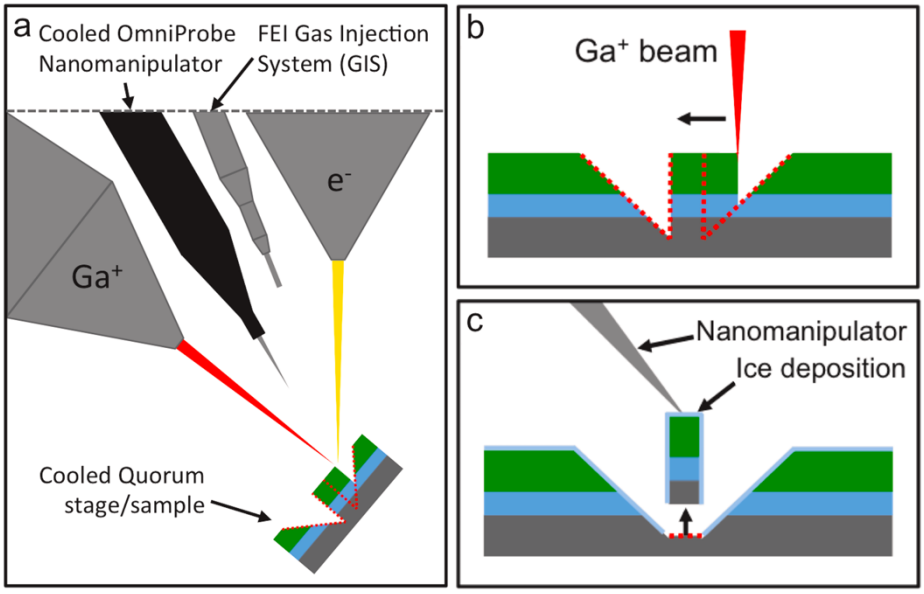

Figure 3.3 Schematic of the interior arrangement of the cryo-FIB and lift-out process, with corresponding SEM images. (a) Cryo-FIB interior components consist of a cooled OmniProbe nanomanipulator, an FEI selective carbon mill gas injection system (which provides water vapor injection), a Quorum cold stage, and electron and gallium ion beams, separated by 52 degrees. Steps to produce a lamella from a bulk sample include milling trenches on either side of the site of interest (b,d), lowering the nanomanipulator needle to the surface of the initial lamella, attaching the needle with water vapor, and cutting the lamella free and lifting it out (c,e). The lamella is then attached to a half-grid with water vapor, the needle is cut free, and the lamella is thinned to electron transparency.

half-grid from falling through the cryo-TEM holder tip while loading under liquid nitrogen, we adhere the half-grid to a molybdenum slotted grid using M-Bond 610 epoxy, providing a rigid support. The half-grid is attached such that the curved side of the grid is in contact with the slotted grid, ensuring sufficient clearance for the nanomanipulator to reach the sample attachment location without contacting the slotted grid. These lift-out grids are transferred into and out of the cryo-FIB on a sample stub modified in-house to include a small lip and cam mechanism, which secures the grid to the stub and allows for simple grid removal under liquid nitrogen. Figure 3.1c shows a shuttle with a modified grid in the cam mechanism of the customized stub.

To minimize ice contamination during transfer to the cryo-TEM, samples are loaded into a Gatan 626 Cryo-Transfer Holder (Gatan Inc., Pleasanton, CA, USA) under liquid nitrogen. A shield on the holder tip is closed over the sample during the brief transfer to the microscope. For this work, a 200 kV monochromated FEI Tecnai F20 ST (S)TEM equipped with beryllium cryo-blades to reduce ice contamination of the sample in the vacuum of the microscope was used. A high-angle annular dark field (HAADF) detector at camera lengths of 100-300 mm was used for imaging, while a Gatan imaging filter 865-ER and an 80mm^2 Oxford X-Max detector were used to acquire EELS and EDX spectroscopic data, respectively.

3.2.3 In Situ Localization of Subsurface Structures

Given the site-specific nature and limited throughput of cryo-FIB preparation, localization of subsurface structures of interest prior to lift-out is crucial for achieving an acceptable yield of these structures in the lamellas produced. While this challenge was recently addressed in cryo-FIB preparation of fluorescently labeled biological specimens using correlative cryo-FLM and cryo-FIB (discussed above), alternative methods are needed for buried structures that lack fluorescent signatures.

Ideally, feature localization should be performed *in situ*, i.e. directly inside the FIB, as this would simplify the process compared to a correlative two-instrument approach. Depending on the experimental set-up, dual-beam (FIB/SEM) systems provide access to a range of signals, some of which can be used to detect subsurface structures. Backscattered electrons (BSE), for example, can escape from a moderate depth in the sample due to their high energy, revealing subsurface information. Additionally,

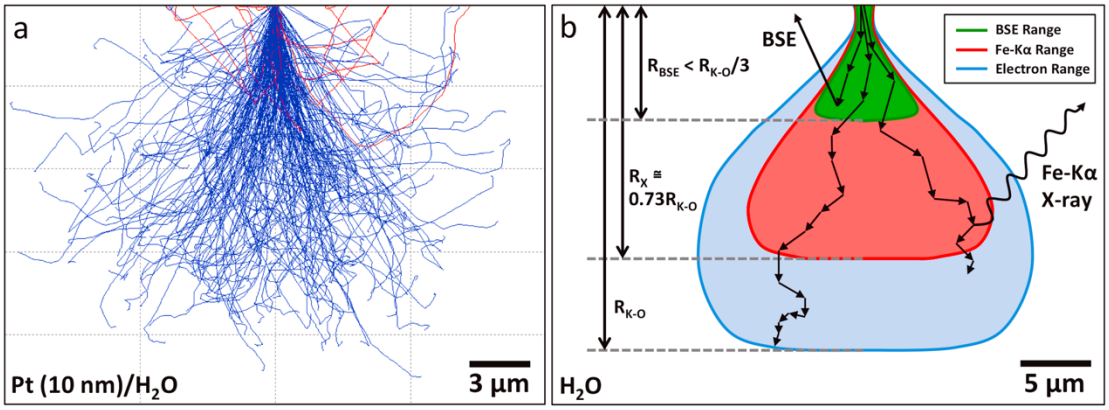

Figure 3.4 Results of electron scatting calculations and Monte Carlo simulations. (a) Example of 30 keV electron trajectories in a water with 10 nm platinum capping layer, calculated with the CASINO program. Blue paths signify electrons that came to rest in the material, while red paths indicate backscattered electrons. (b) Results from calculations of the Kanaya-Okayama primary electron range, characteristic x-ray generation range, and data for backscattered electron range, showing the useful depth probed by the characteristic x-ray signal exceeds that of the backscattered electron signal. Approximate excitation volumes of the signals are also shown, using the shape of total energy deposition contours from CASINO as a guide.

modern silicon drift X-ray detectors enable two-dimensional mapping of characteristic X-rays produced in the sample within reasonable timescales. EDX can therefore also be used to probe the interior of the sample. To evaluate the capabilities of these two signals, a model system of iron oxide particles grown in a silica hydrogel and protected by a 10 nm platinum capping layer was chosen. We performed Monte Carlo simulations of electron trajectories and sample interactions using MC X-Ray [173] and CASINO [174], with parameters chosen to mirror our experimental set-up (discussed below). An example of electron trajectories in a sample without an iron particle calculated with CASINO is shown in Figure 3.4a and demonstrates the range of 30 keV electrons in water.

To gain insight into the depth probing capabilities of different signals, electron scattering calculations allow for a comparison of the relative ranges of BSE and

characteristic X-ray generation in a water sample. Using a simple atomic model and empirical data, Kanaya and Okayama estimated the range for electrons incident on a material, in microns, as follows [175]:

$$R_{KO} = \frac{0.0276\,A}{Z^{8/9}\rho} E_o^{5/3} \tag{3.1}$$

where A is the atomic weight (g/mol), Z is the atomic number, and ρ is the density (g/cm^3) of the target material, and E_o is the incident electron beam energy (keV). By using values appropriate for water, we can estimate the maximum range of 30 keV electrons in our hydrogel sample, $R_{KO} \cong 24$ μm, which is well beyond the depth of a typical lamella (on the order of 10 μm). Assuming this energy dependence can be used to calculate the remaining beam energy at a particular depth (a simple continuous-slowing-down approximation [59]), the maximum depth a primary electron could reach before returning to the surface is $\sim R_{KO}/2$. Monte Carlo simulations previously performed on a variety of materials, however, show that this number typically remains below $\sim R_{KO}/3$ [6]. In comparison, the range where characteristic X-ray generation can occur, in microns, is given by [6]:

$$R_X = \frac{0.064}{\rho}(E_o^{1.68} - E_c^{1.68}) \tag{3.2}$$

where E_c is the energy of the characteristic X-rays generated (keV). For Fe-*Kα* X-rays generated in water using 30 keV electrons the range $R_X \cong 0.73R_{KO}$, which exceeds the range for BSE by a factor of greater than two. The X-ray signal can therefore be used to probe deeper into the material. A schematic of the relevant depths for BSE and X-rays, as well as the approximate corresponding excitation volumes of these signals, is shown in Figure 3.4b.

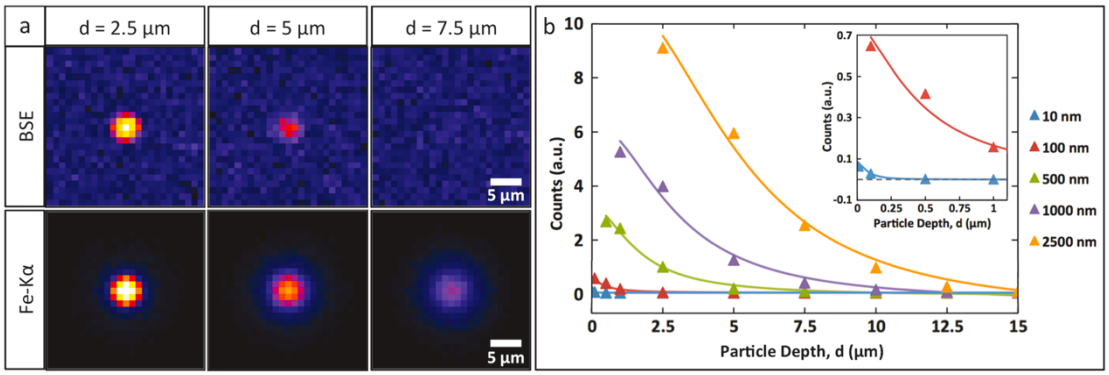

Figure 3.5 Results of Monte Carlo simulations calculated with the MC X-ray program. (a) Detected backscattered electron and Fe-*Kα* X-ray signals from a 2.5 µm radius iron oxide particle at various depths in a water sample with a 10 nm platinum capping layer, showing the increased depth probing ability of the characteristic X-ray signal. The images in each row are normalized to the maximum intensity of the 2.5 µm depth image. As such, an adjustment in contrast settings would allow the X-ray signal to be clearly visible to depths well beyond the lamella dimensions, while the backscattered electron signal is lost in the background noise beyond roughly 5 µm depth for this particle size. (b) Peak intensity recorded from simulations performed on a number of particle radii (with a sigmoid curve fit as a guide to the eye), showing the dependence of depth detection ability on particle size. In a real experiment, the maximum detectable range would be dependent on acquisition time and background signal as well, but these results show the upper limits on what should be possible.

To gain a more detailed understanding of these signals, as well as visualize the viability of BSE imaging and EDX mapping for localizing subsurface features of interest, we performed Monte Carlo simulations of electron scattering in our model system. We simulated a range of iron oxide particle sizes embedded in water at various depths and beneath a 10 nm platinum layer to assess detection limits. A 30 keV electron beam was scanned over a constant two-dimensional field of view centered on the particle, and the BSE and Fe-*Kα* X-ray signals were computed using appropriate detector configurations (MC X-Ray Microscope settings modified from the default: 30 keV beam, 0.5 cm EDX detector radius, and 45° detector take-off angle). Figure 3.5a shows the BSE imaging and EDX mapping results for a 2.5 µm radius particle placed

at various depths in the material. Here, the depths indicated mark the center of the particle, i.e., at a depth of 5 μm the highest point on the particle is 2.5 μm below the sample surface (for proper convergence of the simulation, one additional nanometer of material was placed over the particle in situations where its radius equaled its depth). These simulation results demonstrate that while the BSE signal may detect particles of a high atomic number material near the sample's surface, the depth from which characteristic X-rays are detected, mapped by EDX, is much greater than that of the BSE signal. In fact, the X-ray range exceeds the depth of a typical lamella. An additional benefit to using the characteristic X-ray signal is the ability to differentiate clearly between elements of similar atomic numbers, which is more difficult with a BSE signal, especially for high atomic number materials [176].

The effect of particle size on the detected X-ray signal is shown in Figure 3.5b. Particles with radii from 10 nm to 2.5 μm were simulated up to 15 μm into the material (beyond a typical lamella depth). As expected, the depth at which particles can be detected by EDX decreases with deceasing particle size. Smaller particles, therefore, must sit closer to the surface of the sample to be localized. Experimentally, the maximum detection depth will also depend on factors such as background noise (Bremsstrahlung radiation and trace materials present) and acquisition time. Nevertheless, these simulations show with a high-quality sample and long enough acquisition times it may be possible to detect particles tens of nanometers in size hundreds of nanometers into the material.

We also demonstrate this technique experimentally for the system described above, and show good qualitative agreement with the Monte Carlo simulations. *In situ*

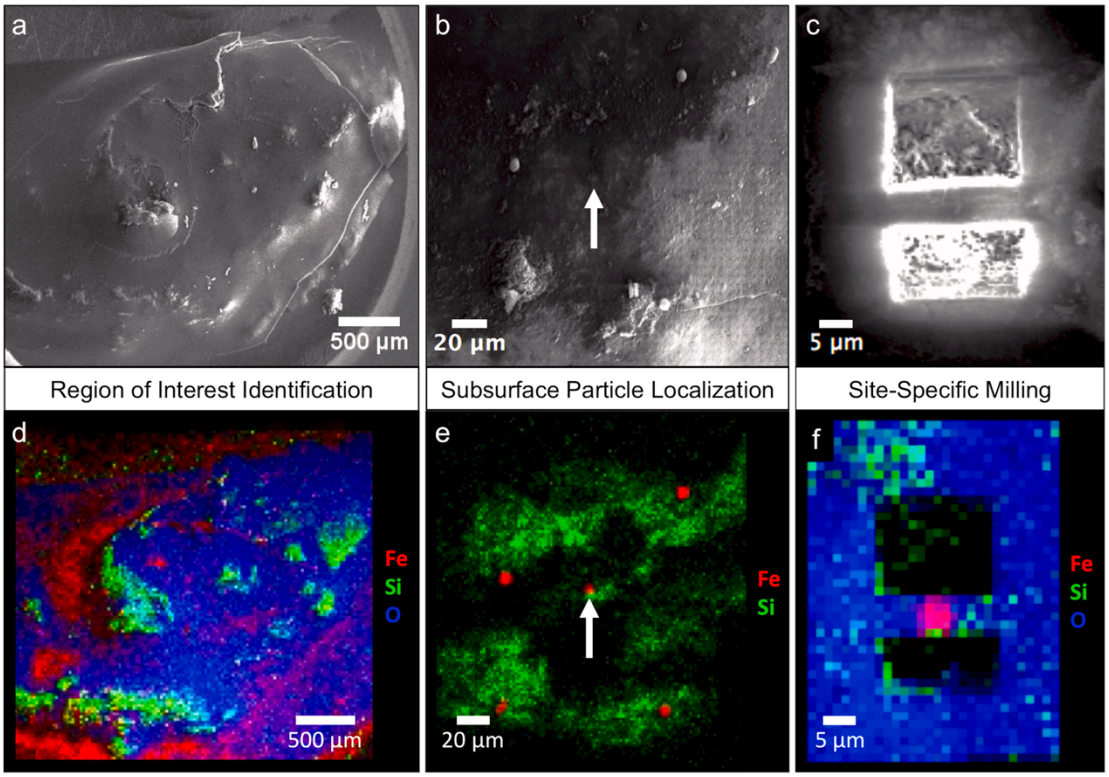

Figure 3.6 Energy dispersive X-ray (EDX) spectroscopy mapping for label-free in situ localization of subsurface structures for milling. (a) At low magnifications, electron images reveal very little about subsurface structures, while (d) EDX maps provide elemental distribution information about structures up to microns beneath the surface. (b,e) At moderate magnifications, secondary electron images can be compared to EDX maps, identifying and localizing subsurface structures with precision. (f) EDX maps also provide the ability to guide milling of specific subsurface structures, significantly increasing the yield of desired structures lifted out over imaging with electron signals alone (c).

localization of embedded iron oxide particles by EDX during different stages of the cryo-FIB lift-out process is shown in Figure 3.6. At low magnifications, an overview of the distribution of elements present in the sample is obtained and used to identify regions of interest for milling (Figure 3.6d). At higher magnification, individual particles are identified by EDX and the secondary electron signal is used to distinguish embedded particles from those at or near the surface of the sample (Figure 3.6d, e). Once a suitable particle has been located, EDX mapping precisely guides the milling process (Figure

3.6f), ensuring the final lamella contains the desired structure. As a result, this technique dramatically improves the yield of useful lamellas over milling "in the dark," without EDX.

3.2.4 Cryo-FIB Lift-Out Procedure

Cryo-FIB lift-out is conceptually similar to traditional FIB preparation of hard materials for TEM. In brief, once a structure of interest has been identified, cryo-FIB lift-out preparation proceeds as follow: Material is removed with the ion beam from either side of the structure of interest in triangular-shaped trenches, leaving a vertical lamella between the two. The lamella is then nearly cut free from the bulk sample with the ion beam using a "J-cut" around the edges of the lamella, leaving a small section at the top to keep the lamella secure until it is attached to the lift-out needle. A cooled nanomanipulator needle is then brought in close proximity to the lamella, water vapor from the GIS is used to attach the two, and the lamella is fully cut free from the sample. It is then lifted out of the bulk sample, attached to a TEM half-grid, again using water vapor, and finally thinned to electron transparency. The frozen lamella is then removed from the cryo-FIB and stored under liquid nitrogen until it is transferred to the cryo-STEM. A basic schematic of this process is shown in Figure 3.3b and 3.3c. SEM images of the lift-out process are shown in Figure 3.7, including final lamellas produced by the methods below.

The first two steps in the lift-out process, trench milling and the "J-cut", mirror traditional FIB techniques. Here, we provide details on how to optimize preparation conditions depending on the sample. First, the sample surface is tilted perpendicular to

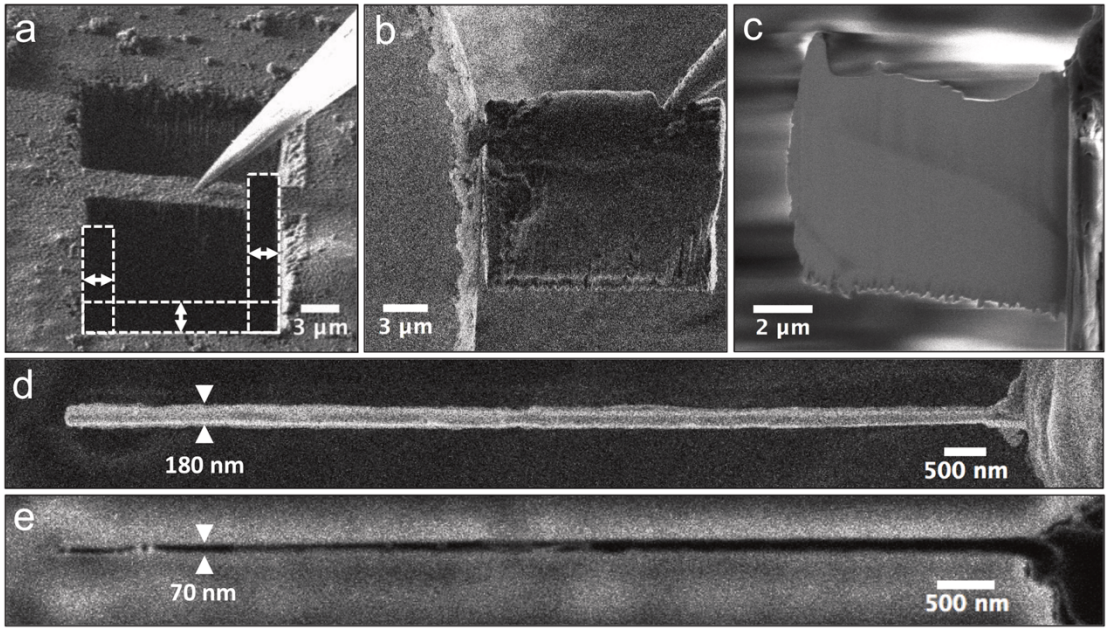

Figure 3.7 SEM images of the lift-out process steps, performed on a bulk silica hydrogel with embedded iron oxide particles. (a) Trenches are milled with the ion beam on either side of the desired structure, a "J-cut" is performed, and the needle is brought in close proximity to the sample. Water vapor subsequently deposited, attaching the needle to the lamella with amorphous ice. (b) The lamella is then cut free from the bulk sample, lifted out, and positioned near a TEM half-grid bar. (c) Water vapor attaches the lamella to the grid, the needle is cut free, and the lamella is thinned to electron transparency. Final thinning reduces the lamella to a uniform thickness on the order of 100 nm. (d) A top-down view shows the lamella thinness and homogeneity, here an early hydrogel lamella with a thickness of 150-180 nm. (e) A top-down image of a lamella created from a solid-liquid interface with protective surface layer shows materials in this configuration can be thinned to < 100 nm.

the ion beam and trenches are milled on either side of the structure of interest. The trenches are milled with either a "regular cross-section," where the milling region is repeatedly scanned with the beam, passing more frequently over the deep end of the trench, or a "cleaning cross-section," where a single slow pass of the beam is used, dwelling progressively longer towards the deep end of the trench. The cross-section used depends on the properties of the target material. For example, materials that redeposit a large amount while milling generally must be milled with a regular cross-

section, preventing accumulation of redeposited material in the trench. This may result in the surface of the lamella becoming coated with redeposited material, however. Cleaning cross-sections may be used to ensure the lamella surface is free of redeposited material, however, this milling type can result in material redepositing in the trench behind the slowly progressing beam. With either cross-section type, the trenches are typically milled five to ten microns wider than the desired lamella width, and a minimum of a few microns deeper than the feature of interest, ensuring room for the J-cut to be performed. Additionally, the trench opposite to the ion beam during the J-cut may be milled deeper, providing extra room for material sputtered from the J-cut. The deep ends of the trenches are positioned towards each other, as in Figure 3.3b, forming the cross-sectional lamella, typically 2-5 μm thick. Beam currents used to mill the trenches vary widely for different sample materials. For the soft hydrogel material, approximately 0.5 nA to 3 nA was used, taking typically upwards of ten minutes to mill the trenches. Harder materials require increased current to achieve the same results. Once the trenches are complete, the sample surface is tilted back perpendicular to the electron beam, giving the ion beam access to the lamella face. A J-cut is then performed, milling through the lamella around the edges in an approximately 1-3 μm wide rectangular "J" shape, as shown in Figure 3.7a, nearly cutting it free from the bulk sample. A small bridge, a few microns thick, is left at the top of the lamella on the side opposite of where the needle approaches, supporting the lamella. Both the trench separation, which defines the initial lamella thickness, and the J-cut width depend on the sample material. As above, lamellas produced from materials that redeposit a large amount of material must be thin, and the J-cut must be narrow, to minimize redeposited

material and avoid the lamella reattaching to the sample. Strongly charging samples, on the other hand, benefit from a wide J-cut to avoid lamella deflection and possible detachment during lift-out.

After the J-cut, the cooled needle is brought in close proximity to the lamella, as shown in Figure 3.7a, and attached with gas deposited from a GIS. In traditional FIB preparation a platinum-based organometallic precursor gas is injected into the chamber and "cracked" with the ion beam, depositing platinum metal locally and effectively "welding" the lamella to the needle. At cryogenic temperatures, however, many gases freeze on the cold surfaces, and as a result, a suitable gas must be chosen for cryo-FIB lift-out attachment. While various options have been suggested for this purpose [112,130,177], the following considerations led us to choose water vapor. First, the low atomic numbers of the elements in water minimize the effect of any remaining material on imaging in the cryo-STEM. Additionally, the use of water avoids introducing artificial carbon, which is crucial for samples where carbon characterization is key. Finally, attachment by water deposition happens on a timescale that minimize the effect of thermal drift of any component during attachment, while allowing the deposition to be monitored in real time through imaging with the electron beam, enabling the proper thickness to be selected. We typically deposit water vapor for ~10 seconds, which results in under a micron of amorphous ice on the cold surfaces and provides sufficient stability for attachment of the needle to the lamella. Once the needle is attached, the remaining small bridge is milled away, freeing the lamella from the bulk sample. If a long water deposition time or narrow J-cut are used, it may be necessary to briefly "clean" the J-cut of deposited ice using the ion beam before lifting the lamella out. Once

the lamella is free, the nanomanipulator is then used to lift it out of the sample on the needle and transport it to a half-grid, as shown in Figure 3.7b. Here, it is attached to the grid with a second water vapor deposition, and the needle is detached with the ion beam.

To minimize multiple scattering in the cryo-STEM, the lamella should be thinner than one mean free path, and thus requires further thinning. For example, the inelastic mean free path of 200-300 keV electrons, typical of the instruments used for cryo-TEM, is a few hundred nanometers in amorphous ice [178,179]. The goal for the final lamella thickness should then be on the order of 100 nm or less. To accomplish this thinning, the lamella is tilted back to the same orientation in which the trenches were milled, with the top edge of the lamella facing the ion beam. Material is then sputtered away from either side of the lamella with a series of decreasing ion currents, removing progressively smaller amounts of material with increasing precision as the lamella gets thinner. In contrast to traditional FIB preparation of hard materials, where cleaning cross-sections are typically used to remove small amounts of material, creating wedge-like lamellas that are exceedingly thin at the top, simple rectangular milling patterns are used in cryo-FIB to create uniformly thin final lamellas. To remove the material, the rectangular milling pattern is placed over one edge of the lamella when viewed from the top (or ion beam direction) and milling proceeds until all material within the rectangle is removed. This reduces the lamella thickness and removes "curtaining" from the surface. All milling steps are performed at 30 kV accelerating voltage, and for softer materials such as hydrogels, the initial thinning is usually performed at a beam current of approximately 50-100 pA. Depending on the initial lamella thickness, the first thinning steps typically remove ~1 μm or less from either side. As the lamella becomes

thinner, the beam current and milling pattern size (perpendicular to the face of the lamella) are progressively reduced, increasing precision by minimizing probe tails and slowing the milling rate for increased control. The final thinning is typically performed with 10 pA or less, removing only nanometers of material. As the lamella approaches the final thickness, beam deflection, sample drift, and even bending of the lamella can occur. As a consequence, the beam shift knobs must be monitored vigilantly, as even a small beam drift or deflection of the lamella can rapidly destroy the sample. A protective layer on top of the lamella, such as platinum, can help this by decreasing the sensitivity of the lamella to probe tails and accidental beam exposure [7].

The described cryo-FIB lift-out procedure provides sufficient control to produce homogeneously thin lamellas with smooth surfaces. For soft materials, such as hydrogels, lamellas down to ~100 nm thick can be produced. An early hydrogel lamella 150-180 nm thick is shown in Figure 3.7c and 3.7d. For materials more resilient to the beam, probe tails do less damage outside the intended milling area, allowing further thinning to be performed. An example of a less than 100 nm thick lamella from a solid-liquid interface protected by a hard metal capping layer is shown in Figure 3.7e. For soft materials that lack a protective surface layer but contain a resilient structure larger than the final lamella thickness, such as the iron oxide particle localized by EDX in Figure 3.6f, the resilient structure itself may be used to shield one interface with the soft material. In this case, the soft material above the structure is sacrificed, but the lower hard-soft interface is preserved. This approach also enables thinning of the lamella to less than 100 nm in thickness. An example of this is shown Figure 3.8, where final thinning was performed on only the left half of the iron particle, shielding the soft

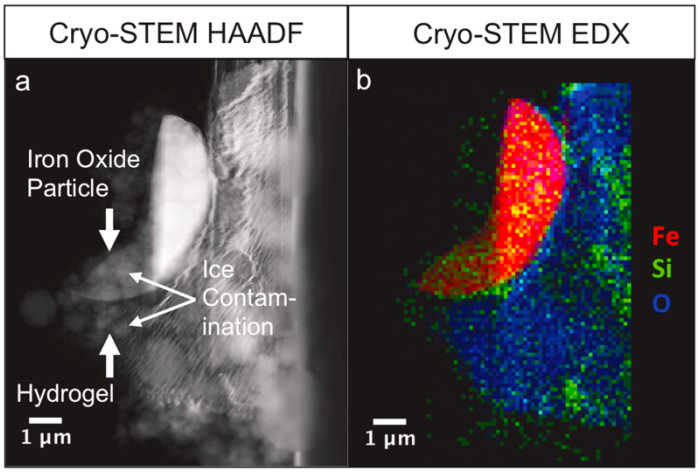

Figure 3.8 Cryo-STEM HAADF images and EDX maps of the hard-soft interface between a micron-scale iron oxide particle and the surrounding silica hydrogel in which it was grown (900 mM iron chloride; 4 week growth). The hard iron oxide particle was used to protect the lower interface with the soft hydrogel material. (a) Cryo-STEM HAADF image of the lamella. Ice contamination visible on the sample is due to an early non-optimized transfer from the cryo-FIB to the cryo-STEM. (b) EDX mapping reveals the distribution of the key elements in the lamella: iron, oxygen, and silicon.

hydrogel material below and preserving the interface between the two.

3.3 Results and Discussion

3.3.1 Cryo-STEM Imaging, EDX, and EELS

The quality of lamellas produced by these techniques allows nanoscale structural, elemental, and bonding information to be obtained from the sample by cryo-STEM. A large range of STEM characterization techniques available for room temperature work are also available for cryo-STEM, including HAADF imaging and convergent beam electron diffraction (CBED) for structural determination, and EDX mapping and EELS to obtain elemental distributions and local bonding information. We demonstrate these techniques in Figures 3.8 and 3.9 for iron (oxy-, hydr-)oxide phase crystals grown in silica hydrogels and prepared by cryo-FIB lift-out. Figure 3.8a shows a HAADF STEM

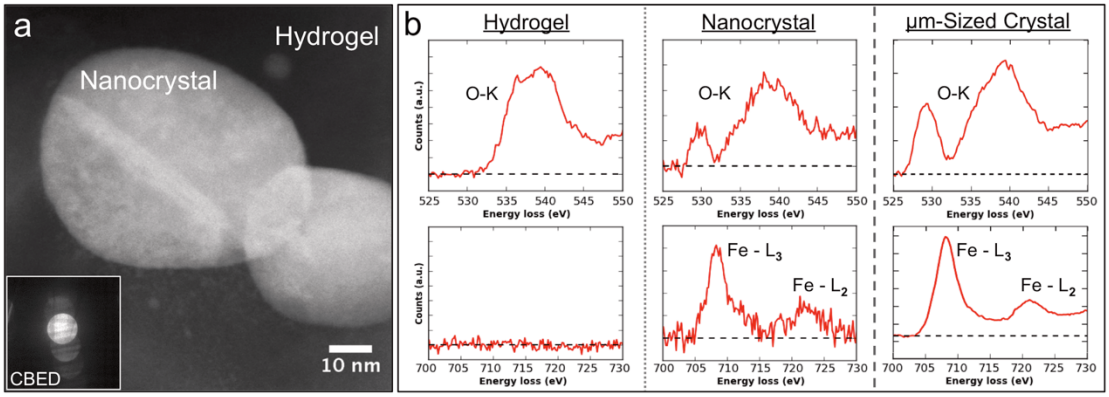

Figure 3.9 Nanoscale cryo-STEM HAADF imaging and EELS of iron (oxy-, hydr-)oxide crystals grown in silica hydrogel. (a) Cryo-STEM HAADF imaging reveals the nanoscale structure of embedded nanoparticles, and (a, inset) CBED confirms the particles' crystallinity. Cryo-STEM EELS provides elemental and bonding information about the surrounding material (b, first column) and the embedded nanocrystal (b, second column). Lamellas containing larger crystals, such as the one shown in Fig. 3.8, lack hydrogel above and below the particle which allows larger electron doses to be applied. This results in an EELS spectrum with improved signal-to-noise ratio (b, third column). The sample used in (b, third column) is taken after 4 weeks of reaction while all others are taken after 4 hours (900 mM iron chloride).

image of the hard-soft interface between a micron-sized iron oxide particle and the hydrogel in a lifted-out frozen lamella, where the material above the particle was sacrificed to preserve the soft hydrogel below the left portion of the particle, as discussed above. Additionally, HAADF STEM performed on precursor phase iron oxyhydroxide nanocrystals embedded in a silica hydrogel lamella (Figure 3.9a) demonstrates nanometer-scale imaging resolution for characterization of hard-soft interfaces. The CBED pattern (Figure 3.9a, inset) recorded on the particle confirms its crystallinity.

In addition to imaging the material's structure, elemental and chemical bonding information across the hard-soft interfaces were obtained through cryo-STEM EDX and EELS, respectively. Figure 3.8b shows an EDX map of the micron-sized iron oxide particle and surrounding silica hydrogel material, revealing the distribution of silicon

and iron across the interface. Cryo-STEM EELS data acquired from the hydrogel embedded nanocrystal shown in Figure 3.9a display a strong iron *L*-edge and oxygen *K*-edge prepeak (Figure 3.9b, second column), consistent with published reference spectra for iron (oxy-, hydr-)oxide phase compounds [180]. As expected, these signals were not present in the surrounding hydrogel, instead the O-*K* fine structure confirms the presence of water ice [181].

A limiting factor for characterizing soft materials and solid-liquid interfaces by cryo-STEM is radiation damage. The critical dose where damage is induced is typically substantially lower in soft materials and liquids than in hard materials, which limits the obtainable signal-to-noise ratio (SNR) [87,129,145]. This is evident from the difference in SNR of EELS spectra recorded on nanoscale and micron-sized crystals shown in Figure 3.9b. The nanocrystal was surrounded by hydrogel, which limited the acceptable dose for spectroscopy. However, in the case of the micron-sized particle, no hydrogel material remained above and below the particle, which resulted in a substantially larger acceptable dose and a greatly improved SNR (last column in Figure 3.9b). However, in both cases we have shown that information about the bonding state of the sample can be extracted using cryo-STEM EELS.

3.4 Conclusion

Analytical cryo-STEM techniques combined with site-specific methods for preparing bulk frozen soft materials or solid-liquid interfaces will enable high spatial resolution characterization of biological, chemical and physical processes that occurs in these systems. Recent advances in cryo-FIB techniques have made progress in this direction,

including proof of concept demonstrations of lift-out sample preparation methods. Here, we have reported developments of this technique that will enable more widespread utilization of cryo-FIB lift-out. Label-free *in situ* localization of subsurface structures of interest by EDX mapping, as demonstrated here, dramatically increases their yield in the lamellas produced. Additionally, we discussed how to optimize the technique to create thin and homogeneous lamellas for cryo-STEM analysis of intact solid-liquid and hard-soft interfaces extracted from bulk samples. To demonstrate these capabilities, nanometer-resolution HAADF STEM imaging of iron oxyhydroxide nanocrystals embedded in a silica hydrogel lamella was performed. Additionally, cryo-STEM EDX allowed elemental mapping across the solid-liquid interface of an iron oxide crystal grown in a silica hydrogel and cryo-STEM EELS provided local bonding information. Our results establish that cryo-FIB lift-out provides a path to access internal solid-liquid interfaces with the liquids intact and stabilized by rapid-freezing. In combination with analytical cryo-STEM, the technique can deliver nanometer scale structural, elemental, and chemical information about these interfaces. As a consequence, cryo-FIB lift-out and cryo-STEM will be able to facilitate advancements in fields where nanoscale information about solid-liquid interfaces is critical, such as crystal growth, biomineralization, and energy materials research.

CHAPTER 4

NANOSCALE MAPPING OF SOLID-LIQUID INTERFACE PROCESSES IN LITHIUM-METAL BATTERIES

Solid-liquid interfaces play a critical role in a range of chemical, physical, and biological processes, but are often not fully understood due to the lack of high-resolution characterization methods that are compatible with both solid and liquid components. The interplay between interface chemistry and rough, dendritic deposition of some metals, for example, remains unresolved and hampers the development of energy-dense rechargeable metal-anode batteries that are durable and safe. Here, we utilize a cryogenic electron microscopy approach to directly probe the native structure and chemistry of lithium dendrites and solid-electrolyte interphase layers formed on cycled lithium metal anodes. We identify two distinct dendrite types, one of which unexpectedly consists of lithium hydride and may contribute disproportionately to capacity fade. The unique insights into lithium dendrite formation provided here demonstrate the potential of cryogenic electron microscopy for probing nanoscale processes at intact solid-liquid interfaces in functional devices such as rechargeable batteries.

(Originally published: Zachman, M. J., Tu, Z., Choudhury, S., Archer, L. A. & Kourkoutis, L. F. Cryo-STEM mapping of solid–liquid interfaces and dendrites in lithium-metal batteries. *Nature* (in press))

4.1 Introduction

Solid-liquid interfaces play a key role in synthesizing novel materials [182], biomineralization [142], electrocatalytic fuel conversion and electrolysis [116], electrochemical energy storage [5,117], and photoelectrochemical electricity and fuel production [115,183]. Processes that occur at these interfaces are, however, difficult to study due to their complexity and the inherent difficulty of characterizing intact buried interfaces at high spatial resolution, necessitating the development of new analytical techniques [35]. One example is the formation of dendrites during electrodeposition of metals, which is closely coupled to processes at the metal/liquid-electrolyte interface [31,118], including the formation of a nanoscale solid-electrolyte interphase (SEI) layer typically composed of electrolyte breakdown products [118]. In electrochemical devices such as metal-anode rechargeable batteries, these processes and the resulting dendritic growths lead to rapid capacity fade and safety concerns. Despite intensive efforts by researchers worldwide over several decades [5] these processes are not fully understood [184–187]. Rechargeable metal-anode batteries able to live up to the promise of significantly enhanced energy density have therefore been elusive.

Direct observation of the nanoscale structure and chemistry at solid-liquid interfaces could significantly aid our understanding of processes occurring in these complex systems. Accurate characterization of electrode-electrolyte interfaces is, however, challenging due to the volatility of commonly used liquid electrolytes, the high chemical reactivity of metal anodes such as lithium, and the fact that the region of interest is an interface between two condensed phases of matter. To address this, the liquid is

typically removed and the electrode of interest washed and dried before being characterized by traditional methods, which alters the structure and chemistry of the solid-liquid interface [9]. For example, cryo-transmission electron microscopy (cryo-TEM) has recently been utilized to image the atomic structure of lithium dendrites grown on a copper TEM grid, opening a path to study chemically reactive and beam-sensitive battery materials [95,99]. However, in this approach the sample was removed from its native electrolyte environment to expose the dendrites and ensure electron transparency in the electron microscope.

Here, we adapt a technique used in biology to enable cryo-TEM of hydrated specimens, immobilization of liquids by rapid freezing [10], to preserve the liquid and native structure at solid-liquid interfaces in lithium-metal batteries (LMBs). To access the nanoscale interior structure and chemistry of the dendrites and their interfaces in LMBs, we couple cryogenic scanning transmission electron microscopy (cryo-STEM) and electron energy loss spectroscopy (EELS) with cryo-focused ion beam (cryo-FIB) "lift-out," a technique we recently developed to prepare buried solid-liquid interfaces for cryo-STEM (see Chapter 3) [123]. By maintaining dendrites in their electrolyte environment and avoiding potentially structure- and interface chemistry-altering washing steps, we discover two families of dendrites coexist on a Li anode, each displaying distinct structure and composition. One family has an extended SEI layer, while the other has a compact SEI layer. Additionally, while dendrites formed during electrodeposition are generally assumed to be composed principally of metal, based on the physical deposition mechanisms proposed by formation models [33], we

demonstrate the presence of lithium hydride dendrites, which may contribute disproportionately to battery capacity fade and failure.

4.2 Materials and Methods

4.2.1 Instrumentation and Experimental Details

We used an FEI Strata 400S DualBeam Focused Ion Beam/Scanning Electron Microscope system (FIB/SEM) to characterize and prepare samples. It was fitted with a Quorum PP3010T cryo-SEM/FIB system, which included a liquid nitrogen (LN_2) cold stage and anticontaminator in the main FIB chamber, a preparation chamber (for sputter coating) with separate cold stage and anticontaminator that is attached to the FIB and separated by a valve, a stand-alone workstation for freezing and loading samples onto the specimen shuttle, and a vacuum transfer device for transporting samples between the workstation and prep chamber. In addition, we installed an Oxford OmniProbe Cryoshaft on our OmniProbe 200 nanomanipulator, which is thermally isolated from the room-temperature shaft by a ceramic section and cooled by a copper braid attached to the anticontaminator. Preparation of lamellas by cryo-FIB lift-out was carried out using the techniques described in Chapter 3. All milling was performed at an ion beam voltage of 30 kV. Trenches to form the initial lamella were generally milled with a beam current of a few nA. Thinning of the lamella was first conducted with a beam current of hundreds of pA, decreasing with lamella thickness to a final thinning with tens of pA. After cryo-FIB lift-out preparation, cryo-STEM samples were transferred back into LN_2 in the workstation where they were loaded into cryogenic sample storage boxes and transferred to a large LN_2 storage dewar.

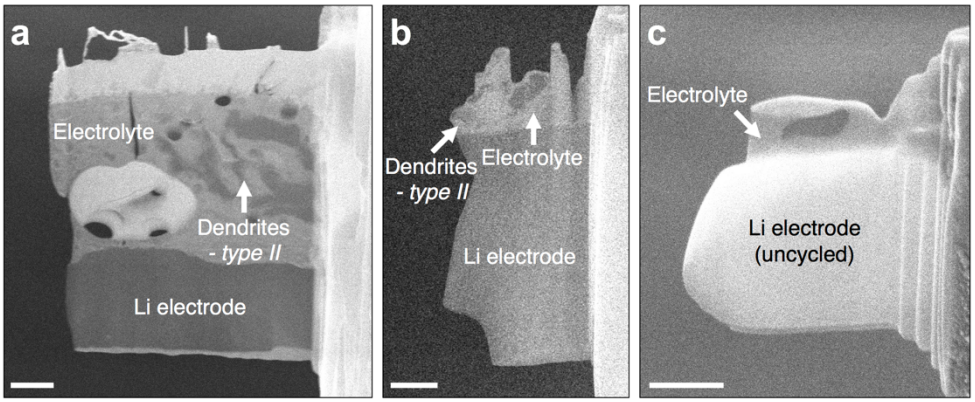

Figure 4.1 Examples of lamellas prepared from coin cells for cryo-STEM analysis. (a, b) Lamellas containing type II dendrites above lithium electrodes. The lamella in (a) contains a F-rich structure as well. Different electrolyte thicknesses and milling parameters were used to prepare these lamellas, resulting in different final dimensions. (c) A lamella produced from an uncycled electrode, used to obtain reference spectra. Note that the increased signal of the uncycled electrode is due to different image acquisition parameters, not a material difference. Scale bars 1 µm.

Cryo-STEM characterization of these samples was performed on an aberration corrected FEI Titan Themis operated at 300 kV. The microscope was equipped with an X-FEG high-brightness gun and a high-resolution Gatan imaging filter (GIF Quantum 965) for electron energy loss spectroscopy. Standard Gatan side-entry cryo-transfer holders (Model 626 and Model 915) enabled transfer of the samples into the microscope and maintained their temperature near -180 ˚C throughout the experiment. The samples were loaded into the holder under liquid nitrogen to minimize ice contamination. During transfer into the vacuum of the microscope, the sample was enclosed by a cryo-shutter which minimizes ice build-up. While throughput of the cryo-FIB lift-out/cryo-STEM workflow is continuing to be improved, it can approach that of room-temperature FIB and STEM techniques with proper optimization. Multiple lamellas were prepared for analysis by cryo-STEM for this project. Examples are shown in Figure 4.1, including an uncycled electrode for reference, and two containing type II dendrites. The O *K*-edge

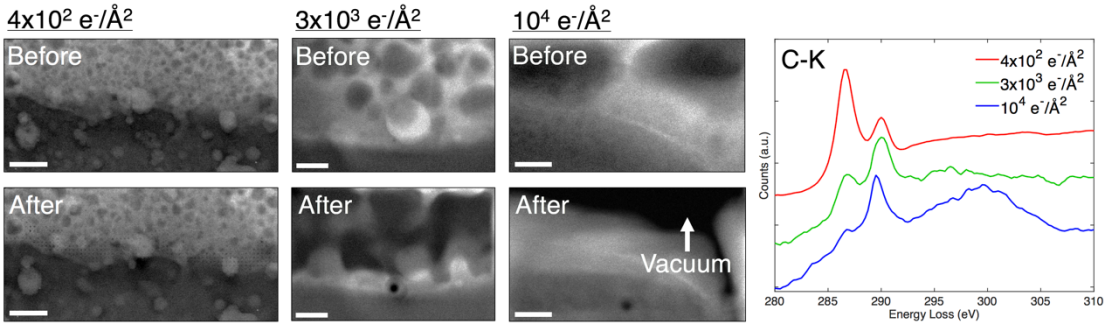

Figure 4.2 Dark-field cryo-STEM images of electrode-electrolyte interfaces taken before and after acquisition of EELS maps, and the corresponding map spectra. While some structural modification was present at low doses, likely due to liberation of hydrogen, a dose greater than 10^3 $e^-/Å^2$ was required for significant mass loss and spectral fine structure modification. In the center set of images above, approximately 50% of the material remained after the map, as determined by the ADF signal. At 10^4 $e^-/Å^2$ the material was completely removed in some areas, but the carbonate portion of the molecule remained. Doses applied during acquisition of the maps in the main text were less than the lowest dose shown here. Spectra are offset vertically for clarity. Scale bars 200 nm, 30 nm, and 60 nm, left to right.

reference spectra for Li_2O_2 and LiOH and the Li *K*-edge reference spectrum for LiH were taken on a 200 kV FEI F20 using the same cryo-transfer holders and loading techniques.

The probe current for EELS maps on the Titan was around 25 pA, confirmed by measurement on a direct electron detector with a high dynamic range [188], and pixel dwell times were 10-50 ms. The electron dose applied during acquisition of the spectroscopic maps shown in the main text was $5x10^1$ to $5x10^2$ $e^-/Å^2$. The small bubbles in the electrolyte appeared rapidly, beginning by the time the first image was taken, with a total dose below 10 $e^-/Å^2$. These were likely hydrogen liberated from the electrolyte solvent molecules [87], since carbon and oxygen *K*-edge fine structures in carbonates are known to be stable under the beam up to a dose of ~750 $e^-/Å^2$ at room temperature under a 200 keV electron beam [189]. The threshold damage for these materials under our cryogenic conditions using a 300 keV beam should be higher than this [87]. A series

Material	Damage Dose ($e^-/Å^2$)	Primary Damage Mechanism
Li (uncycled foil)	10^5	Mass loss/Minimal Li_2O formation
Li_2O	$>10^5$	Mass loss
Li_2O_2	$>10^4$	Mass loss/Li_2O conversion
LiOH	10^4	O_2 generation/Mass loss/Li_2O conversion
LiH	$>10^4$	Mass loss
EC:DMC - 1 M $LiPF_6$	$<10^2$ $>10^3$ 10^4	Slight structural modifications Mass loss/Initial fine structure changes Large mass loss/Conversion to Li_2CO_3

Table 4.1 Threshold electron doses and primary damage mechanisms observed for relevant materials. All of the damage thresholds listed are for cryogenic samples under a 300 kV electron beam. The primary damage mechanism of lithium is mass loss. While a very small amount of oxide can form, this is significantly less than the initial oxide impurities in an uncycled electrode, and occurs at $>10^5$ $e^-/Å^2$. Li_2O_2 and LiOH both initially suffer mass loss at or above 10^4 $e^-/Å^2$, and subsequently begin converting to Li_2O at higher doses, while Li_2O suffers only mass loss and no fine structure change. LiH is stable to above 10^4 $e^-/Å^2$, with mass loss occurring above this and little to no oxidation. The electrolyte material damages differently at different doses, with slight structural modifications occurring at low doses, and mass loss and fine structure changes occurring above 10^3 $e^-/Å^2$. At 10^4 $e^-/Å^2$ a significant portion of the mass is lost, leaving behind the carbonate portion of the solvent molecules, the fine structure of which is still intact at this dose.

of maps of the electrode-electrolyte interface taken at various total doses are shown in Figure 4.2, demonstrating the doses at which different types of damage occur. The damage mechanisms of these carbonate solvents are liberation of hydrogen at low doses, resulting in structural changes such as the bubbling observed. At doses $>10^3$ $e^-/Å^2$ mass loss becomes significant, and the fine structure of the ~287 eV peak is affected. At 10^4 $e^-/Å^2$ the mass loss is severe, producing holes in the sample, and leaving behind mainly the carbonate portion of the solvent molecules. The fine structure associated with this part of the molecule survives high doses, however. These findings are summarized in Table 4.1. Based on our damage analysis, we do not expect the fine structure to have been altered in the maps taken in the results section, though slight structural modifications were present, as expected (Figure 4.3).

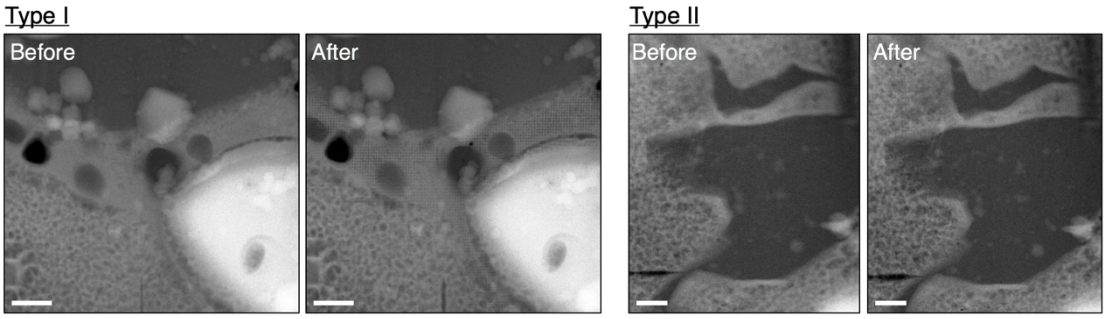

Figure 4.3 Before and after annular dark-field STEM images of the regions where the EELS maps in the results section were taken. Small structural changes were observed in the organic materials, which is expected given our damage analysis. This is likely due to liberation of hydrogen from the molecules, which occurs at low dose. The fine structure is not significantly affected until approximately an order of magnitude higher dose than was applied during these maps, which was on the order of 10^2 $e^-/Å^2$. Scale bars 300 nm.

4.2.2 Reference Spectra Acquisition

The reference spectra for the lithium metal and Li_2O samples were acquired on the Titan in similar conditions to above. The Li *K*-edge for lithium metal was recorded on an uncycled lithium electrode, and the Li_2O spectrum was recorded on a lithium electrode oxidized in the microscope by warming to room temperature and exposing the electrode to the beam. Both samples were produced by cryo-FIB lift-out. The electron dose for the metal spectrum was 10^4 $e^-/Å^2$, and no change in fine structure was recorded by doubling this dose. The oxide spectra were acquired with a total dose of ~10^2 $e^-/Å^2$. While we observed that other lithium-oxygen compounds converted to Li_2O under the beam, no change to the Li_2O fine structure was observed at high doses.

We acquired the lithium peroxide and hydroxide reference materials from Sigma Aldrich, crushed them into a fine powder using a mortar and pestle, and pressed a holey carbon TEM grid onto the powder to adhere some to the grid. The LiH was prepared in an argon-filled glove box due to its air sensitivity, and removed in a sealed vial which

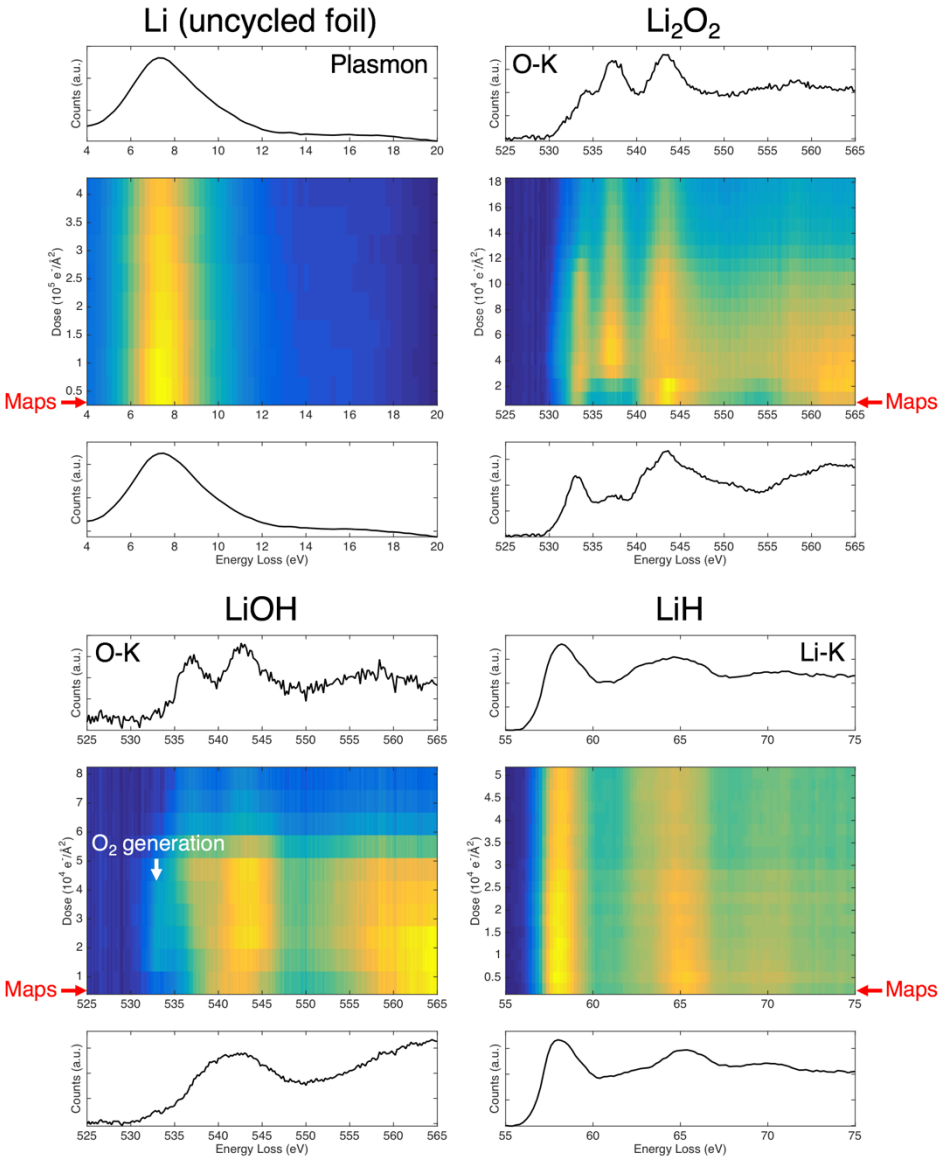

Figure 4.4 Example damage series profiles and initial/final spectra taken for lithium materials relevant to this study over a range of doses where damage occurs. All spectra were recorded at cryogenic temperatures. We found all oxide materials convert to Li_2O under large doses. Li_2O and LiH are primarily affected by mass loss, with no significant fine structure changes. Note that maps presented in the main text were acquired at doses lower than the dose indicated by the red arrows shown at the bottom of the plots, on the order of 10^2 $e^-/Å^2$.

was opened under liquid nitrogen, eliminating air exposure. The other stable samples were also immediately placed under liquid nitrogen after preparation to minimize unnecessary air exposure. On the F20, we used a probe current of ~75 pA. A total dose

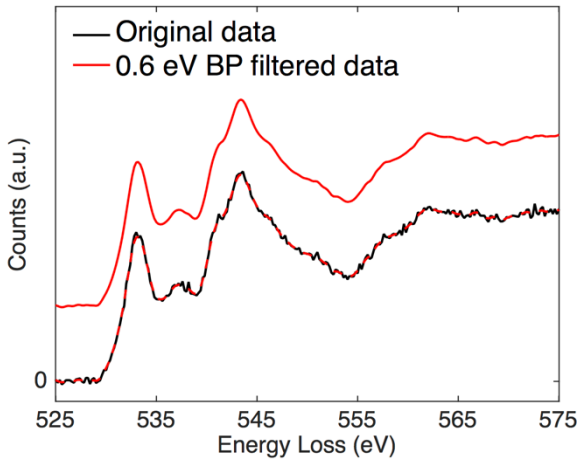

Figure 4.5 Comparison of Li_2O_2 O-K edge spectrum before and after 0.6 eV band pass filter. A 0.6 eV band pass filter was applied to the O-K spectra acquired on the F20 to remove high frequency noise. This preserved the main features of the edge while eliminating those below the instrument's energy resolution.

$<10^4$ $e^-/Å^2$ was applied to the oxides during acquisition, which we found was a few times lower than the dose necessary to induce a significant O-*K* fine structure change. The LiH Li-*K* spectrum was acquired with a total dose on the order of 10^3 $e^-/Å^2$, and no significant fine structure change was observed under any dose, measured to greater than 10^4 $e^-/Å^2$. All of the threshold damages for materials relevant to this study and the corresponding damage mechanisms are shown in Table 4.1, and examples of damage series profiles used to establish these values are shown in Figure 4.4.

To align the energy axis between the O-*K* spectra acquired on the Titan and the F20, we used the Li_2O peak at ~535 eV. The Li-*K* spectra were close enough to the zero-loss peak that no shifting of the spectra was necessary. Additionally, spectra acquired on the F20 were bandpass filtered by 0.6 eV to reduce noise below the energy resolution of the microscope. This reduced high frequency noise while preserving larger features accurately, with only a slight reduction in sharp peaks. An example is shown for the

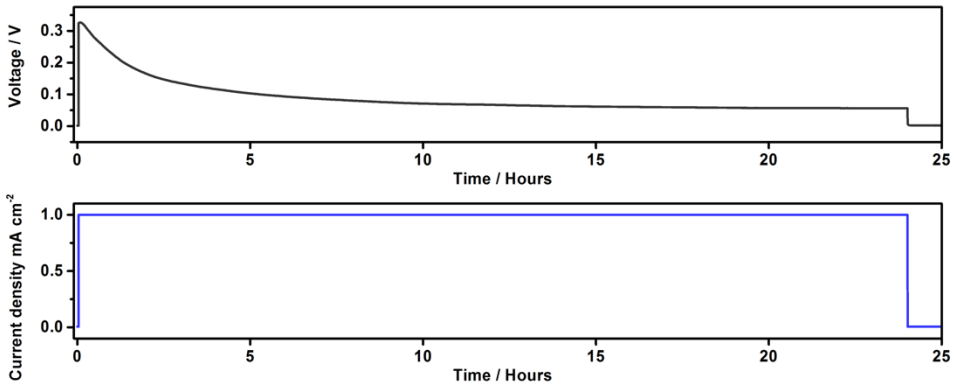

Figure 4.6 Charging profile from a symmetric lithium coin cell. A constant current of 1 mA/cm2 was applied to the cells for 24 hours. The resulting voltage profile from one of the coin cells used is shown above.

Li_2O_2 O-*K* in Figure 4.5.

4.2.3 Coin Cell Battery Preparation

Symmetric lithium cells (CR2032 coin cells) were assembled with two lithium electrodes (MTI Corp., 450 μm thick) and 1M lithium hexafluorophosphate ($LiPF_6$) in ethylene carbonate:dimethyl carbonate (EC:DMC) (v:v = 1:1) as the electrolyte. Celgard 3501 was used as the separator. We subjected the cells to galvanostatic charging for 24 hours at a current density of 1 mA cm^{-2}. A charging profile from one coin cell used is shown in Figure 4.6.

To snap-freeze the samples, slush nitrogen was produced in the cryo-FIB workstation by vacuum pumping liquid nitrogen until it solidified. This enabled a higher cooling rate and reduced bubbling in the workstation. Slush nitrogen was chosen to avoid detrimental interactions of the electrolyte with typical organic cryogens [104]. The coin cells were opened at the cryo-FIB workstation and the electrodes separated and immediately plunged into the slush nitrogen to preserve the electrolyte on the

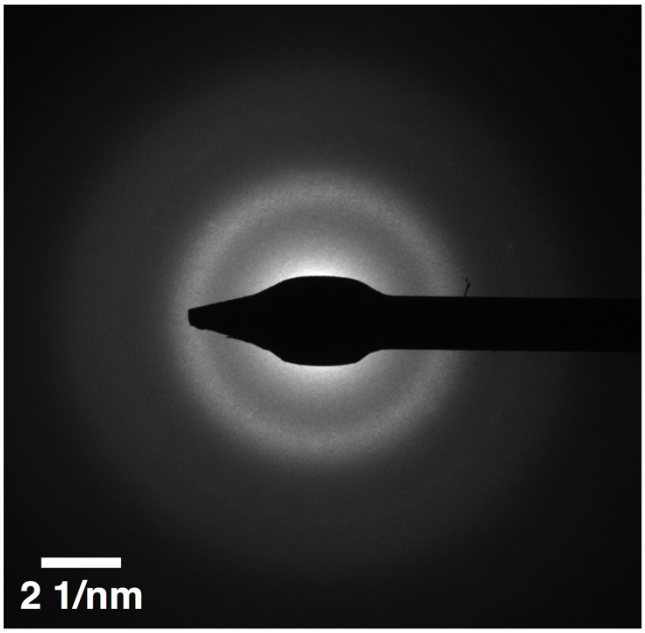

Figure 4.7 Amorphous diffraction pattern of the electrolyte recorded in a cryo-lamella produced by cryo-FIB lift-out. Cryo-TEM diffraction of the electrolyte on samples produced by cryo-FIB lift-out shows that it is frozen amorphously and does not recrystallize at any point in the preparation, storage, transfer, or characterization.

electrode. The frozen samples were then transferred into the preparation chamber attached to the cryo-FIB, typically sputter coated with a 5-10 nm layer of metal (Pt or Au-Pd) to reduce charging, and transferred into the cryo-FIB chamber. Lift-out samples produced for cryo-STEM were transferred back to the workstation, where they were loaded into cryogenic sample storage boxes under liquid nitrogen and transferred to a large LN_2 storage dewar. It is important to note that cryo-TEM diffraction on lamellas produced by cryo-FIB lift-out showed that the electrolyte was frozen amorphously, and remained so through all of the preparation, transfer, and characterization steps, as shown in Figure 4.7.

4.2.4 3D Reconstruction of Cryo-FIB Cross Sections

To reconstruct the three-dimensional dendrite structures, we used Avizo software (Thermo Fisher Scientific Inc.). Since the geometry of the FIB results in images of the cross sections taken at oblique angles to the cross section surface (the electron and ion columns are separated by 52 degrees and the sample surface normal is positioned parallel to the ion beam for milling), the 30-50 individual images were aligned vertically by the position of electrode surface and the appropriate length transformations were applied to the images to correct for the oblique viewing angle ($y = y'/\cos\theta$ and $z = z'/\sin\theta$, where y and z are the true object depth and height, respectively, y' and z' are the observed depth and height, and θ is the angle between the electrode surface normal and the electron beam). The dendrite and electrode structures were segmented by hand within each of the cross-sectional images, and these segmentations were connected in the perpendicular direction to reconstruct the three-dimensional structure.

4.2.5 EELS Map Processing

The large field of view of some EELS maps results in an energy shift of the entire spectrum at different points in the map. To accurately map edges and analyze edge fine structure across the field of view, the energy axis at each pixel was shifted to the proper location. Each map was acquired in DualEELS mode, with both low-loss and high-loss regions of the spectrum recorded. The low-loss maps included the zero-loss peak, the position of which was used to align the energy axis of the low and high-loss regions of the spectra simultaneously, resulting in a flat energy surface across the map.

To map elemental distributions, standard background subtractions were performed

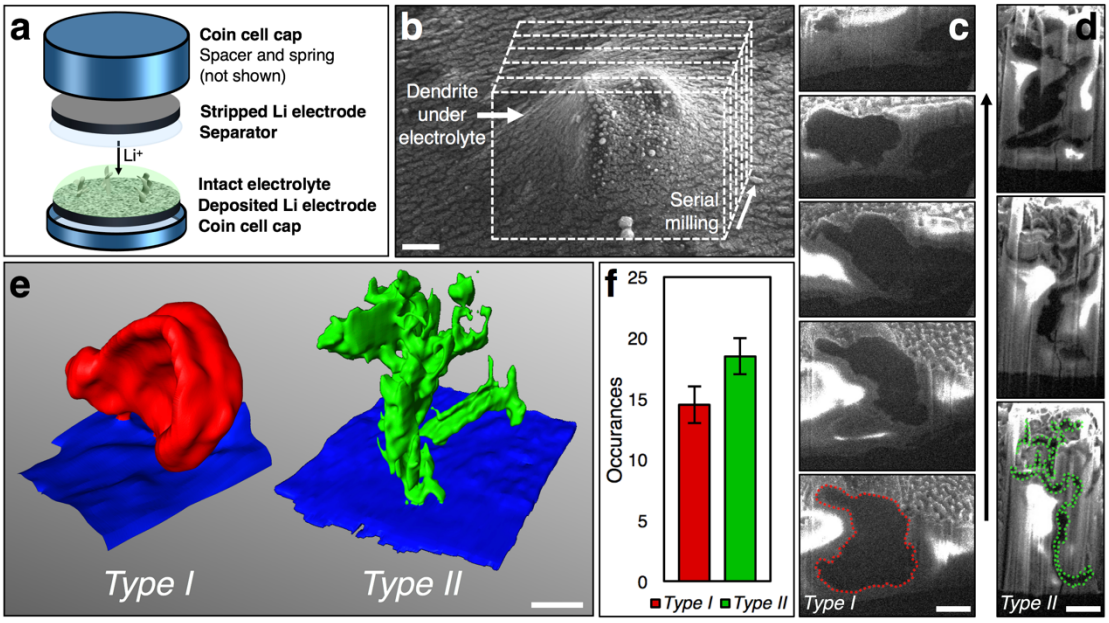

Figure 4.8 Characterization of dendrite morphologies by cryo-FIB. (a) Coin cell arrangement used. (b) Raised regions in the electrolyte, preserved on opened coin cell electrodes by plunge freezing, revealed buried dendrite locations. The electrolyte surface was sputter coated with a thin metal layer for increased conductivity. (c, d) Two distinct dendrite morphologies were observed in serial cross-sectional images produced by cryo-FIB/SEM. (e) Three-dimensional reconstructions of the dendrite structures highlight the morphological differences. (f) Roughly equal numbers of the two morphologies were present across many coin cells. (b)-(d) scale bars, 2 µm, (e), 5 µm.

using a linear combination of power laws (LCPL) fit and oversampling with a FWHM of 2 pixels to increase the background signal-to-noise [190]. Energy windows wider than the fine structure at the edge onset were integrated for elemental mapping, to minimize the effects of spatially varying fine structure on the apparent elemental concentrations. The fine structure of the edges was analyzed by multivariate curve resolution (MCR), which solves for a specified number of linearly independent spectral components in the data by means of a local minimization. A non-negativity constraint was imposed on the corresponding concentration profiles, since negative concentrations are not physical, but the spectra were not constrained. To improve signal-to-noise for

the MCR process the data was typically binned by four (spatially) before analysis. To display the spatial distribution of the resulting spectral components, we fit them back to the original data using the Matlab QR Solver, which takes advantage of QR factorization to minimize the residual of the equation S*C* = D. In our case, S is the matrix of spectral components returned by MCR, *C* is the matrix of concentrations to be solved for, and D is the matrix of original data. Using the original unbinned data (for the type I maps) or the original data binned by two (for the type II maps), we produced maps from the concentration matrix C for the corresponding MCR spectral components, such as in Figure 4.12 below.

4.3 Results

4.3.1 Lithium Dendrite Morphologies

Figure 4.8a shows a schematic of the symmetric lithium-metal coin cells used for these experiments. These contain 1M lithium hexafluorophosphate ($LiPF_6$) in ethylene carbonate:dimethyl carbonate (EC:DMC, v:v = 1:1) and a Celgard separator, and were charged at 1 mA cm^{-2} for 24 hours (see Methods). To preserve the electrolyte on the electrode surface, the cells were opened and the electrode immediately plunge frozen in slush nitrogen. To rapidly explore the morphology of the anode surface, we used cryo-FIB to mill a series of cross sections through the interface where surface structures were large enough to be localized by raised regions in the frozen electrolyte (Fig. 4.8b). We imaged each successive cross section (Fig. 4.8c, d), which revealed two distinct deposit morphologies that we will refer to as Type I and Type II dendrites. Type I dendrites were on the order of 5 μm across with low curvature, while Type II dendrites,

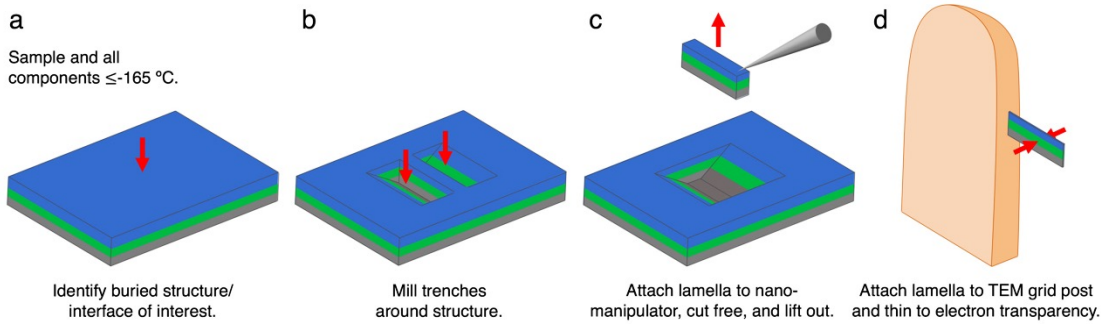

Figure 4.9 Schematic of Cryo-FIB lift-out sample preparation process. (a) A buried structure or interface is identified for preparation. In our coin cell batteries, raised regions of electrolyte were used to localize buried dendrites. (b) Trenches are then milled around the site of interest, forming a vertical cross-sectional lamella containing the structure or interface. (c) A cooled nanomanipulator needle is then attached to the lamella by depositing amorphous ice. The lamella is cut free from the sample and lifted out. (d) Finally, the lamella is attached to a TEM grid post with additional ice deposition, cut free from the nanomanipulator, and thinned to electron transparency.

conversely, were generally hundreds of nanometers thick and tortuous. We did not observe any spatial correlations between dendrite types, or cases where one dendrite type clearly formed on the other. To gain insight into their three-dimensional (3D) morphology, we reconstructed the 3D structure of the dendrites from the acquired two-dimensional cross-sectional images (Fig. 4.8e), as has been shown with biological samples previously [191]. The electrode contact areas for the individual structures can, thereby, be directly compared, revealing the widths of type II dendrite contact areas were more than an order of magnitude smaller than those of type I. This suggests type II dendrites may become disconnected from the electrode more easily during cycling and, in combination with their approximately equal numbers (Fig. 4.8f) and volumes, would therefore contribute disproportionately to active electrode material loss and capacity fade due to electrochemically "dead" lithium.

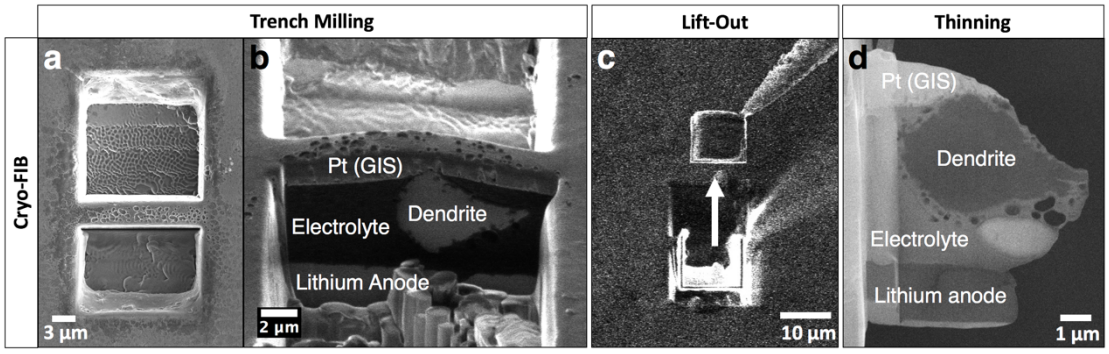

Figure 4.10 Cryo-FIB lift-out sample preparation process. (a, b) Trenches are site-specifically milled around a structure of interest, here a dendrite embedded in frozen electrolyte above the anode, leaving a vertical lamella containing the structure. The sample is aligned in the microscope so that the electrode surface normal is parallel to the electron beam direction in (a), and tilted by 52 degrees to image the lithium anode/electrolyte interface and the electrolyte embedded dendrite in (b). (c) A cryo-cooled nanomanipulator needle is then attached to the cryo-immobilized lamella by water vapor deposition from a gas injection system, the lamella is cut free from the larger sample, and it is lifted out. (d) The lamella is then attached to a cooled TEM grid with a second water vapor deposition, the nanomanipulator is cut free, and the lamella is thinned progressively to electron transparency with the ion beam.

4.3.2 Nanoscale Lithium Dendrite and SEI Layer Structure and Bonding

While cryo-FIB/SEM techniques provided valuable morphological information, we used cryo-STEM and EELS to obtain high-resolution structural and chemical information about the dendrites and their associated solid-electrolyte interphases. Cryo-FIB lift-out was used to extract cross-sectional lamellas of plunge frozen anode-electrolyte interfaces from coin cell batteries and thin them to electron transparency. A schematic of this process is shown in Fig. 4.9, an example set of SEM images from a lift-out is shown in Fig. 4.10, and the specific lamellas containing the dendrites displayed in the results section are shown in Fig. 4.11a, b.

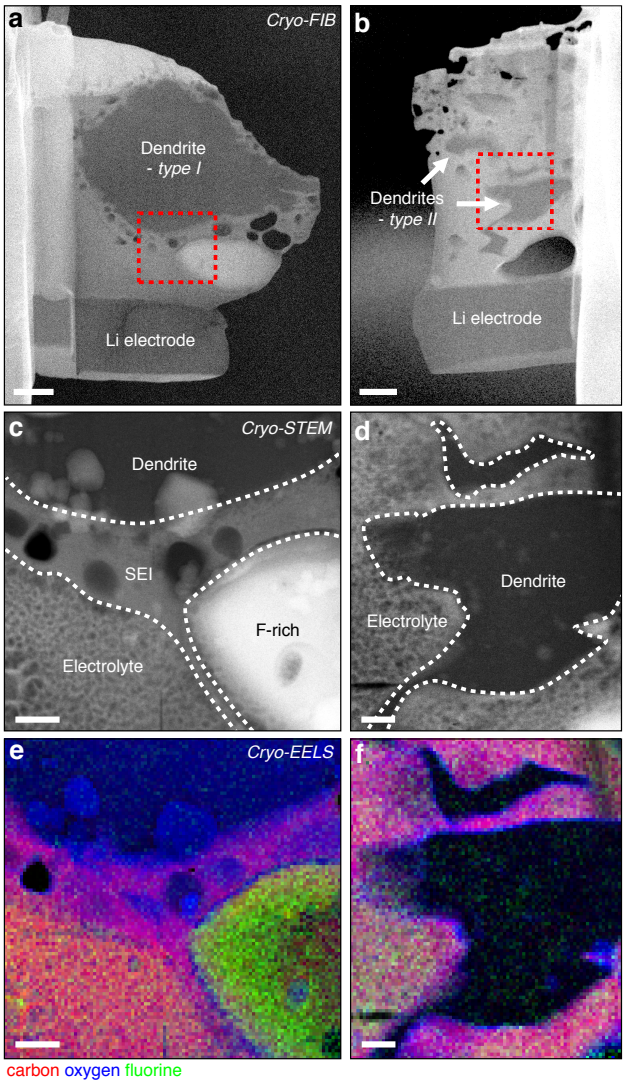

Figure 4.11 Structure and elemental composition of dendrites and their associated interphase layers in electron transparent lamellas. (a, b) Electron transparent lamellas of both dendrite types, produced by cryo-FIB lift-out. (c, d) An extended SEI layer was present on the type I dendrite, but not the type II, as revealed by HAADF cryo-STEM imaging. (e, f) EELS elemental maps showed the extended type I SEI was oxygen-rich, and the thin type II SEI contained oxygen, but no carbon. The type I dendrite had an appreciable oxygen content, while the type II did not. Fluorine-rich structures were often observed near both dendrite types. (a) and (b) scale bars, 1 µm, (c)-(f), 300 nm.

4.3.2.1 Dendrite SEI Layer Structure and Composition

High-angle annular dark-field (HAADF) cryo-STEM imaging of these lamellas immediately revealed an extended SEI layer on the type I dendrite, approximately 300

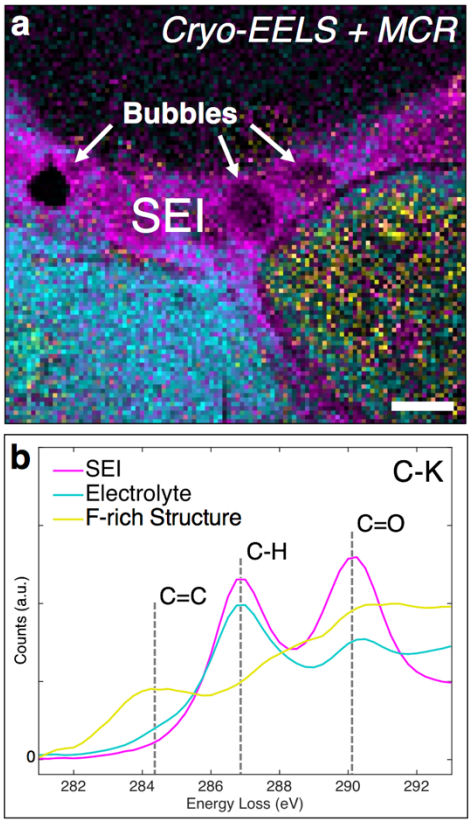

Figure 4.12 Carbon bonding analysis of the type I dendrite interphase. (a) Spatial variation of EELS carbon fine structure showed distinct carbon bonding environments present in the electrolyte, SEI layer, and F-rich structure. (b) The increased 290 eV carbonate C=O bond peak is consistent with a lithium ethylene dicarbonate SEI layer. The C=C bond peak below 285 eV may originate from ethylene gas, a byproduct of SEI formation, possibly bound to LiF in the F-rich structure and the source of the bubbles in the SEI. Scale bar, 300 nm.

to 500 nm thick, which was not present on the type II dendrite (Fig. 4.11c, d). The SEI layer on the anode in LMBs is commonly believed to be tens of nanometers thick [118], largely by analogy to what is known of the self-limiting SEI formed on the graphitic carbon anode used in lithium-ion batteries. Our results suggest that a soft, extended portion of the SEI is removed by washing during sample preparation for traditional characterization techniques, as suggested previously [9]. The remaining portion of the SEI observed by these techniques would then be a thin, compact layer. This is

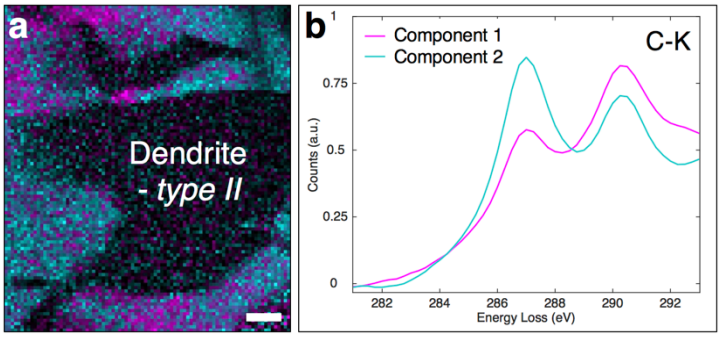

Figure 4.13 Bonding analysis of carbon near the type II dendrite. (a) Two carbon *K*-edge components were present in the electrolyte, but they were not highly localized along the dendrite surface as in the type I case. (b) The peaks occurred at the same energies, but with slightly different intensities, than the components near the type I dendrite. Scale bar, 300 nm.

significant, in part, because it means substantially more lithium is irreversibly lost to the SEI layer than previously thought.

To examine the elemental distribution and local bonding environment in the SEI layers and dendrites, we performed spectroscopic mapping using EELS. In the extended type I SEI we observed an increased concentration of oxygen and lithium compared to the electrolyte, essentially no fluorine, and a similar amount of carbon (Fig. 4.11e). While no extended type II SEI was observed by HAADF-STEM imaging, EELS revealed a thin carbon-free, lithium- and oxygen-rich layer on the surface of the type II dendrite, approximately 20 nm thick (Fig. 4.11f). Roughly spherical structures up to microns in size were frequently observed near both dendrite types (shown near the type I dendrite here - Fig. 4.11a, c) but rarely elsewhere in the sample, and these structures were fluorine-rich and also contained carbon, oxygen, and lithium (Fig. 4.11e).

By analyzing the C *K*-edge fine structure using multivariate curve resolution (MCR), we observe distinct carbon bonding environments in the electrolyte, SEI, and F-rich structure (Fig. 4.12a, b). The increased intensity of the 290 eV peak, from 1s to

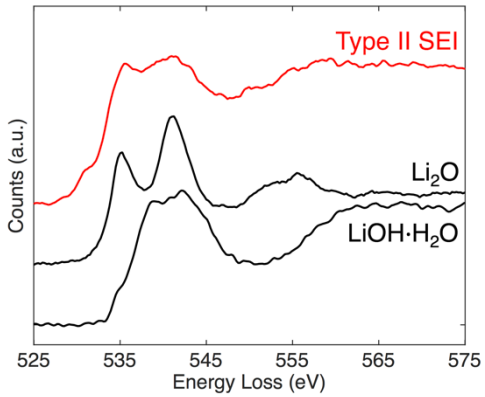

Figure 4.14 Comparison of the Type II dendrite SEI O-K edge with reference spectra. The O-K edge of the type II dendrite appeared to be consistent with a combination of lithium oxide and lithium hydroxide monohydrate. Spectra are offset vertically for clarity.

π* transitions at C=O bonds in carbonates [82], suggests a higher density of these bonds in the SEI than the electrolyte. This, along with the increased oxygen content, is consistent with evidence that the SEI consists largely of lithium ethylene dicarbonate (LEDC) in EC-based electrolytes [185,192,193]. Additionally, ethylene gas is produced during formation of LEDC from EC [185,192–194], which may explain the large bubbles observed in the SEI. The peak below 285 eV corresponds to 1s to π* transitions in C=C bonds [82], such as in ethylene. The correlation of the signals corresponding to fluorine and C=C bonds in the F-rich structure may indicate ethylene is bound to LiF here, the possibility of which has been discussed previously [195]. The C=C peak was not present near the type II dendrite, and no significant change in the C bonding environment was observed along the dendrite surface (Fig. 4.13). The ~287 eV peak is a transition from a 1s to 3p/σ^* hybrid state at C-H bonds [82], and is correspondingly reduced in the LEDC of the type I SEI compared to the electrolyte. While no carbon was present in the thin type II SEI, the O-*K* fine structure is consistent with a

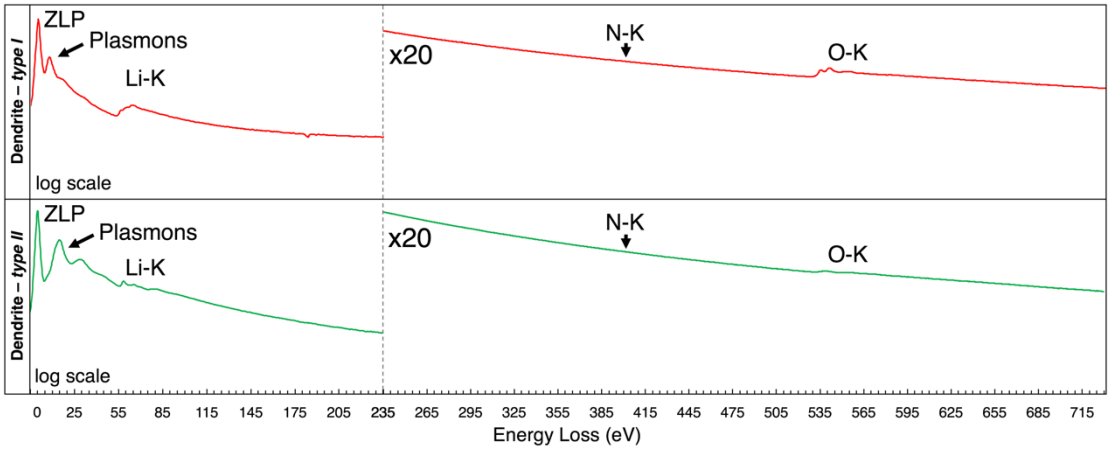

Figure 4.15 Full spectra recorded from the dendrites (intensities on a log scale). The spectra show clear differences in the plasmons and Li-K edges, as well as a large difference in oxygen content between the type I and type II dendrites. The small amount of oxygen on the type II dendrite is likely water molecules adsorbed on the surface of the sample in the microscope vacuum, which would typically react with materials such as lithium or sodium at room temperature. No nitrogen was present in either dendrite, confirming that no reaction with nitrogen in the air or liquid nitrogen had occurred.

combination of lithium oxide and hydroxide monohydrate (Fig. 4.14). Finally, even though we used an electron dose well below the damage threshold for carbonates of ~750 e^{-} $Å^{-2}$ [189], small bubbles in the electrolyte were observed after imaging, likely due to hydrogen liberated from solvent molecules due to beam exposure as discuss previously. These were unlike the larger SEI bubbles, which were inherent to the system and not induced by beam exposure.

4.3.2.2 Revealing Dendrite Compositions

Elemental analysis of the dendrite interiors by EELS showed the type I dendrite contained an appreciable quantity of oxygen, while the type II dendrite did not. No other edges between the Li-*K* at 55 eV and ~730 eV were present, including nitrogen, which rules out reactions with air or liquid nitrogen during specimen preparation and transfer (Fig. 4.15). The two dendrite types are, therefore, not only distinct in morphology, but

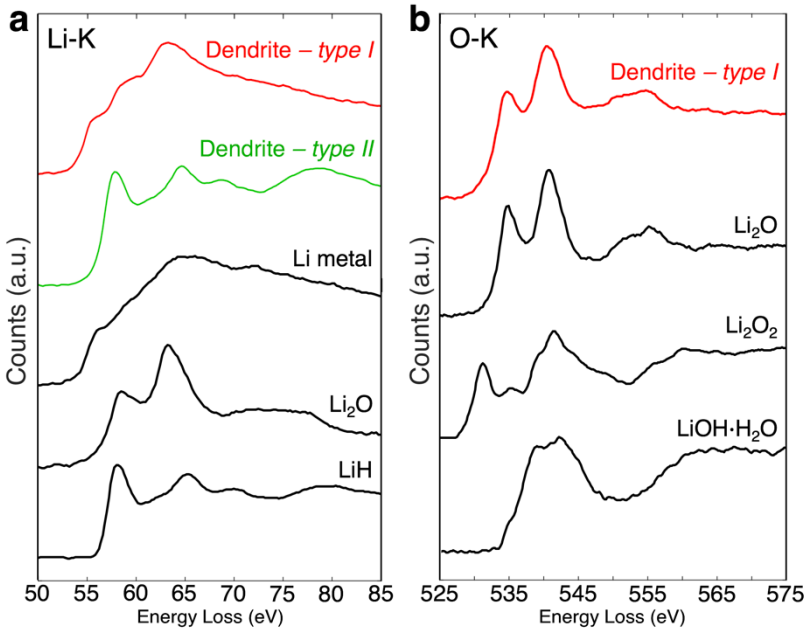

Figure 4.16 Comparison of EELS fine structure from dendrites and lithium reference materials. (a, b) Comparison of the dendrites' lithium and oxygen spectral fine structures with reference materials revealed the type I dendrite was composed of partially oxidized lithium metal, while the type II dendrite was uniform lithium hydride.

also in elemental composition. To understand changes in the local bonding, we investigated the Li-*K* and O-*K* fine structures (Fig. 4.16a, b). Comparison with reference spectra recorded on various lithium compounds revealed the type I dendrite was composed of lithium metal, partially oxidized to lithium oxide. The type II dendrite Li *K*-edge, however, was strikingly different than any combination of lithium metal, oxide, peroxide, or hydroxide reference spectra, and we unexpectedly found it corresponded to pure lithium hydride. While hydrogen gas is known to be prevalent in cycled lithium batteries [196], only small amounts of LiH have been observed on freshly exposed lithium brought into contact with organic electrolytes by FT-IR [197]. NMR studies have revealed appreciable quantities on metal oxide conversion cathodes in lithium-ion batteries, however [9]. LiH is metastable in electrolytes since it rapidly reacts with trace

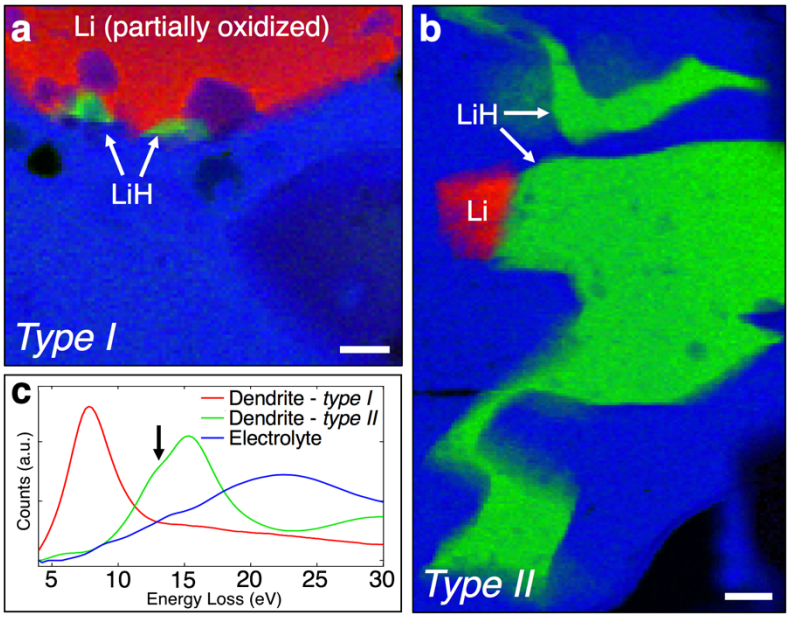

Figure 4.17 Dendrite compositional mapping by low-loss EELS. (a, b) Mapping of the unique lithium metal and hydride low-loss EELS spectra (c) revealed the type I dendrite was only slightly oxidized and had small regions of LiH at its surface, while the type II dendrite had a lithium particle at the tip. The hydrogen *K*-edge appears at ~13 eV in LiH, denoted by the arrow. Scale bars, 300 nm.

moisture and solvent molecules to form species such as LiOH and Li_2O [197]. On large LiH structures exposed to the electrolyte, however, these reactions may result in a thin passivating layer forming on the surface, stabilizing the material, which is consistent with the SEI observed on the type II dendrite.

In addition to core-loss spectroscopy of the dendrites, we examined the plasma resonances of the materials by simultaneously acquired low-loss EELS (Fig. 4.17a-c). Fig. 4.17c shows the plasmon peaks for the type I and type II dendrites, at 7.5 eV and 15 eV, respectively. The type I dendrite plasmon suggests the lithium is only partially oxidized. Pure or slightly oxidized lithium has a plasmon peak at 7.5 eV, but highly oxidized lithium forms additional resonances at 18 and 30 eV [60], which we did not observe. The shoulder at ~13 eV on the LiH spectrum, indicated by the arrow in Fig.

	Dendrite Type I	Dendrite Type II
Diameter	~1-10 μm	~100s of nm
Morphology	Low curvature	Tortuous
Electrode Contact Area	~10 μm^3	~0.1 μm^3
Composition	Lithium metal, slightly oxidized (Li_2O).	LiH
Distribution of Materials	Slightly oxidized lithium with small LiH regions on surface.	Uniform LiH. Pure/slightly oxidized Li particle on tip.
SEI Thickness	~300-500 nm	~20 nm
SEI Elements Detected	Li, C, O	Li, O
SEI Composition	Extended SEI consistent with lithium ethylene dicarbonate. Large bubbles within likely originate from ethylene gas.	Li_2O and $LiOH{\cdot}H_2O$

Table 4.2 Comparison of type I and II dendrite properties.

4.17c, provides additional evidence for the presence of hydrogen in the type II dendrite, due to the 13.6 eV H *K*-edge. Using the low-loss spectra, we mapped the spatial distribution of the partially oxidized lithium and lithium hydride compounds in the dendrites (Fig. 4.17a, b). The resulting maps show that, in addition to the materials that made up the bulk of the dendrites, small LiH regions were present on the surface of the type I dendrite, and a lithium particle was present on the tip of the type II dendrite. Table 4.2 lists a complete comparison of the dendrite characteristics and Figure 4.18 shows diagrams of the two dendrite types and their respective SEI layers.

4.4 Discussion

While it might be tempting to assume the hydrogen to produce these type II dendrites originates solely from the reduction of water impurities in the electrolyte, it was recently shown that decomposition of the electrolyte solvent molecules can produce many times

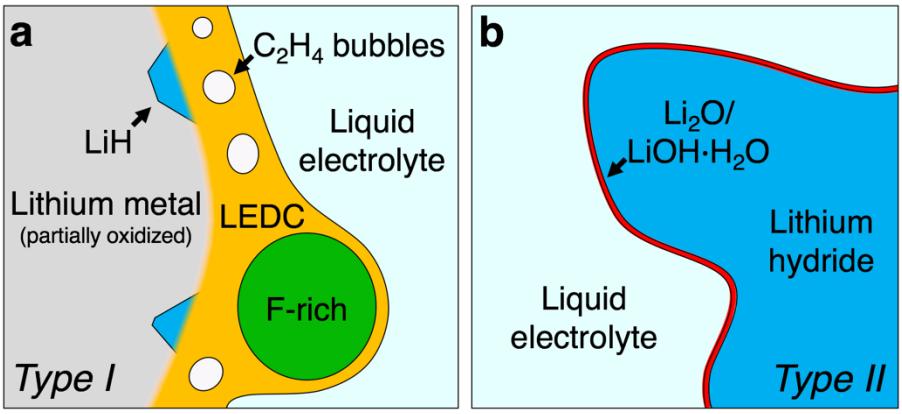

Figure 4.18 Schematic of both dendrite types and their corresponding SEI layers. (a) Type I dendrites consist of partially oxidized lithium metal with small LiH regions at the surface, and have an extended SEI layer consistent with lithium ethylene dicarbonate (LEDC) that contains bubbles likely from ethylene, a byproduct of the SEI formation. Large F-rich structures are often found near the dendrites. (b) Type II dendrites consist of uniform LiH and have a compact $Li_2O/LiOH{\bullet}H_2O$ SEI layer. Though not depicted, F-rich structures were also observed near type II dendrites.

more hydrogen than water impurities, even in electrolytes with water content up to twice that of ours. This hydrogen originates from a "cross-talk" mechanism where solvent molecules oxidized at the cathode are subsequently reduced at the anode, producing hydrogen [194]. By assuming a type II dendrite volume of ~300 μm^3 as determined by our cryo-FIB measurements, a back-of-the-envelope calculation reveals that the maximum density of these dendrites that could form in our cells with water as the sole source of hydrogen in our electrolyte (<10 ppm H_2O) should be roughly an order or magnitude lower than what is actually observed. This suggests a cross-talk mechanism may also be contributing hydrogen. The rate of hydrogen production by the cross-talk mechanism is a strong function of cell voltage [194], so full cell batteries using higher voltage cathode materials would result in production of significantly larger quantities of hydrogen. This would exacerbate the problem of LiH dendrite formation in these cells, especially when paired with a 5 V-class high-voltage cathode material designed

to improve energy density. Potential pathways to hydrogen production exist for any H-containing electrolyte as well, and therefore all LMB batteries utilizing traditional organic electrolytes are likely to suffer from LiH dendrite formation and the associated capacity fade.

Our results therefore suggest that preventing formation of type II dendrites may hinge on a careful choice of solvents and salts to eliminate hydrogen-containing species in the electrolyte and to form interphase layers to protect the anode surface. One way to achieve these goals would be to replace hydrogen in the solvent molecules with other elements in order to generate alternative species in the electrolyte. For example, we hypothesize that a properly chosen material would result in a H-deprived and F-rich environment where sacrificial, low-stability window fluorinated components are preferentially reduced at the anode and oxidized at the cathode relative to carbonate solvents, resulting in F-rich species in the electrolyte. This would both starve the system of hydrogen and promote formation of a beneficial LiF-rich barrier layer on the anode surface [92,198], stunting the growth of LiH dendrites and reducing capacity fade. While recent studies using so-called high-concentration full-fluoride (HFF) electrolytes are consistent with our predictions [199], the high fluorine-donating salt content of the HFF electrolytes as currently configured is impractical and expensive. There is therefore room to explore alternative materials to achieve the above goals with more normal salt contents and a practical electrolyte cost.

As a test of our above hypothesis, we performed cryo-FIB, cryo-STEM EELS, and electrochemical experiments on cells prepared with a full-fluoride electrolyte using a lower salt concentration, fluoroethylene carbonate (FEC) with 2M $LiPF_6$, and the results

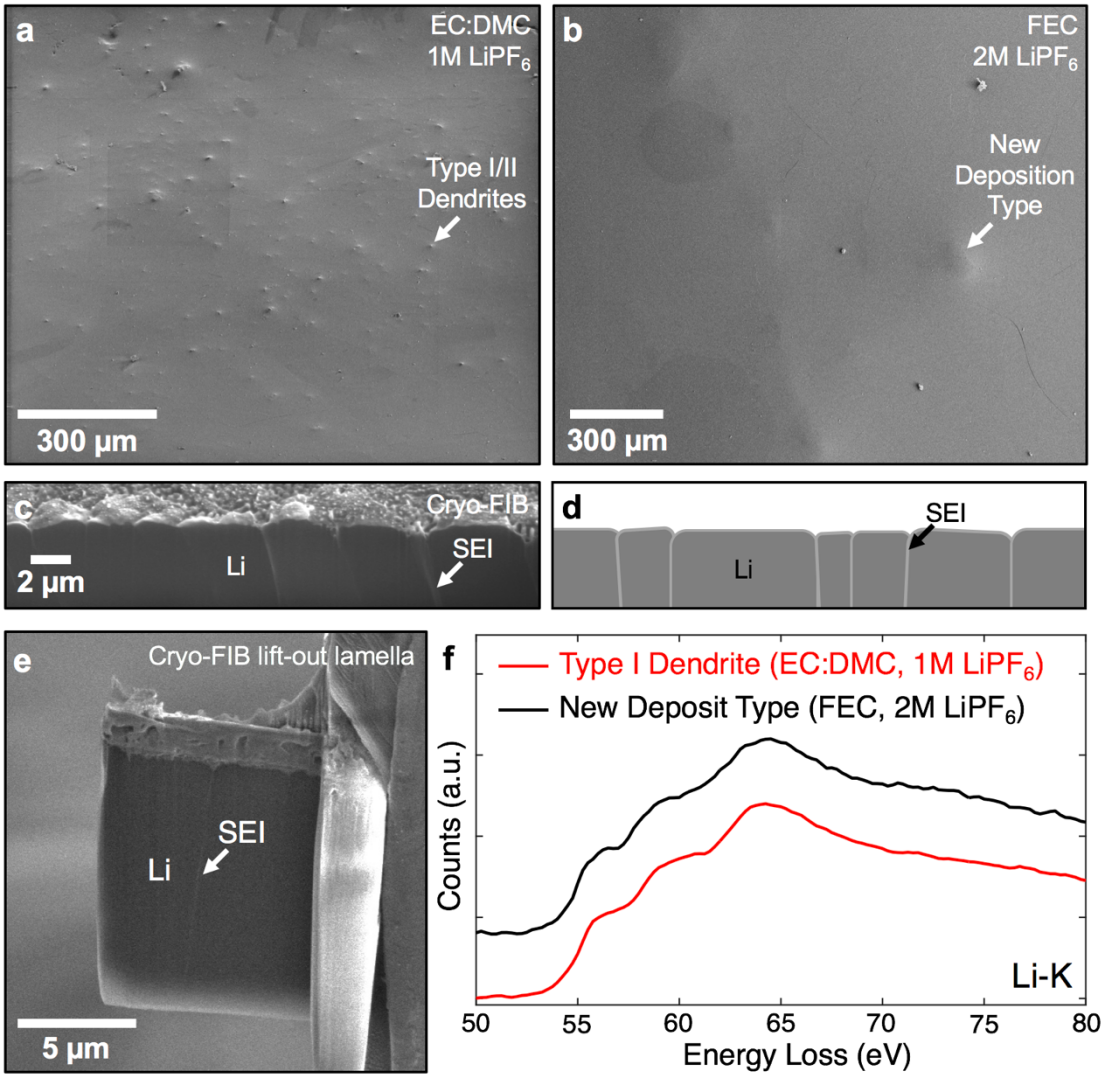

Figure 4.19 Cryo-FIB and cryo-STEM EELS comparing lithium deposition in cells using traditional and full-fluoride electrolytes. (a,b) Cryo-FIB revealed that the dendrite density is significantly lower for the full-fluoride FEC electrolyte than with the traditional EC:DMC electrolyte. In the former case, nearly no LiH dendrites are present, and the lithium deposition is modified as well, forming broad localized depositions. (c,d) Cross-sections of these deposits revealed they are composed of many smaller "blocks" in contact, separated by SEI layers. (e) A lamella of this new type of deposition was prepared by cryo-FIB lift-out, and (f) cryo-STEM EELS of the Li *K*-edge of the material revealed that it is composed of partially oxidized lithium metal, as the type I dendrite in the traditional electrolyte was.

are shown in Figure 4.19 and Figure 4.20. We found this fluorinated electrolyte significantly suppressed formation of LiH dendrites, as expected, and additionally

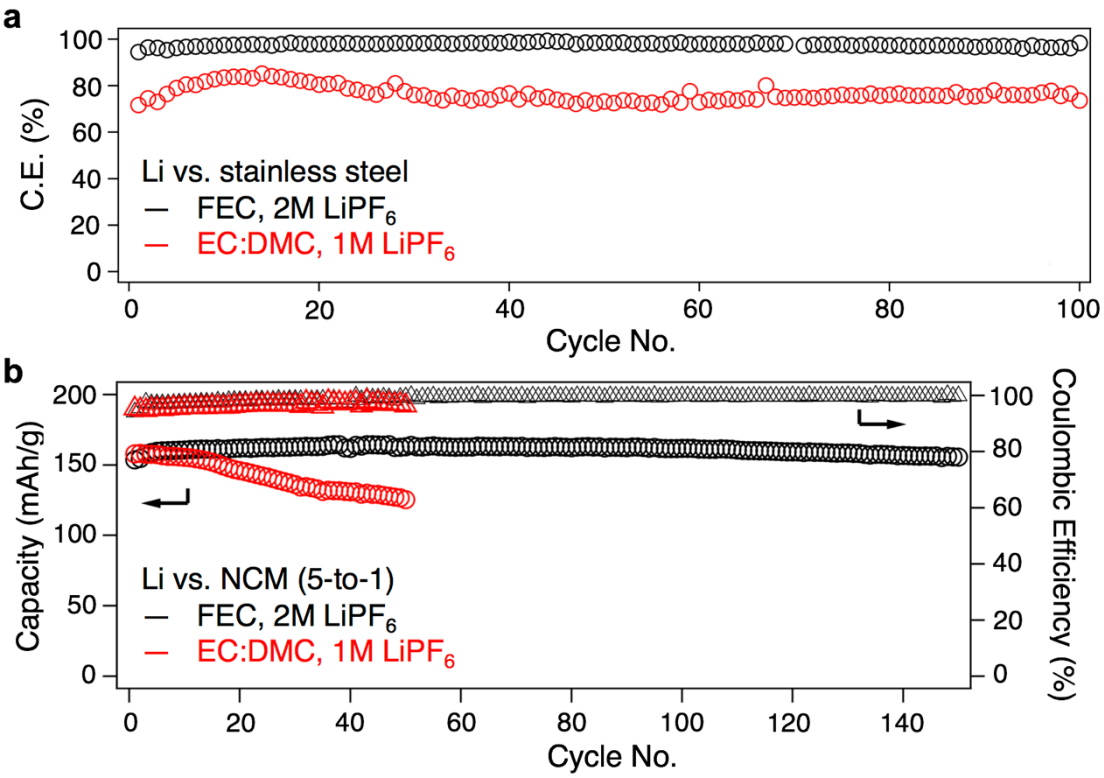

Figure 4.20 Electrochemical results comparing lithium deposition in cells using traditional and full-fluoride electrolytes. (a) Coulombic efficiency measured in a lithium vs. stainless steel setup using a constant current density of 1 mA cm^{-2} and capacity of 1 mAh cm^{-2} was significantly improved for the full-fluoride electrolyte compared to the traditional electrolyte. (b) Cycling of a full cell comprising a lean lithium anode (50μm) and a nickel manganese cobalt oxide (NCM) cathode (2 mAh cm^{-2}) with the full-fluoride electrolyte resulted in a significant decrease in capacity fade and improved coulombic efficiency over the traditional electrolyte. The discharge capacity is plotted on the left-axis, while the coulombic efficiency is on the right-axis. The operating voltage range was 4.3V to 3V. In all figures, the red lines and symbols represent results for the EC:DMC, 1M $LiPF_6$ electrolyte, while the black are for FEC, 2M $LiPF_6$.

greatly altered the lithium deposition. Localized structures were still present, but rather than "type I" dendrites the deposition was much broader, with an inner structure consisting of many smaller "blocks" separated by SEI layers containing C, O, and F. These blocks were composed of partially oxidized lithium, as with the type I dendrites, confirmed by cryo-STEM EELS of the structures prepared by cryo-FIB lift-out. The

electrochemical performance was correspondingly enhanced, with higher coulombic efficiency and significantly reduced capacity fade in the full-fluoride electrolyte cells, as shown in both lithium vs. stainless steel and full cell batteries using a nickel manganese cobalt oxide (NCM) cathode. While this demonstrates the feasibility of dendrite suppression and improved battery performance by introduction of fluorinated electrolytes, these concepts outline above could be further developed by integration of the alternative electrolyte species into cross-linkable structures such as those recently reported [200]. This would result in a H-deprived and halide-rich electrolyte environment that simultaneously forms a lithium halide-rich SEI and elastic interphases that are able to flex to accommodate volume change of the Li anode, thus providing protection against both LiH dendrites and traditional lithium metal dendrites.

It is also interesting to note that LiH spectra have been measured by a variety of techniques previously, not all in agreement [201–203]. The material's moisture sensitivity may explain the disagreement. While the previous work took precautions to avoid air exposure, such as cleaving the LiH in vacuum [201] or transferring it to the microscope in an argon bag [202], reactions with small amounts of contaminants could still occur at room temperature. Accurate spectra could be obtained either by measuring a bulk sample, as the passivating layer would enable the majority of the material to remain unreacted, or by maintaining the sample at cryogenic temperatures, since reactions with contaminants would be essentially eliminated. As expected, the spectra from samples measured in bulk or at cryogenic temperatures are in agreement with each other [201,203] and with our data. The difficulty of characterizing unaltered LiH may be one reason why LiH dendrites have not been observed before, and is an important

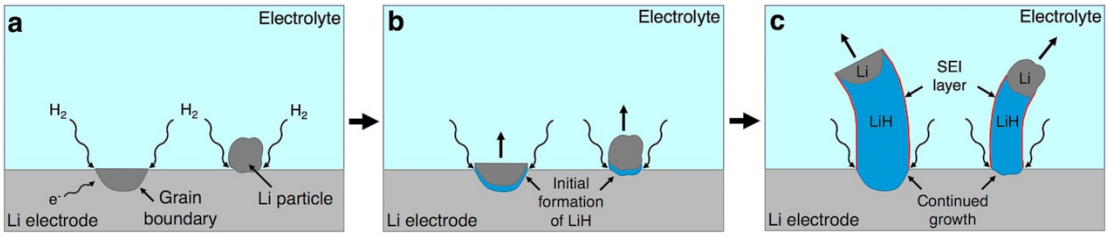

Figure 4.21 Schematic of proposed root growth of type II dendrites. (a) Hydrogen present in the electrolyte diffuses into grain boundaries at the electrode surface or a particle-electrode interface during charging. (b) Lithium hydride forms at these boundaries and pushes the initial lithium section upwards, creating the lithium particle observed on the type II dendrite tip. (c) Growth continues as more material diffuses into the dendrite-electrode interface.

example of how cryogenic techniques like cryo-FIB lift-out and cryo-STEM enable accurate characterization of systems with reactive materials as well as solid-liquid interfaces.

The lithium particle on the tip and uniformity of the LiH within the type II dendrites, as well as their aspect ratio, suggests a root or tip growth mode. Additionally, hydrogen is the smallest gas molecule present in the electrolyte during cycling [194,196], and grain boundaries have been shown to increase hydrogen diffusion through some metals [204]. If this occurs at the electrode surface, it may explain the mechanism behind the selective reactions needed to produce uniform LiH dendrites. Hydrogen and lithium ions could selectively penetrate into an electrode grain boundary or interface between a lithium particle and the electrode and initiate LiH formation. The volume expansion from formation of the new material would then force this particle or section away from the electrode surface, leading to the observed lithium particle on the dendrite tip (Fig. 4.17b). Growth would then likely proceed mainly at the base of the dendrite by continued diffusion into the dendrite-electrode interface, since the poor electrical conductivity of LiH [61] would limit the extent of the reaction elsewhere on the dendrite.

A schematic of this proposed process is shown in Figure 4.21. While formation of LiH is reversible [9], its low electrical conductivity means the reverse reaction would also likely only occur at the base. Furthermore, LiH is significantly more brittle than lithium metal [205]. These facts, combined with the low electrode contact area of the type II dendrites compared to the type I dendrites, suggest that type II dendrites become disconnected from the electrode more easily during cycling than type I dendrites. Since the total volume and number of both dendrite types is comparable, type II dendrites may, therefore, contribute disproportionately to capacity fade due to orphaned or disconnected lithium. Additionally, while the thickness of the type I SEI layer means it contributes more to loss of lithium material than previously thought, we estimate an order of magnitude more lithium is contained within the type II dendrites than the type I SEI layers. Minimizing the formation of LiH dendrites is therefore critical to improving the longevity of LMBs.

4.5 Conclusion

Growth of dendrites in lithium metal batteries is currently considered only a physical deposition process [33] resulting in lithium metal, therefore providing no understanding of the formation of dendrites composed of other lithium compounds. It is apparent, however, that such considerations are necessary if dendrite formation is to be fully understood. While LiH dendrites have not been accounted for in previous growth models or observed by other characterization techniques, their contribution to capacity fade could be significant. The findings presented here will help reduce capacity fade in LMBs by advancing our understanding of dendrite formation processes in these

systems. Additionally, they demonstrate the unique ability cryo-FIB and cryo-STEM techniques provide to generate new insights about processes at solid-liquid interfaces by directly probing the structure and composition of unaltered reactive materials and intact interfaces at the nanoscale.

CHAPTER 5

CONCLUSION

In the work presented here, we developed cryogenic electron microscopy techniques to allow the structure and composition of intact solid-liquid interfaces to be characterized down to the nanoscale, and these techniques were applied to study processes occuring at anode-electrolyte interfaces in lithium metal batteries. In order to establish the importance of this research, a brief review of battery operating principles was provided, as well as a historical overview of the events that led to lithium metal batteries. The technique that provides us with the highest-resolution compositional information is electron energy-loss spectroscopy (EELS), and we therefore also summarized the physics behind the collective valence and single core-level electron excitations that enabled us to perform compositional and bonding environment analyses in this work. We additionally described some specific challenges associated with measuring these signals in materials present in batteries. Finally, the physics of vitrification, or conversion of a liquid to an amorphous ice by rapid freezing, was outlined, as well as techniques to achieve vitrification, and previous applications of cryogenic transmission electron microscopy (cryo-TEM) to biological specimens.

In Chapter 2, we described focused ion beam/scanning electron microscopy (cryo-FIB/SEM) techniques for characterizing intact interfacial layers down to tens of nanometers thick on electrodes in devices. We demonstrated how cryogenic temperatures allow clean transfers and milling of reactive materials, and showed an example where this allowed the native structure and elemental composition of deposited lithium to be determined. In addition, we discussed milling and characterization of interfacial layers at solid-liquid interfaces in devices with the liquids intact in detail, including factors that influence the achievable resolution, examples for potential applications in batteries, and future developments that could enhance the capabilities of

cryo-FIB/SEM.

In Chapter 3, we described and demonstrated a cryo-FIB lift-out technique that enables site-specific localization, extraction, and preparation of electron-transparent cross sections of solid-liquid interfaces with the liquids intact for high-resolution cryo-scanning transmission electron microscopy (cryo-STEM) characterization. The required instrumentation and procedures were discussed thoroughly. Methods for localizing subsurface features of interest were described, and Monte Carlo simulations were performed to establish their feasibility. A model system of iron (oxy-, hydr-)oxide crystals grown in silica hydrogel was used to demonstrate these localization and preparation capabilities by preparing electron transparent cross-sectional lamellas of the hydrogel material containing iron (oxy-, hydr-)oxide crystals. These samples were subsequently transferred to the cryo-scanning transmission electron microscope (cryo-STEM), where nanoscale high-angle annular dark-field (HAADF) cryo-STEM imaging of the nanocrystal structure was performed, as well as energy dispersive X-ray (EDX) spectroscopy to reveal the elemental composition of the hydrogen and particles, and EELS to provide bonding information.

Finally, in Chapter 4, we applied all of these techniques to study anode-electrolyte interfaces in lithium metal battery (LMB) coin cells. Cryo-FIB milling and imaging were performed on the interfaces, revealing the presense of two morphologically distinct dendritic structures present on the electrode surface. Serial milling and imaging allowed the full three-dimensional structure of these dendrites to reconstructed, which enabled their total volume and electrode contact areas to be determined. Cryo-FIB lift-out was then utilized to prepare cross sections of each type of dendrite-electrolyte interface for analytical cryo-STEM characterization. HAADF cryo-STEM imaging revealed that one dendrite type had an extended solid-electrolyte interphase (SEI) layer on its surface, around 400 nm thick, while the other did not. In addition, analysis of the carbon *K*-edge

EELS fine structure the near the dendrite-electrolyte interface allowed us to show that the material in this extended SEI was consistent with lithium ethylene dicarbonate, and that the byproduct of the reaction to form this material, ethylene gas, may be binding to lithium fluoride in nearby structures. Core-loss EELS fine structure analysis was also applied to the dendrites, in addition to plasmon mapping, which revealed that one dendrite type was composed of slightly oxidized lithium metal, while the other was composed uniformly of lithium hydride, which had not been observed before. The small eletrode-contact areas of these lithium hydride dendrites combined with their physical and electrical properties suggests that they may become disconnected from the electrode during cycling more easily than lithium metal dendrites. With roughly equal numbers and volumes to the lithium metal dendrites, these dendrites could therefore contribute disproportionately to the significant capacity fade observed in LMBs.

Our findings also let us propose potential means to avoid formation of these detrimental lithium hydride dendrites. When a fluorine atom is substituted for a hdyrogen atom on one of the electrolyte solvent molecules used for this study, calculations have shown that it is removed preferentially over the hydrogen, both forming a barrier layer of lithium fluoride on the electrode surface and inhibiting production of hydrogen in the cell. We therefore proposed that use of a of full-fluoride electrolyte solvent of this type could suppress the formation of lithium hydride dendrites, and carried out electrochemical, cryo-FIB/SEM, and cryo-STEM experiments to test this idea. Cryo-FIB/SEM immediately revealed that the density of dendrites in the full-fluoride cells was significantly lower than in the traditional electrolyte. Much broader localized deposits were still present, however, and cross-sectional milling and imaging of these structures revealed that they consisted of "blocks" of material separated by thin SEI layers. Cryo-FIB lift-out was then used to prepare a cross section of these deposited structures for cryo-STEM, where we

discovered that the deposited material was slightly oxidized lithium metal, not lithium hydride. In addition, the electrochemical performance of these full-fluoride cells was significantly improved. Lithium versus stainless steel cells achieved much higher coulombic efficiency with the full-fluoride electrolyte than with the traditional electrolyte, and full cells using a nickle manganese cobalt oxide cathode paired with the full-fluoride electrolyte maintained their capacity for over 140 cycles, while the cells paired with the traditional electrolyte experienced significant capacity fade by 50 cycles.

The cryogenic electron microscopy techniques described here therefore allowed us to discover a new type of dendrite present on LMB anodes, which likely gets washed away during the washing and drying preparation steps for traditional techniques, and propose initial pathways towards avoiding lithium hydride dendrite formation, and additional experiments supported these ideas. Since these dendrites may contribute disproportionately to the rapid capacity fade observed in LMBs compared to lithium metal dendrites, their discovery and suppression may be critical for improving the performance of these batteries.

Cryo-FIB/SEM, cryo-FIB liftout, and cryo-STEM techniques have thus been shown to be valueable tools for characterizing intact solid-liquid interfaces and reactive materials down to the nanoscale. These techniques are capable of providing morphological information about structures present at these interfaces, as well as high-resolution structural and bonding information. With solid-liquid interfaces playing an important role in a diverse set of systems, these techniques are poised to make a significant contribution to a wide range of fields.

References

1. Maps and Data. *U.S. Department of Energy, Office of Energy Efficiency & Renewable Energy - Alternative Fuels Data Center* (2018). Available at: https://www.afdc.energy.gov/data/categories/afvs-and-hevs.
2. Nathan S. Lewis. Research opportunities to advance solar energy utilization. *Science (80-.).* **351** (6271), aad1920 (2016).
3. Dunn, B., Kamath, H. & Tarascon, J.-M. Electrical Energy Storage for the Grid: A Battery of Choices. *Science (80-.).* **334** 928–935 (2011).
4. Scrosati, B. History of lithium batteries. *J. Solid State Electrochem.* **15** (7), 1623–1630 (2011).
5. Tarascon, J.-M. & Armand, M. Issues and challenges facing rechargeable lithium batteries. *Nature* **414** (November), 359–367 (2001).
6. Goldstein, J. *et al. Scanning Electron Microscopy and X-Ray Microanalysis*. (Springer Science + Business Media, LLC, 2003). doi:DOI 10.1007/978-1-4615-0215-9
7. *Introduction To Focused Ion Beams*. (Springer, 2005). doi:https://doi.org/10.1007/b101190
8. Muller, D. A. *et al.* Atomic-scale chemical imaging of composition and bonding by aberration-corrected microscopy. *Science* **319** (5866), 1073–1076 (2008).
9. Hu, Y.-Y. *et al.* Origin of additional capacities in metal oxide lithium-ion battery electrodes. *Nat. Mater.* **12** 1130 (2013).
10. Dubochet, J. *et al.* Cryo-electron microscopy of vitrified specimens. *Q. Rev. Biophys.* **21** (2), 129–228 (1988).

11. Bard, A. J. & Faulkner, L. R. *Electrochemical Methods: Fundamentals and Applications*. (John Wiley & Sons, Inc., 2001).

12. Goodenough, J. B. & Park, K. S. The Li-ion rechargeable battery: A perspective. *J. Am. Chem. Soc.* **135** (4), 1167–1176 (2013).

13. Volta, A. On the Electricity Excited by the Mere Contact of Conducting Substances of Different Kinds. In a Letter from Mr. Alexander Volta, F. R. S. Professor of Natural Philosophy in the University of Pavia, to the Rt. Hon. Sir Joseph Banks, Bart. K. B. P. R. S. *Philos. Trans. R. Soc. London* **90** 403–431 (1800).

14. Whittingham, M. S. Electrical energy storage and intercalation chemistry. *Science (80-.).* **192** (4244), 1126–1127 (1976).

15. Mohri, M. *et al.* Rechargeable lithium battery based on pyrolytic carbon as a negative electrode. *J. Power Sources* **26** 545–551 (1989).

16. Fong, R., von Sacken, U. & Dahn, J. R. Studies of Lithium Intercalation into Carbons Using Nonaqueous Electrochemical Cells. *J. Electrochem. Soc.* **137** (7), 2009–2013 (1990).

17. Mizushima, K., Jones, P. C., Wiseman, P. J. & Goodenough, J. B. LixCoO2 (0<x<-1): A new cathode material for batteries of high energy density. *Mater. Res. Bull.* **15** (6), 783–789 (1980).

18. Nagaura, T. & Tozawa, K. Lithium ion rechargeable battery. *Prog. Batter. Sol. Cells* **9** 209 (1990).

19. Fact #939: August 22, 2016 All-Electric Vehicle Ranges Can Exceed Those of Some Gasoline Vehicles. *Transportation Fact of the Week. U.S. Department of*

Energy, Vehicle Technology Office. (2016). Available at: https://www.energy.gov/eere/vehicles/fact-939-august-22-2016-all-electric-vehicle-ranges-can-exceed-those-some-gasoline.

20. Bruce, P. G., Freunberger, S. A., Hardwick, L. J. & Tarascon, J.-M. Li-O_2 and Li-S batteries with high energy storage. *Nat. Mater.* **11** (December 2011), 19–29 (2012).

21. Obrovac, M. N. & Chevrier, V. L. Alloy negative electrodes for Li-ion batteries. *Chem. Rev.* **114** (23), 11444–11502 (2014).

22. Bruce, P. G., Scrosati, B. & Tarascon, J.-M. Nanomaterials for rechargeable lithium batteries. *Angew. Chem. Int. Ed. Engl.* **47** (16), 2930–46 (2008).

23. Wei Seh, Z. *et al.* Sulphur-TiO2 yolk-shell nanoarchitecture with internal void space for long-cycle lithium-sulphur batteries. *Nat. Commun.* **4** 1331 (2013).

24. Zhou, W., Yu, Y., Chen, H., Disalvo, F. J. & Abruña, H. D. Yolk-shell structure of polyaniline-coated sulfur for lithium-sulfur batteries. *J. Am. Chem. Soc.* **135** (44), 16736–16743 (2013).

25. Goodenough, J. B. & Kim, Y. Challenges for Rechargeable Li Batteries. *Chem. Mater.* **22** 587–603 (2010).

26. Manthiram, A., Yu, X. & Wang, S. Lithium battery chemistries enabled by solid-state electrolytes. *Nat. Rev. Mater.* **2** (4), 16103 (2017).

27. Xu, W. *et al.* Lithium metal anodes for rechargeable batteries. *Energy Environ. Sci.* **7** 513 (2014).

28. Aricò, a. S., Bruce, P., Scrosati, B., Tarascon, J. M. & Van Schalkwijk, W. Nanostructured materials for advanced energy conversion and storage devices.

Nat. Mater. **4** (5), 366–377 (2005).

29. Lin, D., Liu, Y. & Cui, Y. Reviving the lithium metal anode for high-energy batteries. *Nat. Nanotechnol.* **12** (3), 194–206 (2017).

30. Xu, K. & von Cresce, A. Interfacing electrolytes with electrodes in Li ion batteries. *J. Mater. Chem.* **21** (27), 9849 (2011).

31. Tikekar, M. D., Choudhury, S., Tu, Z. & Archer, L. A. Design principles for electrolytes and interfaces for stable lithium-metal batteries. *Nat. Energy* **1** (9), 16114 (2016).

32. Cohen, Y. S., Cohen, Y. & Aurbach, D. Micromorphological Studies of Lithium Electrodes in Alkyl Carbonate Solutions Using in Situ Atomic Force Microscopy. *J. Phys. Chem. B* **104** (51), 12282–12291 (2000).

33. Li, Z., Huang, J., Yann Liaw, B., Metzler, V. & Zhang, J. A review of lithium deposition in lithium-ion and lithium metal secondary batteries. *J. Power Sources* **254** 168–182 (2014).

34. Xin-Bing, C. *et al.* A Review of Solid Electrolyte Interphases on Lithium Metal Anode. *Adv. Sci.* **3** (3), 1500213 (2015).

35. Zaera, F. Probing Liquid/Solid Interfaces at the Molecular Level. *Chem. Rev.* **112** 2920–2986 (2012).

36. Kanamura, K., Tamura, H. & Takehara, Z. XPS analysis of a lithium surface immersed in propylene carbonate solution containing various salts. *J. Electroanal. Chem.* **333** (1–2), 127–142 (1992).

37. Edström, K., Herstedt, M. & Abraham, D. P. A new look at the solid electrolyte interphase on graphite anodes in Li-ion batteries. *J. Power Sources* **153** (2), 380–

384 (2006).

38. Peled, E. *et al.* Composition, depth profiles and lateral distribution of materials in the SEI built on HOPG-TOF SIMS and XPS studies. *J. Power Sources* **97–98** 52–57 (2001).

39. Wang, F. *et al.* Chemical Distribution and Bonding of Lithium in Intercalated Graphite: Identification with Optimized Electron Energy Loss Spectroscopy. *ACS Nano* **5** (2), 1190–1197 (2011).

40. Sacci, R. L. *et al.* Nanoscale imaging of fundamental li battery chemistry: solid-electrolyte interphase formation and preferential growth of lithium metal nanoclusters. *Nano Lett.* **15** (3), 2011–8 (2015).

41. Holtz, M. E., Yu, Y., Gao, J., Abruña, H. D. & Muller, D. A. *In Situ* Electron Energy-Loss Spectroscopy in Liquids. *Microsc. Microanal.* **19** 1027–1035 (2013).

42. Holtz, M. E. *et al.* Nanoscale imaging of lithium ion distribution during in situ operation of battery electrode and electrolyte. *Nano Lett.* **14** (3), 1453–1459 (2014).

43. Sacci, R. L. *et al.* Direct visualization of initial SEI morphology and growth kinetics during lithium deposition by in situ electrochemical transmission electron microscopy. *Chem. Commun.* **50** 2104 (2014).

44. Unocic, R. R. *et al.* Direct Visualization of Solid Electrolyte Interphase Formation in Lithium-Ion Batteries with *In Situ* Electrochemical Transmission Electron Microscopy. *Microsc. Microanal.* **20** 1029–1037 (2014).

45. Unocic, R. R. *et al.* Probing battery chemistry with liquid cell electron energy

loss spectroscopy. *Chem. Commun.* **51** (91), 16377–16380 (2015).

46. Ruska, E. The development of the electron microscope and of electron microscopy. *Biosci. Rep.* **7** (8), 607–629 (1987).

47. Muller, D. A. Structure and bonding at the atomic scale by scanning transmission electron microscopy. *Nat. Mater.* **8** (4), 263–270 (2009).

48. Scherzer, O. Über einige Fehler von Elektronenlinsen. *Zeitschrift für Phys.* **101** (9), 593–603 (1936).

49. Scherzer, O. Sphaerische und chromatische Korrektur von Elektronenlinsen. *Optik (Stuttg).* **2** 114–132 (1947).

50. Rose, H. H. Historical aspects of aberration correction. *J. Electron Microsc. (Tokyo).* **58** (3), 77–85 (2009).

51. Hawkes, P. W. Aberration correction past and present. *Philos. Trans. R. Soc. A* **367** 3637–3664 (2009).

52. Haider, M., Braunshausen, G. & Schwan, E. Correction of the spherical aberration of a 200 kV TEM by means of a hexapole corrector. *Optik (Stuttg).* **99** 167–179 (1995).

53. Uhlemann, S. & Haider, M. Residual wave aberrations in the first spherical aberration corrected transmission electron microscope. *Ultramicroscopy* **72** (3), 109–119 (1998).

54. Krivanek, O., Dellby, N., Spence, A. J., Camps, R. A. & Brown, L. M. Aberration correction in the STEM. in *Proceedings of the Institute of Physics Electron Microscopy and Analysis Group Conference* (ed. Rodenburg, J. M.) 35–40 (Institute of Physics Publishing, 1997).

55. Krivanek, O., Dellby, N., Spence, A. J., Camps, R. A. & Brown, L. M. On-line aberration measurement and correction in STEM. *Microsc. Microanal.* **3** (Suppl. 2), 1171–1172 (1997).

56. Egerton, R. F. *Electron Energy-Loss Spectroscopy in the Electron Microscope*. (Springer Science + Business Media, LLC, 2011).

57. *Transmission Electron Microscopy - Diffraction, Imaging, and Spectrometry*. (Springer International Publishing Switzerland, 2016). doi:10.1007/978-3-319-26651-0

58. Lagos, M. J., Trügler, A., Hohenester, U. & Batson, P. E. Mapping vibrational surface and bulk modes in a single nanocube. *Nature* **543** (7646), 529–532 (2017).

59. Reimer, L. & Kohl, H. *Transmission Electron Microscopy Physics of Image Formation*. *Springer Series in Optical Sciences* **36** (Springer Science + Business Media, LLC, 2008).

60. Liu, D.-R. & Williams, D. B. The electron-energy-loss spectrum of lithium metal. *Philos. Mag. Part B* **53** (6), L123–L128 (1986).

61. Islam, A. K. M. A. Lighter Alkali Hydride and Deuteride. *Phys. Stat. Sol.* **180** 9–57 (1993).

62. Muller, D. A. & Silcox, J. Delocalization in inelastic scattering. *Ultramicroscopy* **59** (1–4), 195–213 (1995).

63. Laffont, L. *et al.* Study of the $LiFePO_4/FePO_4$ Two-Phase System by High-Resolution Electron Energy Loss Spectroscopy. *Chem. Mater.* **18** 5520–5529 (2006).

64. Inokuti, M. Inelastic collisions of fast charged particles with atoms and molecules-The bethe theory revisited. *Rev. Mod. Phys.* **43** (3), 297–347 (1971).

65. Bohr, N. II. On the theory of the decrease of velocity of moving electrified particles on passing through matter. *London, Edinburgh, Dublin Philos. Mag. J. Sci.* **25** (145), 10–31 (1913).

66. Bohr, N. LX. On the decrease of velocity of swiftly moving electrified particles in passing through matter. *London, Edinburgh, Dublin Philos. Mag. J. Sci.* **30** (178), 581–612 (1915).

67. Bethe, H. Zur Theorie des Durchgangs schneller Korpuskularstrahlen durch Materie. *Ann. Phys.* **397** (3), 325–400 (1930).

68. Parrat, L. G. Electronic Band Structure of Solids by X-Ray Spectroscopy. *Rev. Mod. Phys.* **31** (3), 616–645 (1959).

69. Bethe, H. Bremsformel für Elektronen relativistischer Geschwindigkeit. *Zeitschrift für Phys.* **76** (5), 293–299 (1932).

70. Rez, P. Inner Shell Spectroscopy: An Atomic View. *Ultramicroscopy* **28** 16–23 (1989).

71. Leapman, R. D., Fejes, P. L. & Silcox, J. Orientation dependence of core edges from anisotropic materials determined by inelastic scattering of fast electrons. *Phys. Rev. B* **28** (5), 2361–2373 (1983).

72. Rez, P. & Muller, D. A. The Theory and Interpretation of Electron Energy Loss Near-Edge Fine Structure. *Annu. Rev. Mater. Res* **38** 535–58 (2008).

73. Muller, D. A. Why changes in bond lengths and cohesion lead to core-level shifts in metals, and consequences for the spatial difference method. *Ultramicroscopy*

78 (1), 163–174 (1999).

74. Mundy, J. A. *et al.* Visualizing the interfacial evolution from charge compensation to metallic screening across the manganite metal–insulator transition. *Nat Commun* **5** (2014).

75. Jiang, N. & Spence, J. C. H. Core-hole effects on electron energy-loss spectroscopy of Li2O. *Phys. Rev. B* **69** 115112 (2004).

76. Gao, S.-P., Pickard, C. J., Payne, M. C., Zhu, J. & Yuan, J. Theory of core-hole effects in 1*s* core-level spectroscopy of the first-row elements. *Phys. Rev. B* **77** 115122 (2008).

77. Glen, G. L. & Dodd, C. G. Use of Molecular Orbital Theory to Interpret X-Ray K-Absorption Spectral Data. *J. Appl. Phys.* **39** (12), 5372–5377 (1968).

78. Hoffmann, R. How Chemistry and Physics Meet in the Solid State. *Angew. Chemie Int. Ed. English* **26** (9), 846–878 (1987).

79. Garvie, L. A. J., Craven, A. J. & Brydson, R. Use of electron-energy loss near-edge fine structure in the study of minerals. *Am. Mineral.* **79** 411–425 (1994).

80. Muller, D. A., Tzou, Y., Raj, R. & Silcox, J. Mapping sp2 and sp3 states of carbon at sub-nanometre spatial resolution. *Nature* **366** 725 (1993).

81. Lehmann, J. *et al.* Synchrotron-Based Near-Edge X-Ray Spectroscopy of Natural Organic Matter in Soils and Sediments. *Biophys. Process. Involv. Nat. Nonliving Org. Matter Environ. Syst.* 729–781 (2009). doi:10.1002/9780470494950.ch17

82. Cody, G. D. *et al.* Quantitative organic and light-element analysis of comet 81P/Wild 2 particles using C-, N-, and O-mu-XANES. *Meteorit. Planet. Sci.* **43** (1–2), 353–365 (2008).

83. Leapman, R. D. & Silcox, J. Orientation Dependence of Core Edges in Electron-Energy-Loss Spectra from Anisotropic Materials. *Phys. Rev. Lett.* **42** (20), 1361–1364 (1979).

84. Bosman, M., Watanabe, M., Alexander, D. T. L. & Keast, V. J. Mapping chemical and bonding information using multivariate analysis of electron energy-loss spectrum images. *Ultramicroscopy* **106** 1024–1032 (2006).

85. Bosman, M. *et al.* Quantitative, nanoscale mapping of sp2 percentage and crystal orientation in carbon multilayers. *Carbon N. Y.* **47** 94–101 (2009).

86. Egerton, R. F. Choice of operating voltage for a transmission electron microscope. *Ultramicroscopy* **145** 85–93 (2014).

87. Egerton, R. F., Li, P. & Malac, M. Radiation damage in the TEM and SEM. *Micron* **35** (6), 399–409 (2004).

88. R.F., E. Mechanisms of radiation damage in beam-sensitive specimens, for TEM accelerating voltages between 10 and 300 kV. *Microsc. Res. Tech.* **75** 1550–1556 (2012).

89. Blanksby, S. J. & Ellison, G. B. Bond Dissociation Energies of Organic Molecules. *Acc. Chem. Res.* **36** (4), 255–263 (2003).

90. Xu, K. Nonaqueous liquid electrolytes for lithium-based rechargeable batteries. *Chem. Rev.* **104** (10), 4303–4417 (2004).

91. Xu, K. Electrolytes and interphases in Li-ion batteries and beyond. *Chem. Rev.* **114** (23), 11503–11618 (2014).

92. Choudhury, S. & Archer, L. A. Lithium Fluoride Additives for Stable Cycling of Lithium Batteries at High Current Densities. *Adv. Electron. Mater.* **2** 1500246

(2016).

93. Tu, Z., Nath, P., Lu, Y., Tikekar, M. D. & Archer, L. A. Nanostructured Electrolytes for Stable Lithium Electrodeposition in Secondary Batteries. *Acc. Chem. Res.* **48** (11), 2947–2956 (2015).

94. Isaacson, M. Electron beam induced damage of organic solids: Implications for analytical electron microscopy. *Ultramicroscopy* **4** 193–199 (1979).

95. Li, Y. *et al.* Atomic structure of sensitive battery materials and interfaces revealed by cryo–electron microscopy. *Science (80-.).* **358** 506–510 (2017).

96. Egerton, R. F. Chemical measurements of radiation damage in organic samples at and below room temperature. *Ultramicroscopy* **5** 521–523 (1980).

97. Deal, B. E. & Svec, H. J. Kinetics of the reaction between lithium and water vapor. *Ames Lab. ISC Tech. Reports* **70** (1953).

98. Williams, D. B. & Carter, C. B. *Transmission Electron Microscopy*. (Springer Science + Business Media, LLC, 2009).

99. Wang, X. *et al.* New Insights on the Structure of Electrochemically Deposited Lithium Metal and Its Solid Electrolyte Interphases via Cryogenic TEM. *Nano Lett.* **17** (12), 7606–7612 (2017).

100. Dubochet, J. The Physics of Rapid Cooling and Its Implications for Cryoimmobilization of Cells. *Methods Cell Biol.* **2007** (79), 7–21 (2007).

101. Stephenson, J. L. Ice Crystal Growth During the Rapid Freezing of Tissues. *J. Biophys. Biochem. Cytol.* **2** (4 Suppl.), 45–52 (1956).

102. Echlin, P. *Low-Temperature Microscopy and Analysis*. (Springer Science+Business Media, 1992). doi:DOI 10.1007/978-1-4899-2302-8 ISBN

103. Tivol, W. F., Briegel, A. & Jensen, G. J. An Improved Cryogen for Plunge Freezing. *Microsc. Microanal.* **14** (5), 375–379 (2008).

104. Kesselman, E. *et al.* Cryogenic Transmission Electron Microscopy Imaging of Vesicles Formed by a Polystyrene−Polyisoprene Diblock Copolymer. *Macromolecules* **38** (16), 6779–6781 (2005).

105. Koifman, N., Schnabel-Lubovsky, M. & Talmon, Y. Nanostructure formation in the lecithin/isooctane/water system. *J. Phys. Chem. B* **117** (32), 9558–9567 (2013).

106. Oostergetel, G. T., Esselink, F. J. & Hadziioannou, G. Cryo-Electron Microscopy of Block Copolymers in an Organic Solvent. *Langmuir* **11** (10), 3721–3724 (1995).

107. Boettcher, C., Schade, B. & Fuhrhop, J. H. Comparative cryo-electron microscopy of noncovalent N-dodecanoyl-(D- and L-) serine assemblies in vitreous toluene and water. *Langmuir* **17** (3), 873–877 (2001).

108. Danino, D., Gupta, R., Satyavolu, J. & Talmon, Y. Direct cryogenic-temperature transmission electron microscopy imaging of phospholipid aggregates in soybean oil. *J. Colloid Interface Sci.* **249** (1), 180–186 (2002).

109. Bartesaghi, A. *et al.* 2.2 Å resolution cryo-EM structure of β-galactosidase in complex with a cell-permeant inhibitor. *Science (80-.).* **348** (6239), 1147–1151 (2015).

110. Scientific Background on the Nobel Prize in Chemistry 2017 - The Development of Cryo-Electron Microscopy. *Nobelprize.org* (2017). Available at: http://www.nobelprize.org/nobel_prizes/chemistry/laureates/2017/advanced.ht

ml. (Accessed: 21st May 2018)

111. Villa, E., Schaffer, M., Plitzko, J. M. & Baumeister, W. Opening windows into the cell: Focused-ion-beam milling for cryo-electron tomography. *Curr. Opin. Struct. Biol.* **23** 771–777 (2013).

112. Rubino, S. *et al.* A site-specific focused-ion-beam lift-out method for cryo Transmission Electron Microscopy. *J. Struct. Biol.* **180** 572–576 (2012).

113. Mahamid, J., Schampers, R., Persoon, H., Hyman, A. A. & Baumeister, W. A focused ion beam milling and lift-out approach for site-specific preparation of frozen-hydrated lamellas from multicellular organisms. *J. Struct. Biol.* **192** 262–269 (2015).

114. Parmenter, C. D. J., Fay, M. W., Hartfield, C. & Eltaher, H. M. Making the practically impossible 'Merely difficult'-Cryogenic FIB lift-out for 'Damage free' soft matter imaging. *Microsc. Res. Tech.* **79** (4), 298–303 (2016).

115. Hagfeldt, A., Boschloo, G., Sun, L. & Kloo, L. Dye-sensitized solar cells. *Chem. Rev.* **110** 6595–6663 (2010).

116. Stamenkovic, V. R., Strmcnik, D., Lopes, P. P. & Markovic, N. M. Energy and fuels from electrochemical interfaces. *Nat. Mater.* **16** 57 (2016).

117. Zhang, L. L. & Zhao, X. S. Carbon-based materials as supercapacitor electrodes. *Chem. Soc. Rev.* **38** (9), 2520–2531 (2009).

118. Cheng, X.-B. *et al.* A Review of Solid Electrolyte Interphases on Lithium Metal Anode. *Adv. Sci.* **3** (3), 1500213 (2016).

119. Krueger, R. Dual-column (FIB–SEM) wafer applications. *Micron* **30** (3), 221–226 (1999).

120. Zhu, Y. & Espinosa, H. D. An electromechanical material testing system for *in situ* electron microscopy and applications. *Proc. Natl. Acad. Sci. U. S. A.* **102** (41), 14503–14508 (2005).

121. Iwai, H. *et al.* Quantification of SOFC anode microstructure based on dual beam FIB-SEM technique. *J. Power Sources* **195** (4), 955–961 (2010).

122. Oostergetel, G. T., Esselink, F. J. & Hadziioannou, G. Cryo-Electron Microscopy of Block Copolymers in an Organic Solvent. *Langmuir* **11** (10), 3721–3724 (1995).

123. Zachman, M. J., Asenath-Smith, E., Estroff, L. A. & Kourkoutis, L. F. Site-Specific Preparation of Intact Solid–Liquid Interfaces by Label-Free In Situ Localization and Cryo-Focused Ion Beam Lift-Out. *Microsc. Microanal.* **22** (06), 1338–1349 (2016).

124. Hayles, M. F., Stokes, D. J., Phifer, D. & Findlay, K. C. A technique for improved focused ion beam milling of cryo-prepared life science specimens. *J. Microsc.* **226** (Pt 3), 263–269 (2007).

125. Sangster, J. & Pelton, A. D. The Ga-Li (Gallium-Lithium) System. *J. Phase Equilibria* **12** (1), 33–36 (1991).

126. Okamoto, H. Ga−Li (Gallium-Lithium). *J. Phase Equilibria Diffus.* **27** (2), 200 (2006).

127. Rosenblatt, S. *et al.* High Performance Electrolyte Gated Carbon Nanotube Transistors. *Nano Lett.* **2** (8), 869–872 (2002).

128. Prasad, B. *et al.* Integrated Circuits Comprising Patterned Functional Liquids. *Adv. Mater.* (Accepted),

129. Henderson, R. The potential and limitations of neutrons, electrons and X-rays for atomic resolution microscopy of unstained biological molecules. *Q. Rev. Biophys.* **28** 171–193 (1995).

130. Mahamid, J. *et al.* A focused ion beam milling and lift-out approach for site-specific preparation of frozen-hydrated lamellas from multicellular organisms. *J. Struct. Biol.* **192** (2), 262–269 (2015).

131. Tu, Z. *et al.* Designing Artificial Solid-Electrolyte Interphases for Single-Ion and High-Efficiency Transport in Batteries. *Joule* **1** (2), 394–406 (2017).

132. Tu, Z. *et al.* Fast ion transport at solid–solid interfaces in hybrid battery anodes. *Nat. Energy* **3** (4), 310–316 (2018).

133. Choudhury, S. *et al.* Designing solid-liquid interphases for sodium batteries. *Nat. Commun.* **8** (1), 898 (2017).

134. Choudhury, S. *et al.* Designer interphases for the lithium-oxygen electrochemical cell. *Sci. Adv.* **3** (4), (2017).

135. Kang, S.-H., Goodenough, J. B. & Rabenberg, L. K. Nanocrystalline Lithium Manganese Oxide Spinel Cathode for Rechargeable Lithium Batteries. *Electrochem. Solid-State Lett.* **4** (5), A49–A51 (2001).

136. Manthiram, A., Chemelewski, K. & Lee, E.-S. A perspective on the high-voltage LiMn1.5Ni0.5O4 spinel cathode for lithium-ion batteries. *Energy Environ. Sci.* **7** (4), 1339–1350 (2014).

137. Levin, B. D. A. *et al.* Characterization of sulfur and nanostructured sulfur battery cathodes in electron microscopy without sublimation artifacts. *Microsc. Microanal.* **23** (1), 153–162 (2017).

138. Burnett, T. L. *et al.* Large volume serial section tomography by Xe Plasma FIB dual beam microscopy. *Ultramicroscopy* **161** 119–129 (2016).

139. Xiaobing, L. *et al.* Detection of Lithium X-rays by EDS. *Microsc. Microanal.* **19** (Suppl 2), 1136–1137 (2013).

140. Henisch, H. *Crystals in Gels and Liesegang Rings*. (Cambridge University Press, 1988).

141. Emily, A., Hanying, L., C., K. E., Wei, S. Z. & A., E. L. Crystal Growth of Calcium Carbonate in Hydrogels as a Model of Biomineralization. *Adv. Funct. Mater.* **22** (14), 2891–2914 (2012).

142. Weiner, S. & Addadi, L. Crystallization Pathways in Biomineralization. *Annu. Rev. Mater. Res.* **41** (1), 21–40 (2011).

143. Botton, G. a. Probing bonding and electronic structure at atomic resolution with spectroscopic imaging. *MRS Bull.* **37** (January), 21–28 (2012).

144. Müller, S. A., Aebi, U. & Engel, A. What transmission electron microscopes can visualize now and in the future. *J. Struct. Biol.* **163** (3), 235–45 (2008).

145. Kourkoutis, L. F., Plitzko, J. M. & Baumeister, W. Electron Microscopy of Biological Materials at the Nanometer Scale. *Annu. Rev. Mater. Res.* **42** (1), 33–58 (2012).

146. Lučič, V., Rigort, A. & Baumeister, W. Cryo-electron tomography: the challenge of doing structural biology in situ. *J. Cell Biol.* **202** (3), 407–19 (2013).

147. Cheng, Y., Grigorieff, N., Penczek, P. A. & Walz, T. A primer to single-particle cryo-electron microscopy. *Cell* **161** (3), 439–449 (2015).

148. Milne, J. L. S. *et al.* Cryo-electron microscopy – a primer for the non-

microscopist. *FEBS J.* **280** (1), 28–45 (2012).

149. McDowall, A. W. *et al.* Electron microscopy of frozen hydrated sections of vitreous ice and vitrified biological samples. *J. Microsc.* **131** (1), 1–9 (2018).

150. Al-Amoudi, A., Norlen, L. P. O. & Dubochet, J. Cryo-electron microscopy of vitreous sections of native biological cells and tissues. *J. Struct. Biol.* **148** 131–135 (2004).

151. Al-Amoudi, A., Studer, D. & Dubochet, J. Cutting artefacts and cutting process in vitreous sections for cryo-electron microscopy. *J. Struct. Biol.* **150** (1), 109–121 (2005).

152. Marko, M., Hsieh, C., Moberlychan, W., Mannella, C. a & Frank, J. Focused ion beam milling of vitreous water: prospects for an alternative to cryo-ultramicrotomy of frozen-hydrated biological samples. *J. Microsc.* **222** (Pt 1), 42–47 (2006).

153. Marko, M. *et al.* Focused Ion Beam (FIB) Preparation Methods for 3-D Biological Cryo-TEM. *Microsc. Microanal.* **12** (S02), 98 (2006).

154. Marko, M., Hsieh, C., Schalek, R., Frank, J. & Mannella, C. Focused-ion-beam thinning of frozen-hydrated biological specimens for cryo-electron microscopy. *Nat. Methods* **4** (3), 215–217 (2007).

155. Hayles, M. F. *et al.* The making of frozen-hydrated, vitreous lamellas from cells for cryo-electron microscopy. *J. Struct. Biol.* **172** (2), 180–190 (2010).

156. Rigort, A. *et al.* Micromachining tools and correlative approaches for cellular cryo-electron tomography. *J. Struct. Biol.* **172** (2), 169–179 (2010).

157. Rigort, a *et al.* Focused ion beam micromachining of eukaryotic cells for

cryoelectron tomography. *Proc. Natl. Acad. Sci. U. S. A.* **109** (12), 4449–4454 (2012).

158. Arnold, J. *et al.* Site-Specific Cryo-focused Ion Beam Sample Preparation Guided by 3D Correlative Microscopy. *Biophys. J.* **110** (4), 860–869 (2016).

159. Parmenter, C., Fay, M., Hartfield, C., Amador, G. & Moldovan, G. Cryogenic FIB Lift-out as a Preparation Method for Damage-Free Soft Matter TEM Imaging. *Microsc. Microanal.* **20** (Suppl 3), 1224–1225 (2014).

160. Zachman, M. J., Asenath-smith, E., Estroff, L. A. & Kourkoutis, L. F. Revealing the Internal Structure and Local Chemistry of Nanocrystals Grown in Hydrogel with Cryo-FIB Lift-Out and Cryo-STEM. *Microsc. Microanal.* **21 (Suppl** (1144), 2291–2292 (2015).

161. Sartori, A. *et al.* Correlative microscopy: Bridging the gap between fluorescence light microscopy and cryo-electron tomography. *J. Struct. Biol.* **160** (2), 135–145 (2007).

162. Schwartz, C. L., Sarbash, V. I., Ataullakhanov, F. I., Mcintosh, J. R. & Nicastro, D. Cryo-fluorescence microscopy facilitates correlations between light and cryo-electron microscopy and reduces the rate of photobleaching. *J. Microsc.* **227** (2), 98–109 (2007).

163. Plitzko, J. M., Rigort, A. & Leis, A. Correlative cryo-light microscopy and cryo-electron tomography: from cellular territories to molecular landscapes. *Curr. Opin. Biotechnol.* **20** (1), 83–89 (2009).

164. Schellenberger, P. *et al.* High-precision correlative fluorescence and electron cryo microscopy using two independent alignment markers. *Ultramicroscopy*

143 41–51 (2014).

165. Agronskaia, A. V. *et al.* Integrated fluorescence and transmission electron microscopy. *J. Struct. Biol.* **164** (2), 183–189 (2008).

166. van Driel, L. F., Valentijn, J. A., Valentijn, K. M., Koning, R. I. & Koster, A. J. Tools for correlative cryo-fluorescence microscopy and cryo-electron tomography applied to whole mitochondria in human endothelial cells. *Eur. J. Cell Biol.* **88** (11), 669–684 (2009).

167. Kukulski, W. *et al.* Correlated fluorescence and 3D electron microscopy with high sensitivity and spatial precision. *J. Cell Biol.* **192** (1), 111–119 (2011).

168. Schorb, M. & Briggs, J. A. G. Correlated cryo-fluorescence and cryo-electron microscopy with high spatial precision and improved sensitivity. *Ultramicroscopy* **143** 24–32 (2014).

169. Asenath-Smith, E., Hovden, R., Kourkoutis, L. F. & Estroff, L. A. Hierarchically Structured Hematite Architectures Achieved by Growth in a Silica Hydrogel. *J. Am. Chem. Soc.* **137** (15), 5184–5192 (2015).

170. Asenath-Smith, E. & Estroff, L. A. Role of Akaganeite (β-FeOOH) in the Growth of Hematite (α-Fe_2O_3) in an Inorganic Silica Hydrogel. *Cryst. Growth Des.* **15** (7), 3388–3398 (2015).

171. Blesa, M. A. & Matijevi??, E. Phase transformations of iron oxides, oxohydroxides, and hydrous oxides in aqueous media. *Adv. Colloid Interface Sci.* **29** (3–4), 173–221 (1989).

172. Stark, T. J., Shedd, G. M., Vitarelli, J., Griffis, D. P. & Russell, P. E. H2O enhanced focused ion beam micromachining. *J. Vac. Sci. Technol. B* **13** (6),

2565–2569 (1995).

173. Gauvin, R. & Michaud, P. MC X-Ray, a New Monte Carlo Program for Quantitative X-Ray Microanalysis of Real Materials. *Microsc. Microanal.* **15** (S2), 488 (2009).

174. Hovington, P., Drouin, D. & Gauvin, R. CASINO: A new Monte Carlo code in C language for electron beam interaction - Part I: Description of the program. *Scanning* **19** 1–14 (1997).

175. Kanaya, K. & Okayama, K. Penetration and energy-loss theory of electrons in solid targets. *J. Phys. D. Appl. Phys.* **5** (1), 43 (1972).

176. Use of Monte Carlo Calculations in Electron Probe Microanalysis and Scanning Electron Microscopy: Proceedings of a Workshop help at the National Bureau of Standards, Gaithersburg, Maryland, October 1-3, 1975 (No. 460). in (eds. Heinrich, K. F., Newbury, D. E. & Yakowitz, H.) (US Department of Commerce, National Bureau of Standards: for sale by the Supt. of Docs., US Govt. Print. Off., Washington, DC., 1976).

177. Antoniou, N., Graham, A., Hartfield, C. & Amador, G. Failure Analysis of Electronic Material Using Cryogenic FIB-SEM. *Conf. Proc. from 38th Int. Symp. Test. Fail. Anal.* 399–405 (2012).

178. Yan, R. *et al.* Simultaneous determination of sample thickness, tilt, and electron mean free path using tomographic tilt images based on Beer-Lambert law. *J. Struct. Biol.* **192** (2), 287–296 (2015).

179. Vulovic, M. *et al.* Image formation modeling in cryo-electron microscopy. *J. Struct. Biol.* **183** (1), 19–32 (2013).

180. Chen, S.-Y. *et al.* Electron energy loss spectroscopy and ab initio investigation of iron oxide nanomaterials grown by a hydrothermal process. *Phys. Rev. B* **79** (10), 104103 (2009).

181. Garvie, L. A. J. Can electron energy-loss spectroscopy (EELS) be used to quantify hydrogen in minerals from the O K edge? *Am. Mineral.* **95** (1), 92–97 (2010).

182. Wu, Y. & Yang, P. Direct Observation of Vapor−Liquid−Solid Nanowire Growth. *J. Am. Chem. Soc.* **123** (13), 3165–3166 (2001).

183. Kudo, A. & Miseki, Y. Heterogeneous photocatalyst materials for water splitting. *Chem. Soc. Rev.* **38** (1), 253–278 (2009).

184. Yamaki, J. *et al.* A consideration of the morphology of electrochemically deposited lithium in an organic electrolyte. *J. Power Sources* **74** (2), 219–227 (1998).

185. Aurbach, D. Review of selected electrode-solution interactions which determine the performance of Li and Li ion batteries. *J. Power Sources* **89** (2), 206–218 (2000).

186. Bai, P., Li, J., Brushett, F. R. & Bazant, M. Z. Transition of lithium growth mechanisms in liquid electrolytes. *Energy Environ. Sci.* **9** (10), 3221–3229 (2016).

187. Kushima, A. *et al.* Liquid cell Transmission Electron Microscopy observation of lithium metal growth/dissolution: root growth, dead lithium and lithium flotsams. *Nano Energy* under review doi:10.1016/j.nanoen.2016.12.001

188. Tate, M. W. *et al.* High Dynamic Range Pixel Array Detector for Scanning

Transmission Electron Microscopy. *Microsc. Microanal.* **22** (1), 237–249 (2016).

189. Lin, F. *et al.* Phase evolution for conversion reaction electrodes in lithium-ion batteries. *Nat. Commun.* **5** 3358 (2014).

190. Cueva, P., Hovden, R., Mundy, J. A., Xin, H. L. & Muller, D. A. Data Processing for Atomic Resolution Electron Energy Loss Spectroscopy. *Microsc. Microanal.* **18** 667–675 (2012).

191. Heymann, J. a W. *et al.* Site-specific 3D imaging of cells and tissues with a dual beam microscope. *J. Struct. Biol.* **155** (1), 63–73 (2006).

192. Zhuang, G. V., Xu, K., Yang, H., Jow, T. R. & Ross, P. N. Lithium ethylene dicarbonate identified as the primary product of chemical and electrochemical reduction of EC in 1.2 M LiPF 6/EC:EMC electrolyte. *J. Phys. Chem. B* **109** (37), 17567–17573 (2005).

193. Yang, C. R., Wang, Y. Y. & Wan, C. C. Composition analysis of the passive film on the carbon electrode of a lithium-ion battery with an EC-based electrolyte. *J. Power Sources* **72** (1), 66–70 (1998).

194. Metzger, M., Strehle, B., Solchenbach, S. & Gasteiger, H. A. Origin of H2 Evolution in LIBs: H2O Reduction vs. Electrolyte Oxidation. *J. Electrochem. Soc.* **163** (5), A798–A809 (2016).

195. Szczęśniak, M. M. & Ratajczak, H. Ab initio calculations on the lithium fluoride–ethylene complex. *J. Chem. Phys.* **67** (11), 5400–5401 (1977).

196. Onuki, M. *et al.* Identification of the Source of Evolved Gas in Li-Ion Batteries Using ^{13}C-labeled Solvents. *J. Electrochem. Soc.* **155** (11), A794–A797 (2008).

197. Aurbach, D. & Weissman, I. On the possibility of LiH formation on Li surfaces

in wet electrolyte solutions. *Electrochem. commun.* **1** (8), 324–331 (1999).

198. Lu, Y., Tu, Z. & Archer, L. A. Stable lithium electrodeposition in salt-reinforced electrolytes. *Nat. Mater.* **13** 961–969 (2014).

199. Suo, L. *et al.* Fluorine-donating electrolytes enable highly reversible 5-V-class Li metal batteries. *Proc. Natl. Acad. Sci.* **115** (6), 1156–1161 (2018).

200. Zhao, Q. *et al.* Building Organic/Inorganic Hybrid Interphases for Fast Interfacial Transport in Rechargeable Metal Batteries. *Angew. Chemie Int. Ed.* **57** (4), 992–996 (2018).

201. Miki, T., Ikeya, M., Kondo, Y. & Kanzaki, H. Reflectance spectrum of lithium hydride at the Li K-absorption edge. *Solid State Commun.* **39** (5), 647–649 (1981).

202. Liu, D.-R. Electron energy loss spectroscopy of LiH with a scanning transmission electron microscope. *Solid State Commun.* **63** (6), 489–493 (1987).

203. Parades Mellone, O. A., Ceppli, S. A., Arneodo Larochette, P. P. & Stutz, G. E. Excitación de electrones K del Li a baja transferencia de momento por dispersión inelástica de rayos X en LiH. *An. AFA* **26** (2), 93–97 (2015).

204. Oudriss, A. *et al.* The diffusion and trapping of hydrogen along the grain boundaries in polycrystalline nickel. *Scr. Mater.* **66** (1), 37–40 (2012).

205. Settouti, N. & Aourag, H. Structural and mechanical properties of alkali hydrides investigated by the first-principles calculations and principal component analysis. *Solid State Sci.* **58** 30–36 (2016).